DOI:10.15774/PPKE.ITK.2020.005

Advanced recording techniques for studying cellular-level neurophysiology

Domokos Meszéna

Pázmány Péter Catholic University

The Faculty of Information Technology and Bionics

Roska Tamás Doctoral School of Sciences and Technology

Scientific advisor:
István Ulbert, MD., D.Sc.

A thesis submitted in partial fulfilment of the requirements for the degree of Doctor of Philosophy

2019

DOI:10.15774/PPKE.ITK.2020.005

DOI:10.15774/PPKE.ITK.2020.005

Non est volentis, neque currentis, sed miserentis Dei.

/ Romans 9:16 /

DOI:10.15774/PPKE.ITK.2020.005

Abstract (in English)

It has long been known, that neurons communicate via bioelectric signals, which are systematic alterations of the membrane potential (both positive and negative directions are allowed). There are numerous ways for studying these bioelectric phenomena. Recently, multi-electrode arrays (from 16 up to thousands of channels) as well as advanced imaging methods were developed to detect and track hundreds of neurons simultaneously in one experiment. Despite the technological advances, several aspects of the generated extracellular potential remain poorly understood. Moreover, a very limited knowledge is available about the validation of these extracellular signals using other complementary modalities, such as intracellular ground-truth recordings or fluorescent two-photon microscopy.

Within the framework of this dissertation I focus on three different aspects of extracellular signal acquisition and validation. I. Thesis group introduces the development and testing of a novel, multi-channel silicon probe with protruding contact sites for improved *in vitro* extracellular recordings and highlights the advantages of this novel design compared to a commercially available, multi-channel surface probe. II. Thesis group presents a novel experimental method developed for co-localised and simultaneous intra- and extracellular recording, it describes the resulting '*ground-truth*' dataset, and explores further potential applications of the recorded data in model-based calculations. Whole-cell patch-clamp recordings were carried out to detect intracellular single cell activity, in rat hippocampal slices. Extracellular signal was detected in the vicinity of the same neuron. Detailed morphology of the recorded and filled cell was revealed by three dimensional reconstruction. A preliminary application in single-cell level current source density analysis will also be presented using the collected dataset. III. Thesis group starts with the description of the photoelectric artefact generated during the use of combined multichannel extracellular recordings and two-photon laser imaging. Recent strategies to eliminate contaminations of photoelectric artefacts are discussed with their limitations. Next I present an experimental protocol for the generation of co-localised and simultaneous extracellular recordings and two-photon imaging either with or without laser artefacts. The protocol allows for investigating photoelectric artefacts but also for providing control data and validation. A collaborative specific filtering algorithm will be presented to mitigate the photoelectric effect on the recorded extracellular data. The dissertation closes with the list of all novel scientific contributions and related publications. Lastly I give an outlook for future perspectives and possible application of my results.

The presented methods allow for improved investigations of single cell dynamics together with their environments. Simultaneous and multi-modal signals recorded throughout this thesis work may yield additional information for various model-based calculations in the future and may also give rise to novel findings in designing advanced neural interfaces.

DOI:10.15774/PPKE.ITK.2020.005

Összefoglaló (in Hungarian)

Régóta ismert, hogy az idegsejtek bioelektromos jelek útján kommunikálnak, melyek a membránpotenciál szisztematikus megváltoztatásai (mind pozitív és negatív irányok megengedettek). Számos módszer létezik e bioelektromos jelenségeknek tanulmányozására. A közelmúltban sokcsatornás multielektróda tömbök (16-tól akár több ezer csatornáig), valamint specifikus képalkotó módszerek is kifejlesztésre kerültek számos idegsejt egyidejű detektálására és nyomon követésére. Mindezen technológiai fejlődések ellenére az extracelluláris potenciál létrejöttének számos aspektusa még nem ismert. Kevés információ áll rendelkezésre továbbá az extracelluláris jelek validációjáról más kiegészítő modalitások, például intracelluláris ún. „*ground-truth*" mérések vagy fluoreszcens két-foton mikroszkópia segítségével.

A disszertáció keretein belül az extracelluláris jelek elvezetésének és validálásának három különféle szempontjára összpontosítok. Az I. téziscsoport bemutatja egy újszerű, szilícium-alapú sokcsatornás elektróda fejlesztését és tesztelését, mely tüskeszerűen kiálló elvezető pontokkal rendelkezik az *in vitro* extracelluláris mérések minőségének javítása érdekében, továbbá a tézis részletezi az érzékelő előnyeit egy kereskedelmi forgalomban kapható, felszíni sokcsatornás elektródával szemben. A II. téziscsoport részletesen ismertet egy új kísérleti módszert az intra- és extracelluláris felvételek egyidejű és lokalizált rögzítésére. Bemutatja továbbá a keletkező "*ground-truth*" adathalmazt, és példát ad az adatok egy lehetséges jövőbeli alkalmazására modell-alapú, elméleti számításokon. Az egysejt aktivitások kimutatására sejttestről elvezetett "*patch-clamp*" intracelluláris méréseket végeztem patkányok hippokampusz szeletein. Az extracelluláris jeleket ugyanazon neuron közvetlen közelében vezettem el. A mért és feltöltött sejtek részletes morfológiáját háromdimenziós térképezéssel rekonstruáltam. Egy előzetes alkalmazási terület, az egysejt-szintű áramforrás sűrűség elemzés szintén bemutatásra kerül az itt gyűjtött adatok felhasználásával. A III. téziscsoport az ún. "*fotoelektromos műtermék*" leírásával indul, mely kombinált extracelluláris és két-foton lézermikroszkópiás egyidejű mérés során keletkezik. E fotoelektromos műtermék szennyező hatásának kiküszöbölésére irányuló legújabb stratégiák részletes bemutatásra kerülnek. Ezt követően leírásra kerül egy kísérleti protokoll a lokalizált és egyidejű extracelluláris és két-foton fluoreszcencia jelek együttes rögzítésére, mind az említett lézeres műtermékekkel szennyezett módon, illetve anélkül. Ez a protokoll lehetővé teszi a fotoelektromos műtermékek és zajok vizsgálatát mindamellett, hogy zajmentes kontroll adatot is biztosít az eredmények validációjához. Egy kollaborációs, speciális szűrőalgoritmus is bemutatásra kerül az extracelluláris jeleken megjelenő fotoelektromos hatás enyhítésére. A dolgozat az új tudományos hozzájárulások felsorolásával zárul és az ezekhez kapcsolódó publikációkkal. Végül kitekintést teszek a jövőbeli tervekre és az eredmények lehetséges alkalmazási területeire.

A bemutatott módszerek lehetővé teszik az egysejt dinamikák és környezetük egyidejű és pontos vizsgálatát. A doktori disszertációs munka során rögzített multimodális jelek további információkkal szolgáltathatnak különféle modell-alapú számításokhoz, és új szempontokkal segíthetik a jövőbeli neurális interfészek tervezését.

DOI:10.15774/PPKE.ITK.2020.005

Abbreviations

2P Two-Photon

aCSF Artificial Cerebrospinal Fluid
AP Action Potential

BPAP Back-Propagating Action Potential
BPF Band-pass filter

ChR Channelrhodopsin
CNS Central Nervous System
CP Conductive Polymer
CSD Current Source Density

DRIE Deep Reactive Ion Etching

EAP Extracellular Action Potential
EBG Etching Before Grinding
EIS Electrochemical Impedance Spectroscopy
EM Electron Microscopy
EPSP Excitatory Postsynaptic Potential

FoV Field-of-View
FPGA Field Programmable Gate Array

IAP Intracellular Action Potential
IR Infra Red
ITO Indium Tin Oxide

LFP Local Field Potential

MEA Multi-Electrode Array
MEMS Micro-electromechanical Systems
MUA Multi-Unit Activity

NIR Near Infra-Red

PCA Principal Component Analysis
PEDOT Poly(3,4-ethylenedioxythiophene)
PETH Peri-Event Time Histogram
PMT Photomultiplier
PSS Polystyrene Sulfonate

RMS Root Mean Square
ROI Region Of Interest

SEM Scanning Electron Microscopy
SNR Signal to Noise Ratio
SPA Spontaneous (or synchronous) Population Activity
STA Spike Triggered Average
STD Standard Deviation
SUA Single Unit Activity
SWR Sharp Wave Ripple

DOI:10.15774/PPKE.ITK.2020.005

Contents

DOI:10.15774/PPKE.ITK.2020.005

Acknowledgements

I consider my situation exceptionally lucky for having the privilege of constantly "*standing on the shoulders of Giants*" during the years of completing my doctoral studies. I am indebted to a great number of people for their guidance, collaboration and support:

First and foremost, my deepest gratitude goes to my Ph.D. supervisor, *István Ulbert*, who gave me the opportunity to enter the fascinating fields of experimental neuroscience and neurotechnology. I thank him that he gave me great ideas and hard challenges but at the same time, he paved my way by providing all necessary intellectual, generous financial and never-ending personal support to succeed.

I would like to give thanks to the Professors and administrative members of *PPCU Faculty of Information Technology and Bionics* for the immense amount of shared knowledge as well as for the supportive and great atmosphere of '*ITK*' during my whole university curricula. Being one among the '*pioneering*' freshman students, it was a unique experience to me to be part of the newly founded Bionics Faculty from its very beginning. I am grateful, *inter alia* to *György Karmos* (who was the first to motivate me as a graduating high school student, towards bionics and neural interfaces during an open day at the University in 2007), *Árpád Csurgay*, *Péter Szolgay* (pro-dean), *Kristóf Iván* (dean), *György Fodor* (rector at that time), *István Jelenits SchP*, *György Hámori*, *Tamás Freund*, *András Falus*, and so many more '*Giants*' but most of all, to †*Tamás Roska* (pro-dean). Professor Roska was not only a world-renowned researcher or the founding and leading mind of the Hungarian bionics research, but a very friendly and inquiring person towards his students. His pieces of life advice and his optimism (" *Tell me some good news!*") during our personal conversations will ring in my ears forever and will motivate my further career.

I am very grateful to *Katinka Vida Tivadarné* and to the *Economy Office* for their availability and helpfulness regarding all of my (sometimes even silly) administrative, travelling or financial issues and questions throughout the program. Similarly, I am sincerely thankful for all the previous research experiences gained under the guidance of my former supervisors, *László Négyessy* (Wigner) and *Gábor Szederkényi* during Bachelor and Master Studies, respectively.

Many thanks are given to the '*UlbertLab members*' (Research Centre for Natural Sciences) for the great working atmosphere, exciting discussions during lab meetings, amazing group experiences while attending various conferences together and for so much fun in Szigliget during annual lab retreats. From the alumni side, I am indebted to *Ildikó Pál* for teaching me a lot

DOI:10.15774/PPKE.ITK.2020.005

of hours how to make proper *in vitro* electrophysiology recordings. She was my first unofficial mentor in generating strict and highly reproducible research output while maintaining a clean and controlled research environment in the lab. However, all other lab members have significant contribution in my professional development and I am grateful for our fantastic community.

I would like to express my special gratitude to my main collaborator *Zoltán Somogyvári* (Wigner). It has always been an honour to learn from him during our conversations, which were usually not limited to science but rather covered numerous other aspects of life too. His optimistic and encouraging support towards me never waned. And again, I consider him as my second unofficial mentor during these years. I have also very much appreciated the exceptional occasion and have learnt plenty of useful things from *Péter Somogyi* (Oxford, UK) during my research visit at his lab in the winter of 2018.

From the technology side, I would like to acknowledge the work of *Patrick Ruther* (Freiburg, Germany) in manufacturing my '*spiky*' probes and I am grateful for his strict but very constructive proofreading of my first-author manuscript. From the service side, I have to mention *Gergely Cserkúti* (Femtonics, senior service engineer), whose constant availability and rapid troubleshooting skills helped me out countless times regarding various software bugs and hardware issues within the two-photon imaging system.

I am not forgetting my fellow doctoral students as they demonstrated to be real friends, *Gergely Csány*, *Bertalan Kovács*, *Máté Handbauer* and our '*Mókacsoport*'☺(which means a fun group activity, but originally formed as a university working group and transformed only later from '*Munkacsoport*' to represent something less serious). It would be challenging to list all of my friends in- and outside of science who have helped me indirectly, for example with an unfailing source of humour or via their uplifting companionship.

But most of all, I thank my Family, my parents *Mami* (Ágnes) and *Apu* (Tamás), and my siblings *Dóra*, *Réka* and *Peti* for all the unconditional love and care they offered me. They are my role-model in building and preserving a cohesive family. Finally, I would like to dedicate this thesis to my wife, *Neszta* and to my son, *Máté*. Being a part of my own family, I know they put even more effort into this dissertation than I did. I am deeply grateful for their patience, love and encouragement.

The research project has been partially supported by the European Union, co-financed by the European Social Fund (EFOP-3.6.3-VEKOP-16-2017-00002).

DOI:10.15774/PPKE.ITK.2020.005

Preface

"My way is to begin with the beginning"

- as Lord Byron once said, and he was certainly right in this regard. Now, let us consider me being worried to find my own appropriate beginning. Clearly, I should start my neuroscience related dissertation with the word '*brain*', that is the origin of the whole thesis work.
To tell the truth, I did my best as follows:

"The human brain is one among the most complex systems
ever investigated by the human brain"

After this heavily cliché-like sentence, I would rather stop (and may even finish writing at all), as a far-reaching vicious cycle immediately showed up at this very first moment: " *Can the observer observe himself*"? While I have no guaranteed answer, for the sake of continuation I kindly ask the Reader to let me accept the unverified axiom that the answer is (at least partially) yes and to jump with me elegantly over any yet unanswered questions of '*philosophy*' by focusing on similarly sounded, but easier-to-answer questions of '*physiology*'.
Then we ask the following: " *Where does this unexpected complexity of the brain come from*"? Paradoxically, we know the brain is formed of relatively simple elements: neurons, glial cells and a few other cell types. The only explanation would be, if the brain's complexity originates from the variety of subtle ways those simple elements interconnect and co-operate to form dense neural circuits producing network phenomena. And how to capture and record those well-orchestrated activity patterns which generate such complex physiological functions? A proper description would require interplay between various electrical and optical recording methods as well as computational modelling tools together with state-of-the-art data analysis algorithms. But even using all modalities simultaneously, our answers may still remain incomplete.
In spite of all these, we possess a tireless and keen interest in studying complex population activities in the brain, which interest stems from the fact that these particular rhythms, oscillations, or waves become altered in famous syndromes, including but not limited to epilepsy, Alzheimer's disease, Parkinson's disease, schizophrenia, anxiety and depression. Consequently, investigating origins and dynamics of these pathological events may lead to a better understanding of governing mechanisms or ultimately, to the capability of providing early markers for detection and treatment of listed neurological diseases.

DOI:10.15774/PPKE.ITK.2020.005

Chapter 1

Introduction

1.1 Motivations and goals of this dissertation

To reveal the biophysical basis of observable global states of the brain (such as cognitive processes or a particular behaviour) a wide range of different approaches were developed and applied, either based on bottom-up or top-down strategies.
The two leading methods for the bottom-up approach are penetrating electrophysiological recordings via intra- and extracellular probes. The words '*intracellular*' (IC) and '*extracellular*' (EC) refer to the electrode location inside and outside the targeted cells, respectively. While these devices become the workhorses of cellular neurotechnology providing direct access to bioelectrical events generated by single or multiple neurons, their invasiveness limits the applicability for chronic and human usage. On the other pole of the scale, imaging and recording methods with the capability of recording multiple regions or even whole-brain activities have been developed in parallel. Such top-down techniques include '*functional magnetic resonance imaging*' (fMRI) or '*positron emission tomography*' (PET) from the imaging side and '*electroencephalography*' (EEG) or '*magnetoencephalography*' (MEG) from the electrophysiology side. All of these technologies have the advantage of remaining completely non-invasive and thus becoming applicable even for human clinical applications instead of being mostly restricted to animal-based research. In spite of intensive progresses either in bottom-up and top-down approaches, there is still a significant, uncovered gap in the middle, namely how individual cells can be spatio-temporally coordinated in local networks to form specific cognitive functions. This so called '*mesoscopic*' range is of great interest recently in neurophysiology (and in its corresponding neurotechnology) and thus will be the main focus of this current thesis as well.

This mesoscopic range will be investigated by means of extracellular multi-channel probes covering wider area than single-electrode recordings. Figure 1.1 illustrates schematically a metaphor of EC and IC potential recordings. Imagine a recording device (a microphone) hanging in the middle of a football stadium (Figure 1.1a, upper subfigure). Since it is a microphone, no visual information can be captured during recordings, only the number of

DOI:10.15774/PPKE.ITK.2020.005

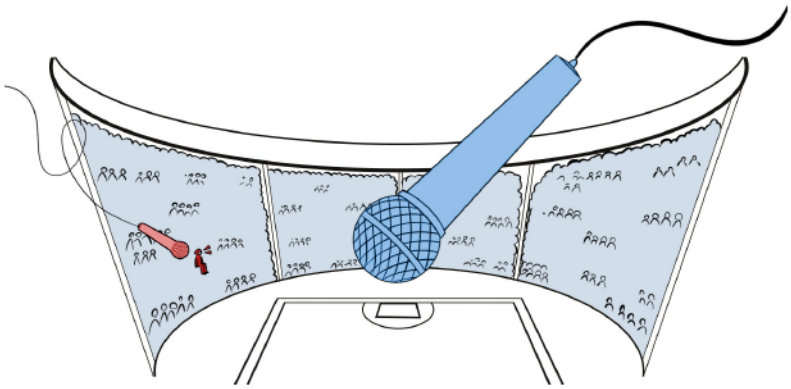

(a) Metaphor of extra- and intracellular recordings

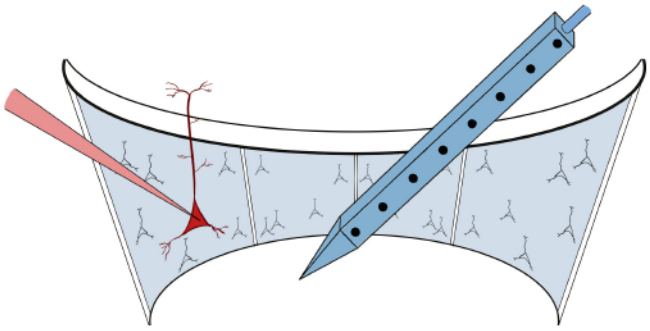

(b) Schematics of realistic extra- and intracellular recordings

Figure 1.1: Metaphor of an implantable neural electrode and surrounding neural tissue. Extracellular electrode and co-localised, simultaneous intracellular patch-clamp recordings are coloured in blue and red, respectively. The theory of this animation is based on the reviews of Buzsáki, et al. (2004, 2012) [1, 2].

microphones can be increased to have better resolution and larger coverage. Large microphone (in blue) placed in the centre of the arena can possibly acquire loud chants generated by the surrounding crowd of people, but it would hardly isolate independent voices of all individuals out of this mass singing. In contrast to this, a small microphone (in red) placed closely to one particular fan (somewhere in the front rows) would record this person's voice with great quality and fidelity. However, this small microphone is limited to exclusively record from one person, and the background of the stadium will be suppressed. To compare voices of individuals to the mass singing, it is easy to see, that both large and small microphones are essential to reconstruct their exact relationship.

Let us immediately transform the devices of this metaphor into electrophysiological correlates. On Figure 1.1b (lower subfigure) large microphone corresponds to an extracellular multi-channel recording device, while the small microphone represents an intracellular recording method. To investigate the relationship between one single cell and its environment, and how this particular cell contributes to the population signal, we have to use co-localised and simultaneous IC and EC recordings. Both words of 'co-localised' and 'simultaneous' are to be

fulfilled, hence spatio-temporally synchronised recordings can only provide proper information about their interconnection. Indeed, we have to be literally "*in the front rows*" with the small microphone (or intracellular electrode), since a very short distance is crucial for finding this '*small voice*' in the population average. According to the literature, this inter-probe distance (or corresponding cell-electrode distance) should be in the range of tens of microns, but maximally below 100 μm to achieve sortable signals with high-quality EC voltage traces [2, 3, 4, 5, 6].

Considering EC recordings, it is well known, that neural signals are detectable at further distances from their source, the phenomenon is called '*volume conduction*' [7, 8] and it will be discussed in details within Background section 2.2.1. However, several complications may emerge from the volume conductive property of the neural tissue and from the summation of different currents sources over distance [9, 10]. Such drawbacks make the interpretation of the EC recorded potentials extremely challenging. Besides theoretical considerations, measurement-related technical challenges also play important roles in achieving high-quality results. The closer an extracellular device can be positioned to the neuronal source, the better recording quality can be achieved. An unsuitably designed contact site layout would prevent the detection of further neural activities which would have been otherwise detectable using an optimal layout. Sufficiently large signal amplitudes are needed to feed in the theoretical calculations in order to achieve correct results. Previous studies have shown that small contact site area and sufficiently low impedance are also essential to detect well-isolated EC signals over the background noise [11]. However, the area of the contact site and its impedance are inversely proportional to each other [12]. In addition to this, a well-designed electrode-tissue interface is also needed to access recorded cells without significantly damaging them, and to detect as many as possible active cells in the close vicinity of the probe [13, 14, 15, 16]. For *in vitro* brain slice EC electrophysiology, this requirement is particularly important, since the surface of the slice is considered to be a dead-cell layer due to cut-off dendrites and cell bodies. The electrically passive dead-cell layer frequently attenuates signals originated from other, physiologically more active cells located deeper in the tissue [17, 18].

In this current thesis, I focus on *in vitro* brain slice electrophysiology using penetrating EC multi-channel, laminar probes. Cutting the brain into thin slices has allowed access to neurons located deeper in the brain. Brain slice preparations can be used for either imaging or recording neural activities that would be otherwise difficult to reach and detect *in vivo*. Similarly to *in vivo* conditions, it is also possible to observe *in vitro* population responses, such as '*sharp wave ripples*' (SWR) or some other inherent oscillations [19]. Furthermore, an additional advantage of *in vitro* brain slice recordings is the ability to combine different modalities, which would be again, challenging or not feasible *in vivo* [20, 21, 22].

The ultimate goal of my doctoral student work is to invent and implement useful, novel methodologies to support different biological research questions. These methodological aims are the following:

- To develop, characterise and valide a novel, multi-channel spiky probe for high-quality extracellular recordings in brain slices.
- To acquire co-localised, simultaneous intra- and laminar extracellular recordings with corresponding neuronal morphology for generating a freely available, open-source ground-truth dataset.
- To combine multi-channel extracellular recordings and the imaging of two-photon laser scanning microscopy for the characterisation of the thus generated photoelectric artefact and to provide benchmark dataset for the development of an artefact filtering algorithm.

These research aims will be detailed separately within the Results Section 4 in Thesis groups 4.1, 4.2, and 4.3.

1.2 Topics overview

For the benefit of the Reader, I shortly outline the main independent topics of the dissertation. Following this introductory section, Chapter 2 will cover the biophysical theory of IC and EC potentials and their relationship as well as will detail the recent technical developments and their limitations.
With this knowledge in hand, Chapter 3 introduces multi-channel silicon probes used throughout the thesis; this same chapter elaborates on the experimental methods and closes with the description of data analysis methods and histological procedures.
Once given the theoretical and methodological bases to contextualize this work, Chapter 4 will split the results into three independent thesis groups:
On Figure 1.2 a triangle illustrates the relationship of the three theses (edges) and three experimental techniques used (nodes). Although there are small exceptions (such as, occasional IC-2P recordings in II. Thesis group, shown with a dashed line), edges represent the main interactions between recording modalities. I. Thesis group (4.1) presents the development and testing of a novel, multi-channel silicon probe with protruding contact sites for improved *in vitro* EC recordings and highlights its advantages with a systematic and quantitative comparison against a commercially available, multi-channel surface probe. This chapter will focus only on EC recording without IC patch-clamp and with only one representative 2P figure showing that the spiky probe is compatible with two-photon microscope imaging.
II. Thesis group (4.2) details an approach developed for co-localised and simultaneous IC-EC recording, it describes the resulting '*ground-truth*' dataset, and explores potential further applications of the recorded data in model-based calculations. This thesis does not

focus on a thorough evaluation of any data analysis method (such as spike-sorting algorithms or source-localization methods), however, a preliminary application of single-cell level current source density analysis (skCSD) will be presented using the collected simultaneous data.

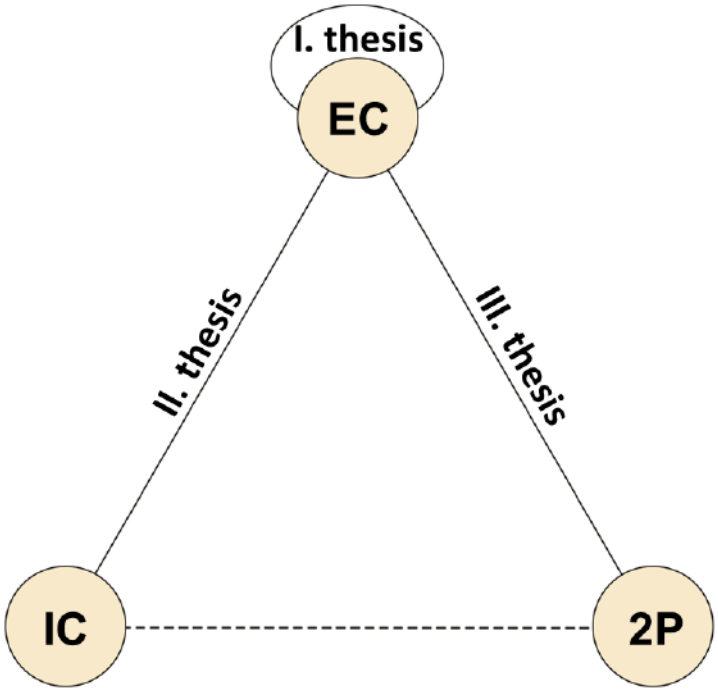

Figure 1.2: Interconnections between thesis groups (edges) and topics covered (nodes).

III. Thesis group (4.3) starts with the description of the photoelectric artefact generated during the use of combined multi-channel EC recordings and two-photon (2P) laser imaging. Recent strategies to eliminate contaminations of the photoelectric artefact will be discussed together with their limitations. Next I present an experimental protocol for the generation of co-localised and simultaneous EC and 2P measurements either with or without laser artefact. The protocol allows for the investigation of photoelectric artefacts but also for providing control data for validation. Using these combined recordings, a developed specific filtering algorithm will be presented to mitigate the photoelectric effect on recorded extracellular signals.
In Chapter 5 I discuss several shortcomings and open questions emerged throughout the results of the three Thesis groups. Finally, Chapter 6 closes the dissertation by listing the novel scientific contributions of this thesis work with related publications and giving an outlook for future perspectives and for the application of the results.

DOI:10.15774/PPKE.ITK.2020.005

Chapter 2

Theoretical background

2.1 Basic neurobiological concepts

Neurons in the central nervous system (CNS) have three typical subcellular sections: soma (also called cell body or '*perykarion*'), dendrites and an axon. These anatomical structures were already examined by the '*father of modern neuroscience*', Santiago Ramón Y Cajal more than hundred years ago. Cajal also noticed (among his countless other findings) that these processes are interconnected and the information flows along the axons towards the dendrites (his theory called a '*dynamic polarisation*'. Unlike Camillo Golgi, who described the CNS - using his self-developed Golgi-staining technique - as a single continuous network, in support of the '*reticular theory*', Cajal reported that the CNS is not continuous and is built up from the presence of a large number of individual nerve cells according to the '*neuron doctrine theory*' [23]. Golgi and Cajal awarded the Nobel Prize together in 1906, but the controversy between the views of those two great scientists remained yet unsolved for decades. The question was finally resolved only in the 1950s with the development of electron microscopy (EM), validating the neuron doctrine and discovering the synapse, the interconnections between individual nerve cells.

In order to understand the complex functional roles of neurons in the CNS, one needs to place them into their precise anatomical locations. Similarly one should first examine the basic electrophysiological principles of their information processing, before deriving functional conclusions about neural coding. In the following subsections I will give a short introduction on the anatomy of hippocampus and neocortex and characterise basic intra- and extracellular mechanisms leading to measurable and functional roles of single and mass neural activities.

2.1.1 Hippocampal Formation and Neocortex (structure and function)

The '*cortex cerebri*' in humans consists of around 15 billion neurons (out of the 80 billion neuron in the whole brain) [24]. Within the cerebral cortex we can identify phylogenetically separated parts, such as the youngest and most complex '*neocortex*' or the simpler and older '*allocortex*',

which can be further differentiated to '*archicortex*' (e.g. hippocampus) and '*paleocortex*' (e.g. olfactory cortex). Cortical regions are lamellar structures, but hippocampus has less layers (only three or four), compared the six-layered neocortex. This may be the reason, why hippocampus has been of great interest from the beginning of modern neurosciences. Its simplicity played a key role in understanding the connection between neural structure and function. Hippocampus is one of the few brain parts clearly visible by naked eye, and it is a typical obligatory task for freshmen medical students to recognise its beautiful curvature from coronally sliced brains. The intrinsic and extrinsic synaptic pathways are also well organized leading to spontaneous and evoked activities that are easy to detect during recording and stimulation. Finally, it is already known that hippocampus plays a crucial role in learning, memory, and spatial navigation [25]. But despite of intensive investigation for decades (or even for a century), many unsolved aspects of its function confound researchers. The term '*hippocampal formation*' refers to all contributing parts of this structure, the '*entorhinal cortex*' (ECx), '*dentate gyrus*' (DG), CA1-4 regions and the '*subiculum*' (Sub), while the term '*hippocampus proper*' corresponds only to CA1-4 ('*cornu ammonis*') regions. The layers of the hippocampus proper constist (from dorsal to ventral)

- I. stratum oriens: scattered interneurons and glial cells can be seen here
- II. stratum pyramidale: this layer is built up of densely packed pyramidal cells
- III. stratum radiatum: the name is derived from the radiating pyramidal apical dendrites
- IV. stratum lacunosum-moleculare: the molecular layer containing distal dendrites of pyramidal cells

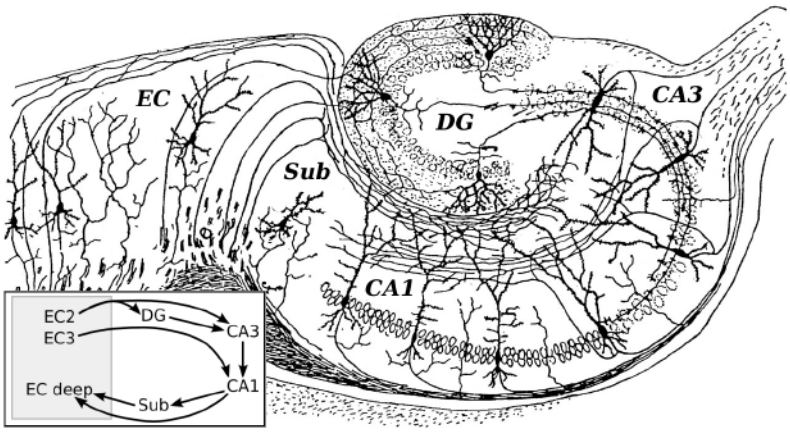

Figure 2.1: This original drawing of Cajal shows the hippocampal subdivisions with their main cell types and axonal pathways [23]. Bottom left: The schema of classical information flow within the hippocampus.

Figure 2.1 is one of Cajal's original drawings and depicts the main regions, cell morphologies and axonal arbours completed with a schema of information flow (bottom left) [23]. According to the classical hypothesis, a '*trisynaptic loop*' forms the main input and output of the

hippocampus, as a feed-forward, excitatory circuit. Neurons from ECx (layerII) project to the DG through the '*performant path*'. DG granule cells send their axon called '*mossy fibers*' (after their 'hairy' axon terminals) to the proximal apical dendrites (located in a region specific '*stratum lucidum*' sub-layer of stratum radiatum) of CA3 pyramidal cells. CA3 pyramidal axons both make recurrent (or auto-associative) network in the CA3 and divide their axons, and through these '*Schaffer-collaterals*' (after Károly Schaffer, Hungarian neurologist) they innervate CA1 pyramidal cells, which project to the Sub and ECx (deep layers) as an output of the hippocampus proper. To complicate the classical view, short-cuts are also present, since ECx (layerII) innervates CA3 directly, and ECx (layerIII) projects to CA1 through the '*temporoammonic*' pathway. Furthermore ECx also has a recurrent collateral network (and CA1 as well, but very sparse), however, back-projections are generally not present in any step of the loop (again, except some projection from the CA3 back to DG). Since the focus of the thesis is the CA1 pyramidal layer, we do not aim for listing all the possible pathways and connections in other areas.

Besides excitatory principal cells, there is a large variety of (mostly inhibitory) interneurons with cell-type specific distribution between layers and regions in the hippocampus. With their large difference in morphology, immunohistochemistry and intrinsic firing properties, the unambiguous classification of interneuron cell types is a major issue [26]. Immunohistochemical markers can be (included but not limited to): CCK+, CB+, VIP+, SST+, PV+, etc. [26, 27]. Another way of classification is based on the innervation and projections. Interneurons targeting the perisomatic regions of pyramidal cells called '*basket-cells*', and '*axo-axonic cells*' if they specifically target the '*axon initial segment*' (AIS), or more distal dendrites, such as '*O-LM cells*' or '*bistratified cells*'. Interestingly, the axo-axonic cell was the only one among these basic interneuron types, which was not found by Ramón Y Cajal, and remained hidden until discovered in 1977 by Peter Somogyi ([28]). And still in the last few years, there are novel definitions and separations for interneuron types based on state-of-the-art transcriptomic screening [29]. Today the question is whether these genetically different cell types are also functionally different and if yes, then what are their specific roles within the neural circuitry, *in vivo*.

While neocortex is similar in many ways to archicortex, it is responsible for more complex information processing tasks, as sensory perception or motor execution, and it gives us the capacity of using even higher-level functions such as language or thinking. The neocortex has six layers of grey matter, and a 2-4 mm thickness in humans covering the external part of the brain, along the gyri and sulci. These layers (in top-down direction) are:

- I. Molecular layer - consists only a few cells
- II. Outer granular layer– relatively thin layer consisting of numerous small, densely packed neurons

- III. Outer pyramidal layer - is composed of medium-sized pyramidal cells
- IV. Inner granular layer - contains small, irregularily shaped cells
- V. Inner pyramidal layer - includes large, ganglion-like pyramidal cells
- VI. Multiform layer - small polymorphic cells are located here

The neocortex is often described in vertical structures called '*cortical columns*' with a diameter of roughly 0.5 mm (and a depth of 3-4 mm, i.e., spanning all six layers). In one column there are nearly 5000 cells, and the number of columns is estimated to 2-3 millions, corresponding to the 10-15 billions of neocortical cells. These columns are often thought of as the basic, repeating functional units of the neocortex, but their definition, in terms of anatomy, size, or function, are generally not consistent, leading to a lack of consensus regarding their structure or function.

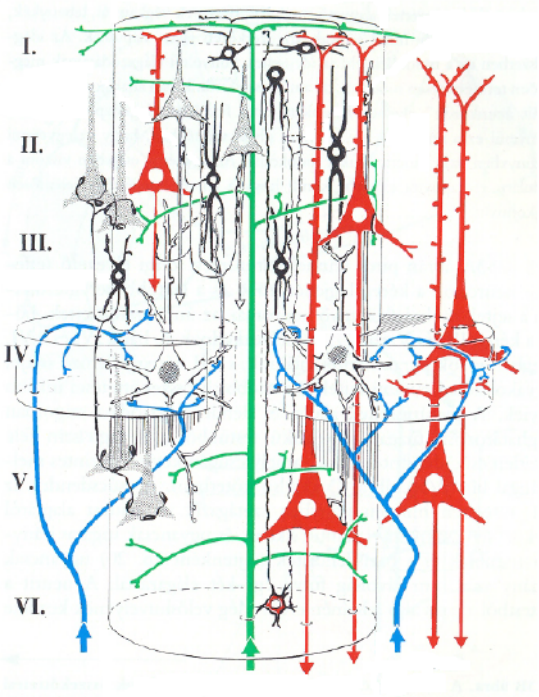

Figure 2.2: General connectivity of a neocortical column drawn by János Szentágothai in 1971. Colours of the sketch are the following: pyramidal cells (red), cortico-cortical afferent fibers (green), specific afferents (blue), multiple interneurons (black) [30].

Nevertheless, there is also some canonical circuitry within the neocortex, even if it is not as conserved as the hippocampus. Pyramidal cells in layer II and III project their axons to other areas within the neocortex, while cells in deeper layer V and VI often project out of the neocortex (e.g. to the thalamus, brainstem, or spinal cord) Neurons in layer IV receive the majority of the synaptic connections from outside the cortex (mostly from thalamo-cortical afferents), and themselves make short-range, local connections to other neocortical layers. It is my duty to refer to the great Hungarian predecessors whenever I can, as Figure 2.2 - showing

the general connectivity of a neocortical column - was depicted by the famous neuroanatomist, János Szentágothai in 1971. Colours of the figure are the following: pyramidal cells (red), cortico-cortical afferent fibers (green), specific afferents (blue), multiple interneurons (black).

While rodent and human brains are similar in many basic ways regarding their elementary building units, comparative studies yielded several differences in the location, sizes and roles of brain structures [31]. In contrast to humans, rat cortex consists only of 100-150 million neurons. Consequently, the width of the rat neocortex is significantly smaller, around 1.5-2 mm and there are no gyri and sulci on its surface. Moreover, the proportion and arrangement of cortical areas are also different in rats compared to humans. Figure 2.3 schematically shows that the rat cerebral cortex (shown in dark blue on the right) has a significantly smaller extent compared to the human cortex.

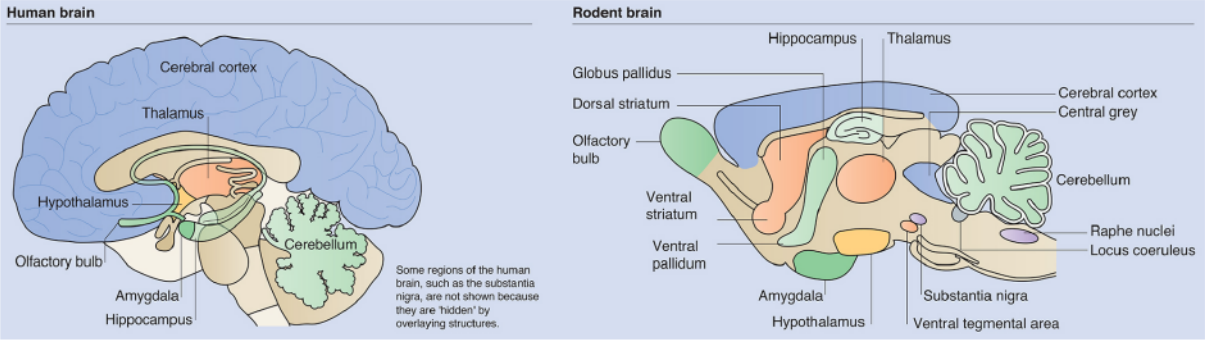

Figure 2.3: Differences and similarities in the proportion and arrangement of human and rat brain areas. Please note the significantly smaller extent of the cerebral cortex (shown in dark blue) in the case of the rat brain [31].

2.1.2 Single neuron electrogenesis: the Action Potential

After describing the basic anatomical and structural features of the cortex, we are moving towards the electrophysiological principles governing the activity of neurons. Basically, input signals received from other (called '*presynaptic*') neuron are terminated mainly on the dendrites (due to synaptic connections) and generated '*postsynaptic currents*' propagate as analogous waves towards the soma. In excitatory connections, currents are depolarising, causing the (originally negative) IC membrane potential to be raised. The EC fluid has a relatively high concentration of sodium (Na^+) ions, while the IC plasma has relatively high potassium (K^+) concentration. In addition, the neuron contains a number of large, negatively charged proteins which give the membrane potential -60-70 mV below the EC fluid (which is considered as zero point or reference). Since postsynaptic currents (and their potentials) decrease over space and time during propagation (plus excitatory and inhibitory currents are cancelling each other), typically tens to hundreds such inputs are needed in a rapid succession to produce a significant

potential change on the soma. If the somatic membrane potential reaches a certain, cell-specific threshold (∼-50 mV), voltage-sensitive Na^+ channels on the soma and on the AIS are activated producing a very non-linear output response, the so called '*action potential*' (AP).

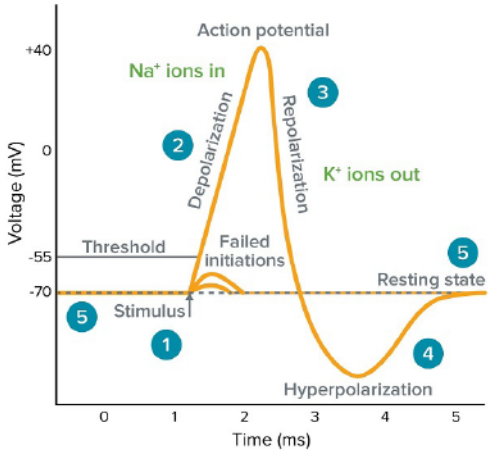

Figure 2.4: Schematic course of a single intracellular action potential (IAP). Numbered steps are detailed in the main text. (Figure was taken from the freely available Axon Guide provided by Multichannel Systems Ltd.)

On Figure 2.4 we can follow the course of one intracellular AP (IAP). Starting from the resting membrane potential (5), if the spatio-temporally integrated inputs are sufficiently large (1), cell becomes quickly depolarised (2) by the more and more incoming Na^+ ions due to the self-exciting effect of Na^+ channel activations. After crossing the zero level (and approaching the equilibrium potential of Na^+ ions) membrane potential stops and turns back to the repolarising phase (3). This is due to both the closing of Na^+ channels and opening of K^+ channels. Inner K^+ ions flow out to the EC space causing a rapid decrease of membrane potential, which now can be even lower than the original state due to the slow deactivation of K^+ channels. This overshooting phase called '*after-hyperpolarisation*' (AHP, 4) then will be followed by an active restoration of the resting state membrane potentials with the help of Na^+/K^+ ion pumps. The whole process is very quick and last maximally 2-3 ms, not including the AHP (also called, the '*refractory period*'), which can last several more milliseconds. IAP is known as a digital process (all or none), the more synchronised excitatory inputs arrive to the soma, the more IAP can be generated (also called '*bursts*', or trains of APs), but the waveform and amplitudes are well-conserved for a given cell type. Generated IAPs then propagated along the axon without any dissipation towards new postsynaptic cells and serve as the output of the presynaptic neuron (that can have either excitatory or inhibitory effect).

Alan Hodgkin and Andrew Huxley described their famous mathematical model in 1952 using a set of non-linear differential equations to explain the ionic mechanisms underlying the initiation and propagation of IAP [32]. To validate their dynamic model, they invented a technique called '*space-clamp*' (there was no patch-clamp at that time) in the squid giant axon (sometimes

funnily misinterpreted as a '*giant squid*' axon, but practically it was a small specimen). For this extensive empirical and computational work, they awarded the Nobel Prize in 1963.

2.1.3 Back-propagating action potential related Ca2+ spikes

The intracellular AP triggered from the axon initial segment (AIS) may propagate back in the opposite direction as well, causing a transient depolarization of the cell body and proximal dendrites [33, 34]. This impulse can travel back effectively along the main apical trunk activating voltage-gated calcium channels and lead to an influx of Ca^{2+} into the IC space. Commonly, single EPSPs from spontaneous synaptic activation are not large enough to activate voltage-gated calcium channels. In contrast, Ca^{2+} spikes can be triggered by NMDA-receptor mediated EPSPs. NMDA-receptors are both ligand- and voltage-gated and they have an additional Mg^{2+} blockade. After neuronal activation (when the neuron fires an AP), the bpAP removes the Mg^{2+} blockade from the receptors due to transient depolarisation. If another, presynaptic neuron releases glutamate simultaneously (or in other words, a spatio-temporally synchronised EPSP arrives to the given dendritic compartment), the NMDA-receptor binds the glutamate and let Ca^{2+} ions inside the cell. Since this process is strictly time-dependent, it may be responsible for the so called long term potentiation (LTP), which is known as the cellular basis of memory formation in the hippocampus.

2.2 Theory behind extracellular potential recordings

Intracellular electrochemical activity of neurons inevitably generates extracellular changes due to transmembrane currents. Currents that are moving between inside and outside of the neuron during its activity can be only indirectly measured extracellularly by their influence on the electrical field. The EC electrode picks these changes up and relays them to an amplifier where they can be measured in respect to a reference. EC potential elicited by transmembrane currents varies dynamically in time and space as numerous currents may be superimposed at a given location in the EC medium [1, 2]. Thus, EC potential contains all the summed signals of multiple synaptic inputs and spiking outputs as well as different local and further (volume conducted) activities in the region where the EC electrode is located [5, 6, 10]. Some of the biophysical principles of EC potential generation are long known [35, 36]. However, there are still many theoretical and experimental open questions that limit the interpretation of EC potential to understand its function [37].

2.2.1 Properties of extracellular potentials

The signals that are measured by the extracellular electrode are very small (typically, three orders of magnitude smaller compared to intracellular) changes of the electrical field potential in the range of tens to hundreds of μV, that need to be amplified. In EC potential recordings, two dominant frequency bands can be extracted representing different information content. For

extracting spiking activity, EC signals are to be high-pass filtered (≥500 Hz) or band-pass filtered (from 500 Hz to 5 kHz). These high-frequency ranges contain an *a priori* unknown number of single- and multi-unit activities (SUA, MUA) stemmed from the immediate vicinity of corresponding contact sites along the EC probe. The nomenclature of SUA in the literature is redundant, since *spikes, extracellular action potentials* (EAPs) and *SUAs* are all frequently used describing the same, cellular-level phenomenon from different point of views. On the other hand, a summed population activity can also be extracted from the lower-frequency part (≤500 Hz) of the EC potential recording, which is often called as *local field potentials* (LFP). Please note that the inaccurate wording of the LFP can be misleading, namely the LFP does not equal to its electric field. In classical electrostatics, the electric field (a vector quantity) is expressed as the negative gradient of the electric potential (a scalar quantity) [2, 10]. Moreover, the LFP cannot be considered purely local as summed and synchronised activities generated by neurons located hundreds of micrometers away from the contact site may also contribute to the measured LFP due to volume conduction. But since the name '*local field potential*' became mostly familiar in neuroscience community, we continue to use this expression. It is probably the "*irony of fate*" that this abbreviation matches perfectly to the 'low-frequency part' of the EC potential, and as a result, LFP has been completely reconciled on this alternative way.

The LFP is originally the same signal that can be measured using macro-electrodes on the surface of the brain (electrocorticogram, ECoG) or even non-invasively on the scalp (electroencephalogram, EEG) due to the above mentioned volume conductive property of the neural tissue. EEG and ECoG signals are considered as spatio-temporally smoothed version of LFP with even lower amplitudes [7, 38].

For a long time, it was thought that only synchronised synaptic events such as EPSPs and IPSPs (excitatory and inhibitory post-synaptic potentials) contribute dominantly to the LFP signal, but recently it has been proven that other, non-synaptic sources are also involved [2, 6]. Recent studies question the widely accepted view that the EAP would be completely independent from the LFP and would not contribute significantly to its generation. It has been proven that the spiking of neurons can notably affect bandwidths of EC signals lower than 200 Hz (which generally belongs to the LFP range). Obviously spiking and synaptic currents cannot be completely separated, as synaptic activity is essential for firing.

For a non-synaptic example, long-lasting (10-100ms) Ca^{2+} spikes during *back-propagating action potentials* (bpAP) can influence the EC potential (and thus the LFP) prominently [34]. These Ca^{2+} spikes are durable (∼10-100 ms) and have a large amplitude (10-50 mV). In addition to bpAP-related Ca^{2+} spikes, bursts of fast spikes are often followed by a larger hyperpolarisation of the cellular membrane due to the activation of Ca^{2+} mediated K^{+} conductances [39]. These earlier mentioned spike after-hyperpolarisations (AHPs) can be as large and as long as synaptic events and thus can contribute to LFP significantly until a frequency of as low as 20 Hz. This contribution can be especially enhanced when numerous neurons are synchronised (e.g. during down-states of slow-wave sleep) [2].

Another important factor to consider as contributors for EC potential generation is the low-pass filtering effect of dendrites[9]. Simulations have shown that high-frequency input (e.g. 100 Hz) given to the distal dendritic part of a pyramidal cell can be detected well extracellularly near the given segment, but at the level of the soma the signal is attenuated with several orders of magnitude, which leads to the high-frequency attenuation of LFP. In contrast, signals (e.g. 1 Hz) with slower frequency are attenuated much less [40, 41, 42]. This low-pass filtering effect results in a consistent property of the LFP, namely that the magnitude of LFP power (or the square of the Fourier amplitude) is inversely related to the frequency f, where the scaling is $1\backslash f^n$ with $1 \leq n \leq 2$.

2.2.2 Current Source Density analysis

The non-local nature of the low-frequency LFP makes the interpretation of EC recordings very challenging. To address this problem, a various source localisation techniques were developed and applied to determine cellular or network origins (by means of active current sources and sinks) of recorded EC potentials in the neural tissue [2, 43]. The key question is whether it is possible (and if yes, then how) to bridge the gap between EC potentials and transmembrane currents. To solve this problem, a physical model called '*current source density*' (CSD) analysis were introduced, which is per definition to estimate the volume density of net transmembrane currents through the neuronal membranes based on EC recordings and its dimension originally is $[A/m^3]$ [8, 44, 45]. Hence CSD is a model-based estimation technique, several approximations and assumptions are to be included *a priori* about the experimental conditions and about properties of the EC milieu, and these constraints will be discussed shortly here.
Historically, many corresponding modelling stages were already described before the construction of the CSD analysis, from the active membrane dynamics (Hodgkin&Huxley, 1952, [32]), to core-conductor theory (Clark&Plonsey, 1966, [46]), dendritic integration (Rall, 1967), generation of EC potentials from single cells (Rall, 1962, [47]) or from populations (Rall&Shepherd, 1968 and Nicholson & Llinás, 1971 [48, 49]), to the description of continuous field theory by Nicholson & Freeman in 1975 [44]). These early investigations allowed for the derivation of the first mathematical transformation (called traditional CSD, or tCSD) estimating the spatial distribution of physiological sources based on recorded EC potentials. The formalism of tCSD described firstly by Nicholson & Freeman (1975) become comprehensively completed by Mitzdorf (1985) [44, 45]. Besides tCSD, improved CSD methods were step-by-step developed by independent researchers in the last year for fulfilling specific aims of different level applications. Calculating the (non-measurable) CSD from the measured EC potential patterns is called '*inverse-problem*', which is known – mathematically speaking – as an '*underdetermined*' or '*ill-posed*' question. While the '*forward problem*' (namely, to calculate the EC potential from known CSD distribution) can be uniquely solved, this uniqueness does not hold *vice versa* and there is an infinite number of equally correct CSD variants for a given EC pattern [50, 51, 52, 53]. In order to squeeze down the unknown parameter space, additional constraints should be imposed

(that is, a parameter will be considered as constants instead of a variable) resulting in a sufficient amount of model reduction, that can guarantee a unique solution. However, these approximations give at the same time the drawbacks or limitations of a particular CSD estimation formula as in many cases, conditions cannot be fulfilled [41, 54]. Starting from the forward-solution, our first general assumption is based on the original quasi-static approximation of Maxwell's equations that the time derivatives of magnetic and electric fields can be neglected, therefore magnetic field $\mathbf{B}$ and electric field $\mathbf{E}$ become decoupled and only capacitive but not inductive effects are allowed.

$$\nabla \times \mathbf{E} = -\frac{\partial \mathbf{B}}{\partial t} \approx 0 \tag{2.1}$$

$$\nabla \times \mathbf{B} = \mu_0 \mathbf{j} + \mu_0 \epsilon_0 \frac{\partial \mathbf{E}}{\partial t} \approx \mu_0 \mathbf{j} \tag{2.2}$$

This means that the electric field $\mathbf{E}$ is only related to the EC potential Φ and can be expressed by its negative gradient:

$$\mathbf{E} = -\nabla \Phi \tag{2.3}$$

(Eq 2.3 nicely shows the historical cause, why we often call the EC potential as '*local field potential*'). From this point on, approaches differ from each other in the way how they model (and add constraints to) the IC sources and the EC medium. Such constraints can be (including but not limited to) the followings:

- Linearity of the EC medium, where σ is the conductivity tensor that still can be a complex value accounting for capacitive effects:

$$\mathbf{j} = \sigma \mathbf{E} \tag{2.4}$$

- Ohmic (resistive) EC medium: Imaginary part of the conductivity σ is assumed to be zero, that is, the capacitive effects of the neural tissue is assumed to be negligible compared to resistive effects. This usually appears to be well fulfilled for the relevant frequencies in extracellular recordings (below 10 kHz).

- Isotropy of the EC conductivity: σ is assumed to be a scalar (same in all directions), i.e., $\sigma x = \sigma y = \sigma z = \sigma$. While this assumption can be true for grey matter, it can be one of the mostly violated simplification for example in the case of white matter.

- Frequency-independence of the EC conductivity: The last assumption also implicates that $\sigma(\omega)$ is constant for relevant frequencies. Its validity is highly debated and this issue is not yet fully resolved and may depend on specific experimental applications.

- Homogenous EC conductivity: EC medium is assumed to have simply the same conductivity everywhere. Again, this can be valid within the cortical grey matter but it becomes questionable when applying it for example to the whole hippocampus.

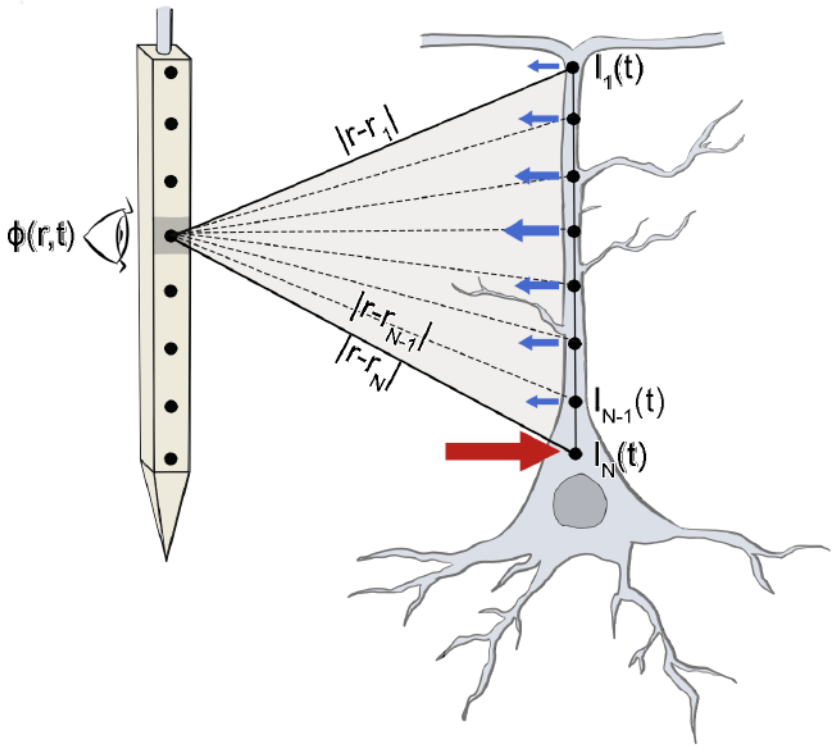

Figure 2.5: Illustration for mathematical formula in Eq. 2.5. EC potential measured at the recording site is generated by the weighted linear sum of net transmembrane currents along a single neuron. The sizes and directions of the arrows illustrate inward (red) and outward (blue) transmembrane currents, whose sum is equals to zero in each time step according to the charge conservation law.

With all of these constraints in mind, transmembrane currents from several dendritic sources can be added up linearly and the general formalism (for N point sources) of the forward model is given as follows:

$$\Phi(\mathbf{r},t) = \frac{1}{4\pi\sigma}\sum_{n=1}^{N}\frac{\mathbf{I}_n(t)}{\mid \mathbf{r}-\mathbf{r}_n \mid} \tag{2.5}$$

Where $\mathbf{I}_n(t)$ is the transmembrane current of the particular n^{th} compartment, and the LFP $\Phi(\mathbf{r},t)$ at $\mathbf{r}_n$ is inversely proportional to the cell-electrode distance as well as to the EC conductivity σ of the tissue. Please note the linear summation of the contributing sources which are individually weighted by their distance compared to the recording point [55, 56].
This Eq. 2.5 is further illustrated on the Figure 2.5, where the sizes and directions of the arrows represent inward and outward transmembrane currents. This schematic figure visually implies an additional law, the 'charge conservation' (or Kirchoff's law) saying that the net transmembrane current on the whole cell (including capacitive and resistive parts) must equal zero:

$$\sum_{n=1}^{N}\mathbf{I}_n(t) = 0 \tag{2.6}$$

DOI:10.15774/PPKE.ITK.2020.005

Consequently, a single '*monopole*' source in one compartment cannot generate any EC potential, since its net transmembrane current necessarily will be zero [10, 57]. The first, simplest possible solution is the '*dipole*' configuration of transmembrane currents in a two-compartmental model (with equal sources). Typically, pyramidal cells in the cortex with long apical dendrites are ordered into layers and can generate strong dipoles. (This arrangement is also called as '*open-field*', since the active sink or source are spatially separated from passive return currents, thus open fields can contribute to the EC potential significantly.)
Furthermore, we can formulate the inverse problem (using the same ohmic EC medium and homogenous, isotropic EC conductivity) as:

$$\sigma \nabla^2 \Phi(\mathbf{r}, t) = -C(\mathbf{r}, t) \tag{2.7}$$

where $C(\mathbf{r}, t)$ is the CSD, and ∇^2 is the so called '*Laplace-operator*' and the equation is analogous to the '*Poisson's equation*' also known from general electrostatics, among others .
For tCSD, we consider a $1D$ (linear) electrode array with constant 'h' inter-contact distance and parallel cell-electrode orientations, then Eq. 2.7 simplifies to:

$$\sigma \frac{d^2 \Phi(z, t)}{dz^2} = -C(z, t) \tag{2.8}$$

Thus the CSD can be calculated numerically as a second order spatial derivative of the measured potential [45]:

$$C(z_j) = -\sigma \frac{\Phi(z_j + h) - 2\Phi(z_j) + \Phi(z_j - h)}{h^2} \tag{2.9}$$

It was already noted by Nicholson&Freeman that this simple formula may be erroneous for small diameters (for local populations) and may not be applicable for single cells at all [44]. Besides tCSD, Somogyvári et al. (2005) invented a model-based inverse calculation method [58]. Then Pettersen et al. (2006) introduced the iCSD technique, which was then expanded to three-dimensions by Leski et al (2011) [8, 59]. Later on, kernel CSD (kCSD) by Potworowski, Wójcik and colleagues (2012) generalised the iCSD allowing arbitrarly chosen electrode grids and handling the corruption of noise [60, 61]. In the same year, Somogyvári et al. (2012) proposed the spike CSD (sCSD) which was especially tailored for single-cell calculations but firstly with unknown (and thus simplified) morphology [5]. sCSD uses an additional trick (called the auto-focus algorithm) to find the cell-electrode distance and thus to provide the most realistic CSD solution for the inverse-problem [5]. Lastly, single-cell kCSD (skCSD) – which was published recently using the experimental results of this current thesis – is an application of kCSD framework while assuming that the measured EC potential (or its so called '*spike-triggered average*', STA) comes from a particular cell with *a priori* known morphology and known cell-electrode distances [62]. Using a one-dimensional parametrisation of the branching structure of dendrites (based on the so called '*Chinese postman problem*' from graph theory), this is the first (and until now, the only) published CSD method taking into account

the complicated and realistic morphology of a single neuron. First experimental application of skCSD method on recorded ground-truth data will be discussed in details in Section 4.2.7 of the II. Thesis (4.2) and in the relating co-authored publication in Cserpán et al. (2017) [62].

All in all, the above listed strategies have been successfully used to identify CSD distributions based on recorded EC potentials. When interpreting CSD, it is still unclear yet whether the current reflects an active synaptic current or a passive return current. The inclusion of anatomically identified input regions helps to decide which option may be valid, but unfortunately, ambiguity may remain present if the currents are the result of non-synaptic events or any of the several assumptions becomes violated.

2.2.3 Relationship between IC and EC signals

As it was already introduced, spikes (or EAPs) are the extracellularly detectable equivalents of intracellular action potentials (IAPs). In the first depolarization phase, the rapid Na^+ ion influx generates a sink in the EC medium that causes a large amplitude negative peak in the measured EC potential. In the subsequent repolarization phase, the migration of K^+ ions into the EC space is slower, but it can decrease the IC potential even below the resting state level and often results in an overshoot (AHP), which is considered as a EC source and indicates a lower amplitude positive wave component in the EC signal. It is worth to clarify the (sometimes ambiguously referred) sign convention and corresponding colouring of LFPs and CSDs. Negative CSD value represents a sink, when cations flowing into the cell and leaving the EC medium. Even if (from the EC point of view) the values are negative here, standard colour for sinks is reddish to highlight increased (depolarised) neural activities. Likewise positive values stand for a source, when cations enter the EC space, but the colouring here is blue since we are focusing on the decreased (hyperpolarised) ongoing neural activities.

Figure 2.6 shows data collected by Henze et al. (2000) of averaged EAP from CA1 pyramidal cell, which consists of an initial large negative deflection followed by a smaller and wider positive peak, while the simultaneously recorded IAP is completely its opposite with a large positive peak and a smaller negative part [3]. The temporal relationship is examined by overlapping the two waveforms. It can be observed that the EAP negative deflection corresponds to the depolarizing phase of the IAP and the later positive peak corresponds to the repolarizing and after-hyperpolarizing phases of the IAP. Studies have shown that the shape of the EAP waveform is not only qualitatively, but quantitatively similar to the IAP and it can be approximated by the negative of the temporal derivative of the intracellular somatic voltage: $V_{EAP} = -dV_{IAP}/dt$. When superimposing the negative derivative of the IAP on the EAP traces, waveforms are fitting relatively well during the initial deflection, but there is a mismatch on the further phases, the IAP derivative precedes EAP and follows a faster route. The assumed reason for the deviation is that the EAP in the later stages is impacted by complex properties like neuronal morphology and varying ionic conductances [63]. The quantified connection between the temporal properties

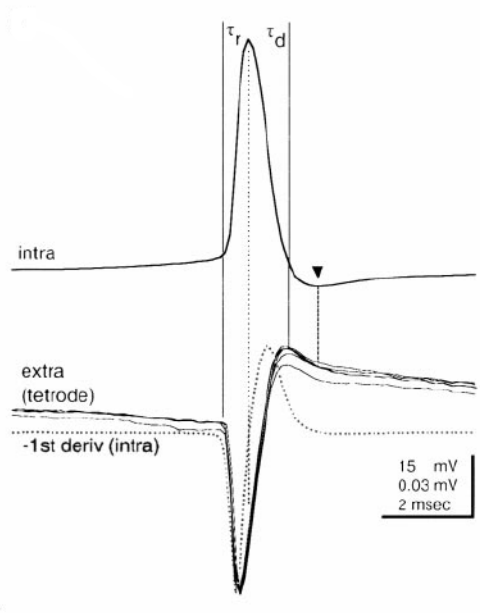

Figure 2.6: Averaged IAP and EAP recorded from CA1 pyramidal cells, and the negative of the first derivative of the IAP is superimposed [3]

is the following: averaged EAP started 0.01 ms and ended 0.02 ms earlier than the corresponding IAP, and interestingly, the negative peak of the EAP preceded the IAP by 0.2 ms. A speculative solution would be if the EAP captured the axon initial segment (AIS) during action potential generation while IAP only represented the somatic contribution to the generated action potential [5, 64].

Researchers have tried to identify interneurons and pyramidal cell types based on examining various EC waveform parameters when IC ground-truth data was not available [65, 66, 67, 68]. Waveform classification of EAPs based on spike durations (or spike half-time duration) can provide clear separations of putative cell types resulting in a one-dimensional, bimodal distribution for all clustered EAPs. In the study of Barthó et al. (2004), the EAP duration of the putative interneurons was significantly faster (0.43 ms $\pm$0.27 ms) than for putative pyramidal cells (0.86 ms $\pm$0.17 ms) [66]. This result implicated that interneuron spikes are narrower in average, which statement has been several times confirmed over time [11, 68, 69]. In extreme cases, even neuronal subtypes can be inferred (with the help of anatomical data and by considering more parameters), such as short-duration and large frequency spikes from cells whose somas are located in the pyramidal layer are typical for perisomatic interneurons (putative basket cells or chandelier cells). In contrast, spike durations of O-LM interneurons are very heterogeneous and they cannot be easily distinguished. Regarding spike-spike interactions in term of cross-correlations in the recorded network, findings indicate that signal transmission occurs more frequently between interneuron-pyramidal cells, rather than among pyramidal-pyramidal cell pairs, but this statement may vary trough different region of interest. Such a waveform based cell type classification will be also performed in this dissertation in Section 4.1.5 of the I. Thesis (4.1).

2.3 Repertoire of extracellular multi-channel recording techniques

We have learned in previous sections that electrical nature of neuronal activity allows the detection of current-generated voltage changes using EC probes. Novel technologies allow us for choosing from a wide range of electrode designs, such as metal wires, silicon-based probes, multielectrode arrays (MEAs), etc. There is a constant challenge in the development process to fulfil two mutually exclusive conditions, namely keeping impedance values low and contact sites small at the same time [12]. An additional crucial factor which should also be taken into account is the choice of material used in fabrication, because it mostly influences the basic properties of probes: the motility, softness, stability, toxicity, bio-compatibility, etc. [70, 71]. In the following subsections I overview the development of recent recording techniques enhancing their ongoing challenges and opportunities in different in vitro and in vivo applications.

2.3.1 Historical aspects

In the beginning, electrophysiological recordings have been started to access a few cells in the brain using single tungsten wires [72]. These electrodes consisted of an insulated metal wire except for the wire tip which represents the recording site. The wire electrodes have a tapered structure to enable convenient insertion in the brain tissue. The tapered structure can be achieved by dipping the wires into an etching solution (e.g. NAOH) and slowly drawing out the electrode from the solution. Typically used electrode materials include platinum, iridium, platinum-iridium, gold, stainless steel or tungsten [19, 73, 74]. For insulation of these electrodes, quartz glass, Teflon, polyimide, and Parylene materials can be used. The insulating materials ideally should have a high dielectric constant in order to minimize stray capacitances affecting the electrode during recording. A multi-channel probe of these insulated wires can be made by gluing individual metal wire electrodes together. These are called '*stereotrodes*' (two electrodes), '*tetrodes*' (four electrodes), or cut-off wire bundles with multiple electrodes [3, 75, 76]

2.3.2 Batch fabricated silicon probes

Thanks to the cross-disciplinary development of the silicon-based batch manufacturing technologies, multi-channel silicon probes became available in a wide variety of shapes, layouts with submicron reproducibility and with only low restrictions regarding their physical configurations [19, 71, 77]. In addition, the number of contact sites placed on a single shank increased exponentially from 8-16-32 channels (firstly called '*polytrodes*' [78]) up to more than a thousand of channels (probes developed by international Neuroseeker and Neuropixels consortia [11, 79, 80, 81, 82]). In the past few years, countless examples were published applying different geometries for site layout or novel shank designs [11, 81, 83, 84, 85, 86, 87, 88]. The use of bulk micromachining is not only cost effective and reproducible, but one can also obtain an active probe with on-probe signal processing or pre-amplification to significantly reduce the inherent

noise [80, 82]. Inclusion of integrated circuits is also advantageous to reduce the overall size of the recording system.

The fabrication of silicon probes includes the following steps: deposition of a metal layer on an insulated substrate and patterning the metal layer to form contact sites, read-out pads for connecting to the external circuitry, and interconnecting traces between the recording sites and read-out pads [89]. An insulating layer is then deposited over the whole structure and patterned to open access above the recording sites and bonding pads. The substrate must be biocompatible, mechanically stable and strong enough to penetrate the pia mater and then to deeper tissue. These well-recognised properties of silicon made it suitable to become a gold standard material in neural interface industry. The two most famous examples of silicon probes are the '*Michigan-type probes*' and the '*Utah-arrays*' [90, 91]. The latter one is also among the few probes with FDA license for human clinical applications [92].

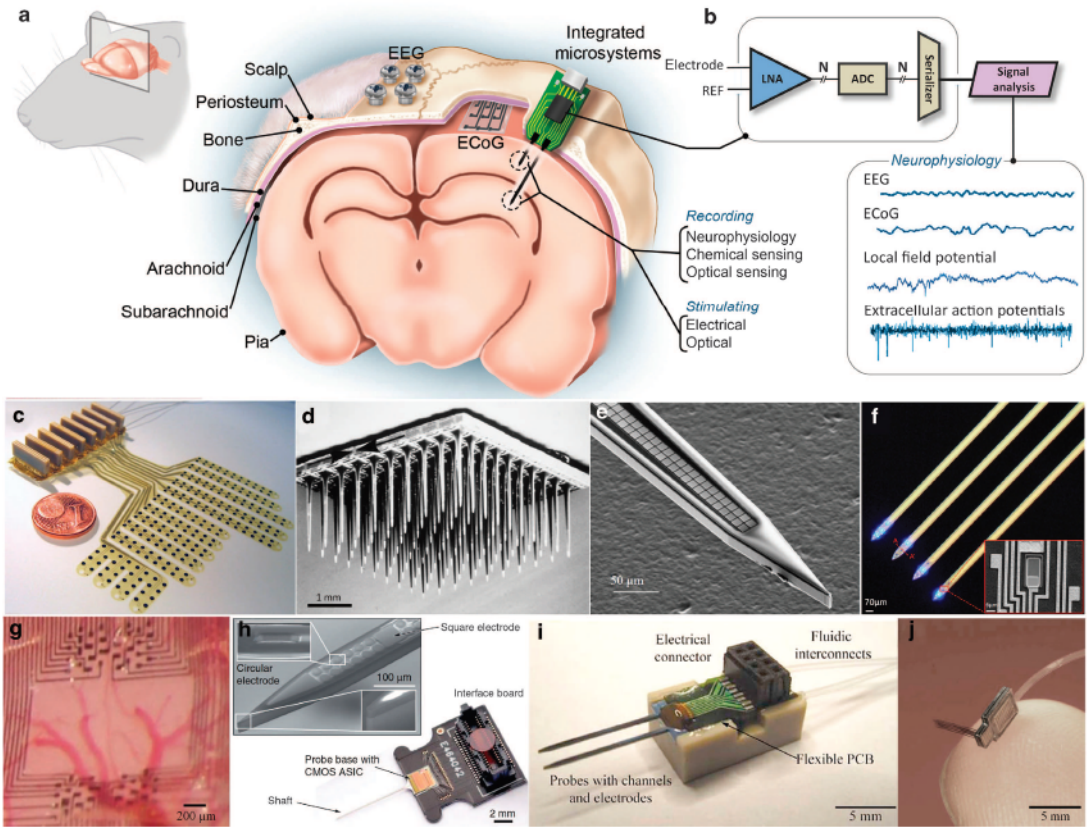

Figure 2.7: Illustration of the rodent brain (a) and a variety of technologies from EEG to intracortical microelectrodes. (b) High-density systems with built-in active electronics to pre-process large data streams and reduce the size of the connectors. Sample electrical signals show the amplitudes of various signal sources. (c) Polyimide soft ECoG for large area mapping. (d) A 'Utah-array' (e) Close-packed contact sites on a multi-channel silicon probe (f) MicroLED optrode made from GaN on silicon. (g) Parylene ECoG with single-cell capabilities. (h) CMOS integration (i) Microfluidic probe for drug delivery. (j) Active 3D silicon probe with flexible parylene interconnect. Figure is taken from the review of Seymour, Wise and colleagues (2017) [71].

Figure 2.7 summarises these extracellular recording techniques with their different degrees of invasiveness. Figure is taken from the review paper of Seymour et al. (2017) [71]. Among others, a Utah-array is shown on Figure 2.7/D and a soft Parylene ECoG array is shown on Figure 2.7/G.

Beyond single- or multi-shank implantable (or needle-like) silicon probes planar '*Multi-Electrode Arrays*' (MEAs) were also developed and specialized for *in vitro* cell cultures, retinas and brain slice applications [93, 94, 95, 96]. These MEA systems are made of using complementary metal-oxide-semiconductor (CMOS) technologies enabling several thousands of contact sites with ultra-high density spacing. While the vast majority of MEA systems have planar forms, 3-D structured protruding MEAs were also developed for penetrating studies [97, 98]. These types are especially useful in slice recordings where electrodes have to manage to record neural activities below the surface dead-cell layer of the brain slice.

2.3.3 Polymer-based soft probes

Different biocompatible polymers such as '*polyimide*', '*Parylene-C*', '*SU-8*' or '*polydimethyl-siloxane*' (PDMS) are used to cover the metal and silicon region of the probes to form a biocompatible interface between the probe and the brain tissue [15, 99, 100, 101]. Polymer materials are also used for the interconnect cables even in combination with Utah-arrays or Michigan-type probes. However, the bonding methods are often unconventional and non-trivial for connecting the polymer cables with the microfabricated silicon probes. Glassy carbon (GC) electrodes can be used on these ultra-comformable polyimide based probes typically for minimally invasive MR-compatible or μECoG configurations [102, 103]. The main advantage of flexible materials is to provide smoother coupling with the soft tissue, as they are able to follow small motions and pulsations of the brain [104]. This may result in a less severe immune response and moderated glial scar formation around the flexible probes compared to silicon based probes [15].

Moreover, synthetic and organic conductive polymers (CP) can also be used as biosensors of electrochemical signals (resistance, impedance, or electric potential) [105]. Especially, Poly(3,4-ethylenedioxythiophene), commonly called PEDOT has been the subject of great interest because of its beneficial properties such as high-conductivity and transparency in its doped state. The most commonly used counterion for PEDOT electropolymerization is Polystyrene sulfonate (PSS) [106] It is important to note that the biocompatibility of these conductive polymers was also proved to be improved compared to semiconductor or metal-based probes [107, 108].

2.4 "Renaissance" of optical imaging techniques in neuroscience

Optical microscopy has been a commonly used system of lenses stemmed from the 17^{th} century. However, two independent discoveries in the last decades have revolutionised the use of light in research, especially in neuroscience applications. '*Fluorescent laser scanning microscopy*' and '*optogenetics*' were these two transformative technologies providing dramatic recent progress in both to control and read-out neural activities, *in vivo*. General advantages of using light are obvious: it is basically non-invasive (unless the carrier is invasive, as in the case of '*optrode*' or '*fiber photometry*'), can be precisely targeted, can be adjusted between multiple wavelengths, and can report the presence or activity of (otherwise invisible) selected molecules in the living brain. In the following subsections, I introduce both the read-out part and control part, focusing on specific methods used in the current thesis work.

2.4.1 Two-photon laser scanning microscopy

'*Two-photon laser scanning microscopy*' is a fluorescent imaging technique based on the physical effect of two-photon (2P) excitation. Although the 2P absorption was firstly described theoretically by a famous woman physicist, Maria Göppert-Mayer in the early 1930s, it was applied experimentally for microscopic usage only in 1990 by Wilfried Denk, Watt Webb and colleagues [109]. Today, 2P imaging is a widely used complementary technique besides electrophysiology for the acquisition of neural activity with single-cell resolution from hundreds of neurons both *in vitro* and *in vivo*.

One of the main areas this imaging technique is used is the measurement of Ca^{2+} changes in neurons as a proxy for intracellular action potentials [110]. A prominent advantage over other techniques is the use of dyes that change dynamically with the intracellular Ca^{2+} concentration. Firstly, fluorescent microscopy only provided static (or structural) information of the investigated tissue via '*green fluorescent protein*' (GFP) based fluorescence, but more recently, tracking of Ca^{2+} dynamics by 2P microscopy allows for functional imaging and tracking physiological processes almost in real time [111].

Excitation by two-photon effect is based on the physical principle that two, comparably lower-energy photons are able to activate one fluorophore molecule, instead of the conventional excitation by the energy of only one photon. The fluorophore will then decay back to its fundamental state by emission of a photon of somewhat lower energy than the sum of the two exciting photons. Traditionally, conventional fluorescent microscopy - when applied to thick (over $\sim$100 μm) samples- suffers from the shortcoming that the fluorophore is excited in a comparatively large volume, giving rise to a large out-of-focus component in the fluorescence reaching the detectors. '*Confocal microscopy*' overcomes the problem by using a pinhole to reject the photons originating from all locations other than from one point in the focal plane, providing an optical section of the tissue sample [112]. Although out-of-focus photons do not contribute to imaging,

corresponding fluorophores are still excited leading to high putative photodamage and photobleaching during scanning. In addition, the use of pinhole implies that there will be a loss of "good photons" as well, that were indeed emitted from the in-focus-point, but underwent scattering on their way out of the tissue. In 2P microscopy, however, all emitted photons are useful, that dramatically increase the signal-to-noise ratio (SNR) compared to confocal microscopy, where scattered photons are rejected. Similarly, photodamage and bleaching is greatly reduced, since the probability of fluorophore excitation depends quadratically on light intensity, rather than linearly as in the case of confocal fluorescence [113]. Thus sufficient excitation occurs only where the local concentration of photons is very high, which is essentially true only at the focal point of the microscope. To achieve this, 2P imaging requires a high power femtosecond pulse synchronised lasers. These (typically, Ti:Sapphire based) lasers yield outputs of 1-4 W average power (depending on the chosen wavelength range). This power can be enough for imaging the tissue with a depth of hundreds of μm up to even 1 mm.

Emitted fluorescence is collected by lenses, then separated by wavelength using '*dichroic*' mirrors and colour filters from the applied near infra-red (NIR) light source, and become finally detected by '*photomultiplier detectors*' (PMTs) [114]. Generally, single-photon imaging techniques use fluorophores that are activated in the 400-500 nm (visible) wavelength range, but for 2P excitation this range falls into the NIR ranges (between 700-1300 nm) resulting in a higher possible penetration capability. Lower energy, longer wavelength excitation is rather suitable for *in vivo* chronic imaging of living animals, as it causes less phototoxicity.

2.4.2 Optogenetics

As mentioned in the section introduction, optogenetics can be used both to read-out (or to monitor) and manipulate (or control) the activity of neurons. The word "optogenetics" stemmed from the combination of genetic targeting and optical interrogation.

On the read-out side, highly sensitive protein based molecular probes were developed to transform electrochemical activity of neurons into detectable light. In the case of in vitro recordings, neurons can be labelled by fluorescent dyes that diffuse inside the cell through a micropipette or bulk loading due to perfusion. More recently, genetically encoded indicators can also be used via viral transfection or with transgenic breeding strategy. Some of the established '*genetically encoded calcium indicators*' (GECIs), such as Thy1-GCaMP6 has the potential of single spike sensitivity across multiple regions in the cortex [115]. Thy1-GCaMP6 will also be used in this current thesis work in the I. Thesis (4.1), in Section 4.1.4 and in the III. Thesis (4.3), in Section 4.3.3 and 4.3.5. Although GECIs are certainly useful in 2P imaging, their kinetics is relatively slow (with rise times of hundreds of milliseconds). And this is getting even worse if larger field-of-view needed, since there is a trade-off between spatial and temporal resolution which results in a vast under-sampling of single IAPs (whose time scales are between 1-3 ms).

Further, novel reporter molecules were designed recently for detecting not only Ca^{2+} as previously established (which is only indirectly related to IAPs), but also for other specific ions and

even IC membrane voltage [116]. Genetically encoded voltage indicators (GEVI) perform better in sub-cellular sensitivity compared to GECIs and have faster kinetics, comparable to IAPs. Therefore the use of GEVIs can be another game-changing revolution for future neuroscience, since they could non-invasively substitute invasive electrophysiological recordings, while also providing geometrical information about the sources and chronic tractability. But to this day, GEVIs are only occasionally used in a few laboratories for testing their biocompatibility and optimizing their features and long-term stability. To take maximal benefit from the ultra-fast kinetics of GEVIs, new type of scanning method is also to be invented, as traditional 2P microscope scanners cannot compete with kilohertz scanning frame rates required for sampling [117]. On the manipulation side, a palette of proteins for both activation and inhibition have been identified and optimised in the last years. The inventors, Ed Boyden and Karel Svoboda (among others) awarded the Brain Prize in 2013 for their pioneering work in this field [118]. Optogenetic tagging is based on light-sensitive proteins called '*opsins*'. The original, wild-type opsin called '*channelrhodopsin*' (ChR) was isolated intriguingly from unicellular algae (they used it for movement via '*phototaxis*'). ChR is naturally able to function as a light-gated ion channel and variants were cloned and engineered to be sensitive for different colours or to have exciting or inhibiting effect in response to light stimulation. However, a number of technical issues must be addressed here as well, to fluorescent indicators to exploit the full potential of optogenetics, including local delivery of well-focused, low-intensity light, application of appropriate stimulus waveforms, and the replacement of large bench top lasers to small, head-mounted LEDs or laser diodes [119].

Within the research of the current thesis, only read-out methods will be used by recording spontaneous single-cell and population activity without any local optogenetic manipulation. All in all, optogenetics and stimulation can provide a comprehensive tool-kit for testing causal roles of specific neuron types or (by applying inhibition) to conduct millisecond-precise 'loss-of-function' experiments in living neural circuits [120].

2.5 Challenges and opportunities in current recording techniques

While all of these devices gained significant impact on the discovery of neural circuitry and dynamics, numerous questions remain mostly unanswered about their limitations and interpretation of recorded signals [2, 6, 7, 121, 122]. It is critical to demonstrate the recording capabilities and to define the limits of a certain probe to understand how neuronal signals are transformed and transmitted during the acquisition [122, 123].

2.5.1 Design issues and biocompatibility aspects

There is an inherent risk, which must be undertaken during each electrode implantation. Penetrating probes unavoidably cause tissue damage, blood vessel rupture and a certain level

of inflammation with corresponding immune response [15, 124]. These are bad news both from the point of host tissues (animal or human patient) and from the point of the quality of recorded signals. The initial reaction can progress into a chronic foreign-body response with glial scarring leading to an isolated probe environment, and consequently, to a dramatically declined SNR.

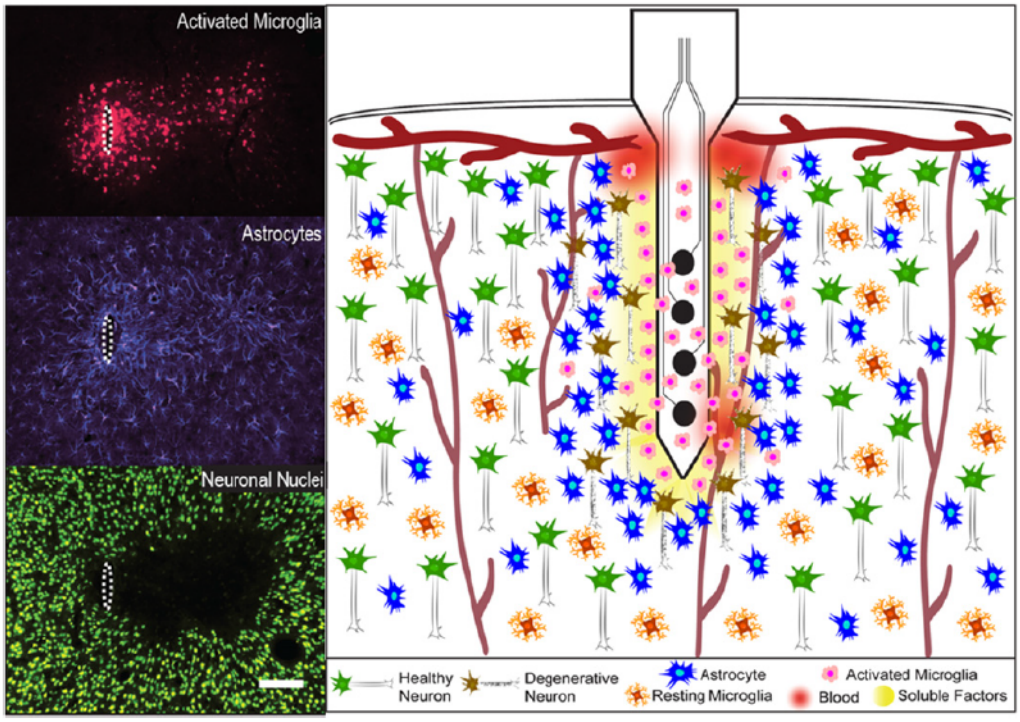

Figure 2.8: Acute and chronic cellular events around an implanted silicon probe. On the left, immunohistochemical sub-figures shows the distribution of dominant cell types in the vicinity of the probe track. Figure is taken from the review of Jeffrey Capadona and colleagues (2014) [125].

Figure 2.8 schematically depicts cellular events around an implanted silicon probe. On the left, immunohistochemical sub-figures shows the distribution of dominant cell types in the vicinity of the probe track. Figure is taken from the review of Jeffrey Capadona and colleagues (2014) [125]. The formed high-impedance glial encapsulation sheath is one of the major hurdles for seamless and chronic neural interface design [13]. Moreover, variability in histological results and conflicting published conclusions in recent years made it difficult to disentangle the main contributors of observed failure modes [16, 126]. This ongoing challenge of chronic integration places a heavy burden on multi-channel electrode design. There are numerous intrinsic and extrinsic material properties to be considered for mitigating inflammatory processes. Intrinsic probe properties, among others consist of impedance of contact sites, shank flexibility, material strength, and chemical stability, while extrinsic parameters are probe geometry, insertion strategies, applied bioactive drugs or packaging.

Similarly, in the case of *in vitro* recordings, establishing a tight seal between the cell culture (or brain slice surface) and the planar MEA probe becomes a difficult proposition due to dead-cell

layers leading to loss of synaptic inputs (via cut-off dendrites), poor SNR, or the possibility of aberrant recordings, and signal contamination [19, 122]. Continuing this line, metal-based microelectrodes are also affected, since these probes can record activity only at their exposed tip. Increasing the number of contact sites requires a linear increase (in case of passive probes, without multiplexing methods) in overall probe size and thus causes an undesirable amount of neural tissue damage. Further, it is difficult to insert a high-density needle array accurately into a small volume of brain tissue due to tissue deformation. We discussed the main advantage of metal electrodes, which is the simplicity of their manufacturing. But this simplicity also leads to their disadvantage: the lack of common standards and automation in probe manufacturing from one lab to other. Lastly, polymer based softer probes showed improvements in reducing microglial activity, however they also suffer from several discrepancies.

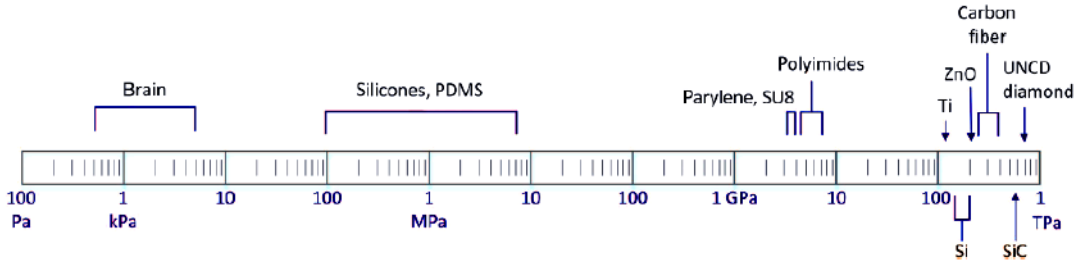

Figure 2.9: Log scale of Young's modulus for many substrates used in implantable arrays. Please note, how far are even the polymer materials from the original stiffness (or rather, from the softness) of brain tissue. Figure is taken from the review of Seymour, Wise and colleagues (2017) [71].

There is a remarkable difference in the '*Young's modulus*' (a mechanical property that measures the stiffness of a solid material) of the tissue and implanted probes, which still holds for elastic and soft materials. Figure 2.9 list all materials mentioned with their corresponding Young's modulus. It is clear from this 1-D comparison, that none of them can even approach the softness of the brain tissue, which may result in further (post-implantation) tissue damages caused by electrode drift [104].

Complications are present in the case of optogenetic indicators and modulators as well. An aberrant activity was found for GCaMP6 in numerous independent labs concerning its putative phototoxicity [127]. These Ca^{2+} based indicators also have singificantly slower time-resolution and kinetics compared to EC recordings or voltage-sensitive dyes and GEVIs. On the other hand, optogenetic stimulation can similarly induce pathophysiological response via bulk illumination of too large areas. Millisecond precise synchrony of large population activities appears to be unnatural in mammalian neural circuits. However, it is a non-trivial task to properly calibrate stimulus waveforms and frequencies and the responses are highly variable across experimental trials. For ChR expression, researchers also found abnormal axonal morphologies after either virally driven or *in utero* electroporation [128]. It has to be mentioned that experimental limitations, such as the contamination of background fluorescence in densely labels tissue (e.g. dentate gyrus) or optical aberrations can also hinder good resolutions and signal

quality in microscopic recordings, even if optical indicators are optimized [122]. In addition to this, deeper subcortical structures (such as hippocampus, basal ganglia or brainstem nuclei) remained very hard to approach (especially in larger species, eg. in non-human primates) by conventional imaging techniques due to limited penetration capabilities. A further experimental contamination can be the so called '*photoelectric artefact*' when EC electrophysiology and laser scanning imaging are both applied in the same field-of-view (FoV). The photoelectric effect is a generation of free electrons in the conductive material upon exposure to light energy, first observed by Becquerel in 1839 (also known as '*Becquerel-effect*'). Further literature also distinguishes between '*photovoltaic*' and '*photoelectric*' effects. The otherwise well-known photoelectric effect is unexpectedly prominent when coherent, high-energy light sources (such as 2P lasers) are used and can strongly contaminate recorded signals. The artefact remains present even in the out-of-focus range or outside the actual FoV of the imaging due to light scattering in the tissue, however its amplitude decreases over distance. Since photoelectric artefact is a material dependent property, transparent polymers are much less affected during laser imaging, and ionic conductors (such as patch-clamp pipettes) almost completely resistant to its generation. Nevertheless, it is an ongoing issue for silicon probes, how to mitigate photoelectric effects and combine multi-modal signals on the same media.

We could not cover all the aspects of neural interface design here, however, in the I. Thesis (4.1), Section 4.1.2, several more design principles for silicon probes will be taken into account and discussed in further details. Further, an in-depth experimental realisation will be presented for mitigating photoelectric effects during co-localised EC and 2P recordings within the III. Thesis (4.3) in Section 4.3.3 and 4.3.5.

2.5.2 Review of ground-truth recordings

In Table 2.5.2 I summarise all known and published attempts in the literature for co-localised and simultaneous IC-EC recordings ($n = 15$, rows). These previous literature results can be considered as real ground-truth datasets. Comparison was made based on 8 different criteria (columns). As a last row, ground-truth data provided by this thesis was also listed here (for detailed description of the recording method, please see II. Thesis group in Chapter 4.2) to show similarities and differences compared to these studies. As a walk-through, I list the *pros* and *cons* of all literature attempts to fit my thesis work into the grand picture.

In their early pioneering study, Freygang and Frank (1959) started to record simultaneous signals inside and outside the soma of a motoneuron in order to estimate the relationship between intra- and extracellular waveforms [36]. Wehr, et al. (1999) were the first who used metal electrode in simultaneous recordings, however the famous study from György Buzsáki's lab, conducted by Henze, et al. (2000) became the most widespread since they provided the first open-source, easy-to-use ground-truth dataset with included morphology [3, 129]. It is

worth to note, that Wehr, et al. (1999) recorded their data from locust (or grasshopper), which made their findings less applicable to data obtained in later mammal species. Cohen, et al. (2000) published similar datasets to Henze's work but using *in vitro* slices from guinea-pig. Interestingly, it has been one and a half decade when next studies could replicate first results of the Buzsáki's lab. Anastassiou, et al. (2015) were the firsts in using multi-channel silicon probes in co-localized and simultaneous recordings [130]. However, they investigated only one or few neighbouring EC channels in every recording session (they picked mainly the channel with the highest spike amplitude, which - in the majority of cases - corresponds to the contact site placed closest to the soma) for comparing IC and EC properties across different cell types in cortical and hippocampal slices of rats. In the same year Franke, et al. (2015) published a dual patch-clamp + EC study to validate spike sorting in the case of overlapping spikes [131]. (For the records, they also published a prior simultaneous work with single patch-clamp in 2010 [132]). From that time, experimental directions suddenly proliferated due to new technological developments. Vardi, Jäckel and Yger and colleagues recorded *in vitro* ground-truth signals using planar high-density MEA systems placed below the cultured tissue or brain slice [133, 134, 135]. While other attempts from groups of Adam Kampff and Ed Boyden were able to record high-density simultaneous data, *in vivo* [21, 22, 136]. Similarly, Daniel English et al. (again from Buzsáki's lab, 2017) collected IC-EC data from paired interneurons and pyramidal cells, *in vivo* combined with optogenetics [137]. Here, these last studies were often restricted to record juxtacellular (JC) or loose-patch (LP) instead of whole-cell (WC) configuration and the exact localization of cell-electrode distances became very challenging (none of them included morphological information into their *in vivo* dataset). Most recently, Hunt and colleagues presented a micropipette-integrated tetrode design for comprehensive validation of spike sorting algorithm [138]. With their paired probe, co-localised and simultaneous data acquisition becomes faster and easier to implement, however, the user is again restricted regarding the number of EC contact sites.

In this thesis I provide a hybrid approach, using multi-channel, penetrating silicon probes, but *in vitro* slices, completed with whole-cell patch-clamp and reconstructed 3D cell-electrode positions and morphologies. This study is mostly similar to work of Anastassiou et al. (2015), except I use laminar EC probes (instead of Buzsáki-type polytrodes), and I will focus on multiple (≥ 4) EC contact sites, plus the acquired data will be published together with this thesis to become a continuously growing open-source dataset (unlike Anastassiou's work) available for testing future data analysis methods and model-based calculations (such an application will also be presented here in the II. Thesis group (4.2) in Section 4.2.7).

DOI:10.15774/PPKE.ITK.2020.005

Reference	Experiment	Animal	EC	IC	Putative cell types	Morphology included?	Can be spike sorted?	Data available?
Freygang59 [36]	*in vivo*	cat	pipette	pipette	PC	No	Not indicated	No
Wehr99 [129]	*in vivo*	locust	tetrode	sharp	Not indicated	No	Yes	No
Cohen00 [139]	*in vitro* slice	guinea-pig	single wire	sharp	PC + IN	No	No	No
Henze00 [3]	*in vivo*	rat	single wire and tetrode	sharp	PC (only 1 IN)	Yes	Yes	Yes
Chorev12 [140]	*in vivo*	rat	single wire	WC	PC	Yes	Yes	No
Anastassiou15 [130]	*in vitro* slice	rat	32 ch NeuroNexus Buzsáki probe	WC	PC + IN	Yes	Yes (only 1 ch shown)	No
Franke15 [131]	*in vitro* slice	rat	tetrode	dual WC	PC	No	Yes	No
Neto16 [136]	*in vivo*	rat	32 ch NeuroNexus probe + 128 ch Neuroseeker probe	JC	PC	No	No	Yes
Vardi16 [133]	*in vitro* culture	rat	60 ch planar MEA	WC	Not indicated	No	No	No
Jäckel17 [134]	*in vitro* culture	rat	11011 ch planar MEA 126 read-out ch	WC	Not indicated	Yes	Not indicated	No
English17 [137]	*in vivo*	mouse	32 ch and 64 ch polytrodes + with optogenetics	JC	PC + IN	No	Yes	Yes
Allen18 [22]	*in vivo*	mouse	1000 ch custom-made probe Scholvin et al., 2016 ([86])	JC, LP, WC	Not indicated	No	Yes	Yes
Yger18 [135]	*in vitro* retina	mouse and rat	252 ch and 4225 ch planar MEA	LP	RGC	No	Yes	Yes
Marques-Smith18 [21]	*in vivo*	rat	960 ch Neuropixels probe 384 read-out ch	JC, LP, WC	PC + IN	No	Yes (only a few)	Yes
Hunt19 [138]	*in vivo*	mouse and rat	pipette integrated tetrode	WC	Not indicated	No	Yes	No
This thesis	*in vitro* slice	rat	16 ch NeuroNexus probe and 32 ch custom-made spiky probe	WC	PC (only 1 IN)	Yes	Yes (only a few)	Yes

Table 2.1: Overview of all published attempts in the literature for co-localised and simultaneous IC-EC recordings. Abbreviations: extracellular (EC), intracellular (IC), multi-electrode array (MEA), channel (ch), pyramidal cell (PC), interneuron (IC), retinal ganglion cell (RGC), juxtacellular (JC), loose-patch (LP), whole-cell (WC) recordings.

DOI:10.15774/PPKE.ITK.2020.005

Chapter 3

Materials and methods

3.1 Silicon probes used for *in vitro* extracellular recordings

We have seen a large variety of devices developed for multi-channel EC recordings in Background section 2.3. From this repertoire I use the following squeezed list of features in future experiments:

- acute rodent
- *in vitro* brain slice
- laminar (1D) contact sites
- silicon or steel shank
- penetrating or surface
- polytrodes (16-32 channels)

Recordings were carried out with three different multi-channel microelectrodes that met the above criteria. In the next subsections, I list the dimension of all variants and main pros and cons of their specific design.

3.1.1 *'The hockey-stick'*: Plexon U-type, 24-channel, angled surface probe

The U-type *in vitro* probe is a modified version of an originally *in vivo* multielectrode also used in human intra-operative studies [73, 74, 92, 141, 142]. This very robust probe consists of 24 embedded wires with single contact sites arranged in a row. The inter-contact distance is 50 μm and sites have relatively small impedance magnitudes. The shank was angled to arrange the contact sites parallel (horizontal) to the recorded slice. Therefore, this probe cannot be inserted, it can only be placed onto the surface of the slice. Over its robustness and easy-to-use formation, the surface nature is one of the biggest disadvantage of this probe. As we discussed earlier in Background section 2.5.1, surface of the slice is considered a dead-cell layer and it heavily attenuates single unit activities generated in deeper tissue, but it can be

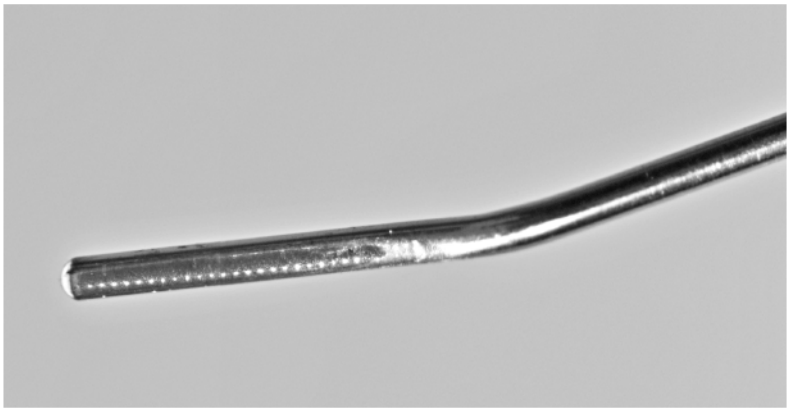

Figure 3.1: *'The hockey-stick'*: Plexon U-type, 24-channel, angled surface probe.

easily used for volume conducted population activities, e.g. for LFP gradient recordings. This probe was developed by István Ulbert and László Papp (Neuronelektród Kft, Hungary) and commercialised by Plexon Instruments (U-type probe, Plexon Inc., Texas, USA) [73, 74, 92, 142].

3.1.2 *'The comb'*: NeuroNexus 16-shank *in vitro* probe

This linear array is a custom design developed by NeuroNexus for the researcher Liset Menendez de la Prida (*'A16x1'* series, NeuroNexus Technologies, Inc., Ann Arbor, Michigan, US). It is designed as a 16-tooth comb with one contact site per shank and 100 or 50 μm shank-to-shank spacing to facilitate *in vitro* recordings [143, 144]. Smaller spacing is more suitable to densely sample single cells, but the bigger version has a longer tissue coverage. Contact sites are circular with a diameter of 15 μm and have impedance magnitudes between 1-1.5 MΩ at 1 kHz. This comb probe was used in the first simultaneous IC-EC recordings in II. Thesis group (4.2), Section 4.2.2. During measurements the probe can be inserted perpendicularly into the CA1 region of the hippocampus to cover all the layers for parallel pyramidal cells. The linearly spaced contact sites are optimal to track the elongated shape of these neurons. However, the main disadvantage of this probe is concerning the so called dead-spot problem, which means that the contacts are not completely located at the end of each probe. This problem still holds for the above mentioned hockey-stick probe, but in that case, surface design introduce a much larger additional distance from any targeted cell. The ineffective design of centred contact sites creates an additional space (in axial direction) towards the tip of the shank (and a smaller lateral space between the edges of the shank and the centred contact sites). These insulating dead-spots will add a 10-50 μm distance plus from the chosen cell to record and they may hinder the capability to capture their single cell activity. But naturally, this dead-spot problem only holds for two dimensions (axial and lateral), with side positioning, high-quality signals can be captured in front of the contact site.

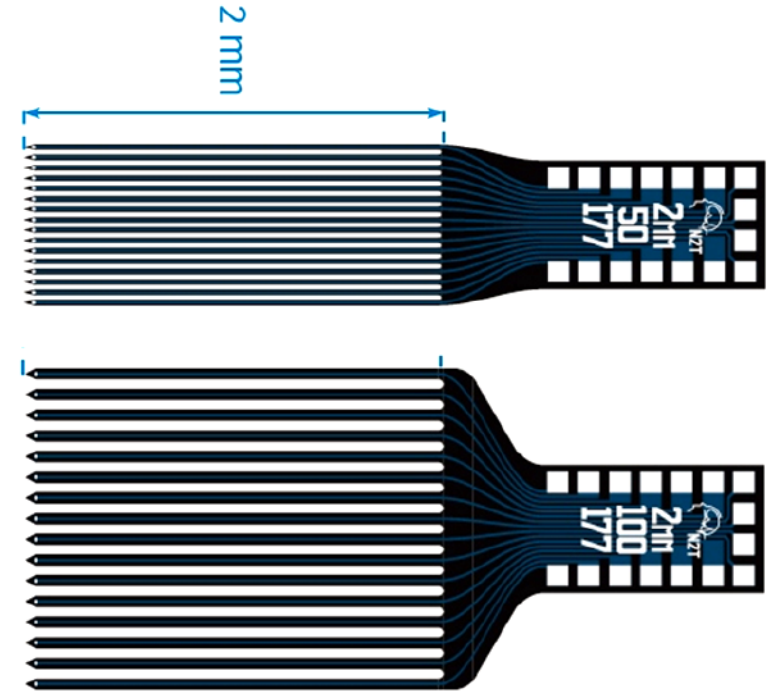

(a) Schematics of shank dimensions

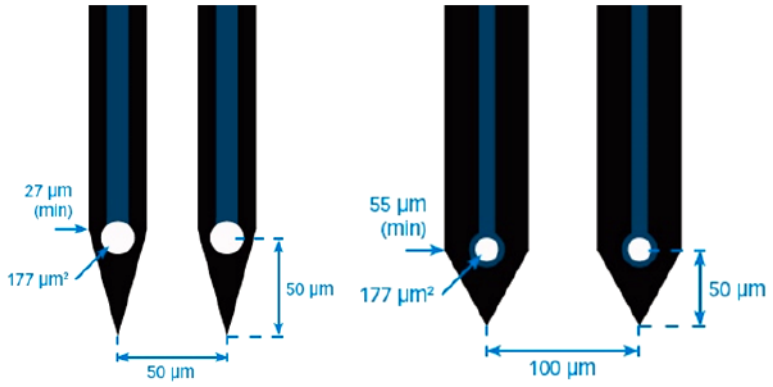

(b) Probe tip dimensions

Figure 3.2: *'The comb'*: Parameters of the NeuroNexus custom-designed, 16-shank probe

3.1.3 *'The spiky'*: Novel, 32-channel spiky probe presented in this thesis

This multielectrode also has a comb-like structure, but unlike the NeuroNexus 16-shank comb probe, the spiky probe consist of one single shank carrying 32 protruding contact sites. The spiky probe was named after its novel contact site arrangement developed by me and colleagues in our lab and fabricated in collaboration with a German partner company (IMTEK GmbH, Freiburg, Germany). The inter-contact distance can be varied between 25 μm, 50 μm and 100 μm.

The main advantage of spiky probe against the hockey-stick surface probe is the arrowhead-like design of the contact sites that facilitates a slight penetration into the tissue providing better cell-accessibility and higher signal quality. This advantage will be analysed in detail in Results section 4.1.4. A further advantage of the spiky probe compared to the NeuroNexus comb probe

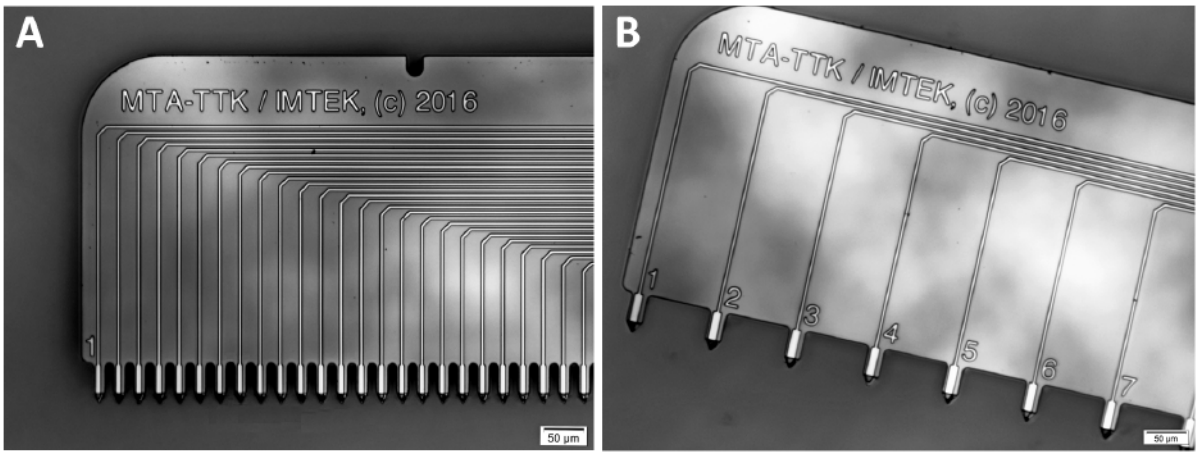

Figure 3.3: *'The spiky'*: Novel, 32-channel spiky probes presented within this thesis. Densest (A) and longest (B) version with inter-contact distance of 25 μm and 100 μm, respectively.

is the single-shank design providing easier positioning and the elimination of dead-spot by the edge-type construction of the triangular contact sites on the tip of each protruding spiky (or arrowhead-like) ending. The following Table 3.1 summarises all types of multi-channel silicon probes used for extracellular recordings and their main recording dimensions.

Probe name	Company	Channel count	Spacing [μm]	Sampling area [μm]
'*Hockey-stick*'	Plexon Instruments (*in vitro* modified U-type)	24	50	1150
'*Comb*'	NeuroNexus (A16x1-2mm-100-177-A16)	16	100	1500
'*Comb*'	NeuroNexus (A16x1-2mm-50-177-A16)	16	50	750
'*Spiky*'	custom-made	32	100	3100
'*Spiky*'	custom-made	32	50	1550
'*Spiky*'	custom-made	32	25	775

Table 3.1: Multi-channel silicon probes used for extracellular recordings and their main recording dimensions: channel counts, spacing (inter-contact distance in [μm]) and sampling area ($(channel\_count - 1) \times spacing$) .

3.2 Whole-cell patch-clamp intracellular recordings

'*Patch-clamp*' is an IC recording technique, which measures ionic currents under a fixed voltage value (voltage-clamp mode) or voltage-deflections under a fixed amount of applied current (current-clamp). The method was invented by Erwin Neher and Bert Sakmann in the early 80s and they received the Nobel Prize in 1991 for their pioneering work, which become then a gold standard and the most widely used method in cellular neurophysiology. Although the

patch-clamp technique was originally developed in order to record single ion channel activity, the '*whole-cell*' configuration has become of equal if not greater importance over time. Classically, electrolyte-filled glass micropipettes (with an $Ag/AgCl$ wire electrode at the backside) are used to seal the tip of the pipette against the cell membrane, establishing a '*cell-attached*' state, and then (by applying gentle suction) break the membrane for obtaining whole-cell patch-clamp configuration. The result is equivalent to impaling a cell with a sharp microelectrode as it has been done earlier for decades, however, the access resistance is much lower and the induced leakage conductance is also lower for patch-clamp. These features allow researchers to gain lower noise and higher-fidelity IC data with the possibility of relatively long-range (up to couple of hours) and customisable recording protocols.
However, it is not easy to establish a good seal, or to maintain this good access on the targeted cell over time. Several obstacles can emerge during patch-clamping e.g. contaminated IC solutions, clogging pipette tip, inappropriate applied currents or compensations, tissue movements or '*closing*' cellular membrane. Besides the fine-tuning of technical details, one must practically have a good sense to achieve successful patching and it becomes even more challenging for *in vivo* studies, which go beyond the focus of this current study. Details about simultaneous IC-EC recordings will be explained in the II. Thesis group (4.2), Section 4.2.1.

3.3 Experimental protocol

Recording protocols for all the three Thesis groups were performed on the same experimental set-up using the similar tool-kit with minor changes. Specific requirements and additional settings will be detailed in corresponding Results sections, here I only focus on basic hardware and software tools essential for general data acquisition.

3.3.1 Brain slice preparation

Acute horizontal hippocampal slices were prepared from adult Wistar rats (between 200-350 g, gender balanced, in total #30 successful experiments at the date of thesis submission). Within the I. Thesis group (in Section 4.1.4), I tested electrophysiological performances by using #7 rats (with #17 insertions) for the spiky probe and #7 rats (with #9 insertions, in total) for the hockey-stick *in vitro* surface probe [145, 146].
Within the II. Thesis group (in Section 4.2.2), only Wistar rats were used and simultaneous IC-EC and EC-only recording sessions were both recorded and intermingled. At the moment of thesis submission, I have #9 successful simultaneous IC-EC recordings with the NeuroNexus comb-probe and #7 with spiky probes. (A detailed, annotated and ever-growing summary table is available containing both recorded datasets and their experimental conditions as a Supplementary Material for the thesis.)
In addition to Wistar rats, Thy1-GCaMP6 transgenic mice were also used for population imaging under 2P microscopy [115]. In the I. Thesis group (in Section 4.1.4), #1 mouse

(between 15-20 g) was used for representative testing of the spike probe in combined EC-2P recordings and #3 more mice were used in the III. Thesis group (in Section 4.3.3) with NeuroNexus comb-probe to collect combined data for eliminating 2P-generated photoelectric artefacts.

Animals were bread and reared in the Research Centre of Natural Sciences, Hungarian Academy of Sciences. Animals were supplied with food and water *ad libidum* and were kept on a 12-12 hour light-dark cycle. All of the protocols followed the guidelines of the Hungarian Act of Animal Care and Experimentation (1998; XXVIII, section 243/1998.). The Animal Care and Experimentation Committee of the Hungarian Academy of Sciences, and the Animal Health and Food Control Station have approved the experimental design (license number: PEI/001/2290-11/2015). Efforts were made to minimize animal suffering and to reduce the number of animals used. Before the experiment, the animals were deeply anaesthetized with isoflurane (min. 0.2 ml/100 g), quickly decapitated and their brains were immediately removed and dipped into cold (2–3 °C), oxygenated (95% O_2, 5% CO_2) cutting solution. The cutting solution contained the following composition (in mM): 250 Sucrose, 26 $NaHCO_3$, 10 D-Glucose, 1 KCl, 1 $CaCl_2$ and 10 $MgCl_2$. 500 μm-thick horizontal slices were cut by a vibratome (VT1200s; Leica, Nussloch, Germany) from both hemispheres containing the whole hippocampal formation. Slices were kept in a standard '*artificial cerebrospinal fluid*' (aCSF) solution at room temperature (20–22 °C) for at least 1 h before use. The recordings were performed with a standard recording aCSF containing (in mM): 124 $NaCl$, 26 $NaHCO_3$, 10 D-Glucose, 4 KCl, 2 $CaCl_2$ and 2 $MgCl_2$.

3.3.2 Measurement set-up and signal acquisition

The whole recording system was build under a two-photon laser scanning microscope set-up developed by the Femtonics company (Femtonics Ltd., Budapest, Hungary) from a transformed Olympus BX61 upright microscope, which has a NIR bright-field camera mode and a 2P fluorescent mode as well. Both the stage and two other lateral micromanipulators were controlled by motorised wheels of the Luigs-Neumann (LN) controller system (Luigs&Neumann Feinmechanik und Elektrotechnik GmbH, Ratingen, Germany).
After placing the brain slice into the perfusion chamber of the microscope, it is fixed by a light and small metal holder ring. In the recording chamber, a dual-perfusion reservoir was used by perfusing both the top and the bottom surfaces of the slices with relatively high perfusion speed ($\geq$10 ml/min) to provide better oxygenation, similar to *in vivo* conditions [17]. The recordings were performed at 32-34 °C. Under these conditions, SWR population activities and SUAs were reliably detected in the hippocampus [146, 147, 148].

The locations of the slice and recording IC and EC probes are shown schematically on Figure 3.4. Please note the parallel orientation between the EC probe and the patch-clamped cell and the almost perpendicular orientation between IC and EC recording electrodes.

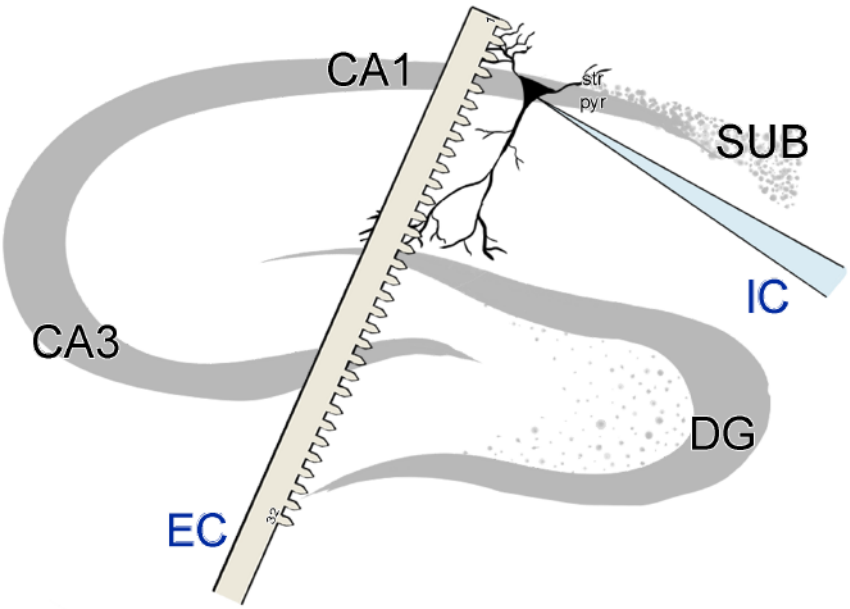

Figure 3.4: Schematics of the recording arrangement. Please note the orientation of the slice and the CA1 pyramidal cell compared to the EC spiky probe.

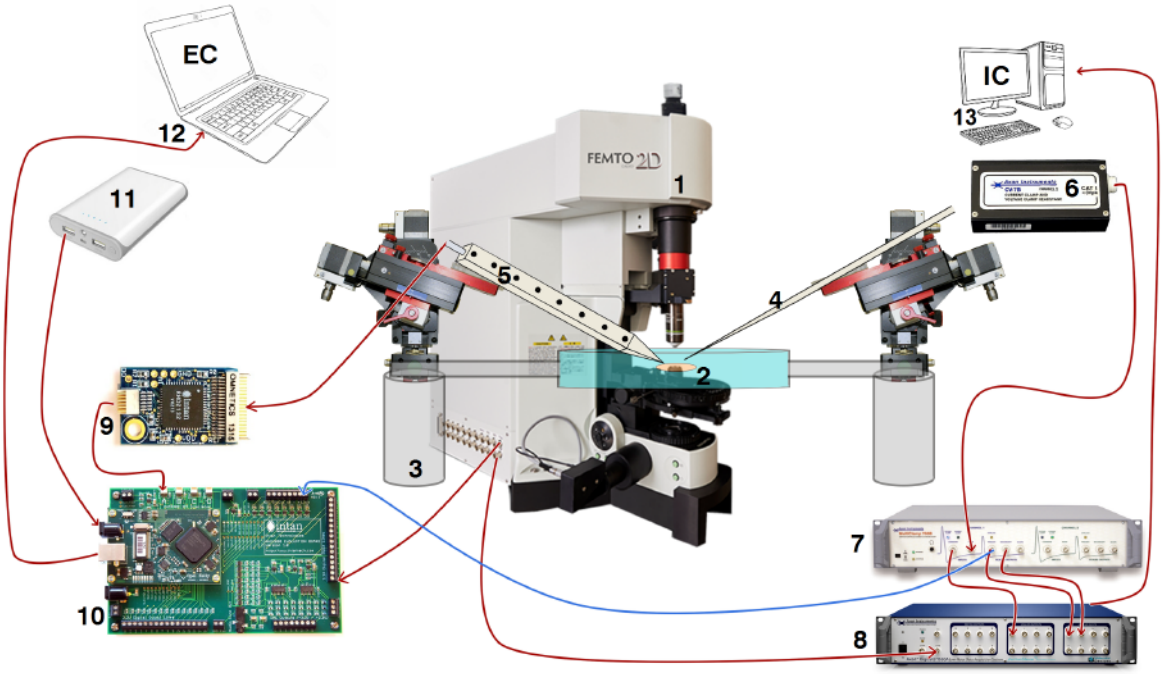

Figure 3.5: Schematic flowchart of the simultaneous IC-EC recording set-up. Numbers represents the following instruments: 2P microscope (1), recording chamber and brain slice (2), LN stage and manipulators (3), patch-clamp (4), EC multi-channel probe (5), Axon pre-amplifier (6), Axon Multiclamp amplifier (7), Digidata A/D converter (8), RHD2132 pre-amplifier chip (9), RHD2000 FPGA-based evaluation board (10), Power bank (11), Laptop (12), Main PC (13). Blue curve shows an occasional possibility for precise synchronisation between IC and EC data streams.

Figure 3.5 depicts figuratively the flow of information during recordings. Electrophysiological signals in the brain slice (2) under the 2P microscope (1) can be picked by both IC (4) and EC (5) recordings. For positioning, LN stage and micromanipulators (3) can be motorically adjusted if needed. From this point, information splits into two independent data streams. IC data acquired by the Axon CV-7B pre-amplifier are transmitted into the Multiclamp 700B amplifier (7) in two channels (first for patch-clamp signal, second for command signal). Before the A/D conversion by Digidata 1550B digitiser (8), analogous patch-signal can be divided and routed also to the INTAN board ADC input channel (curve shown in blue). This can guarantee sub-millisecond precise synchronism (discussed later in Section 3.4.2 and Results section 4.2.1. For the last step, digitised signals are transmitted to the main PC. Unlike the EC recorded signals, which follows a separated route. The printed circuit board (PCB) of the probes is connected to the INTAN2132 pre-amplifier chip (9) via Omnetics connectors. Data is transmitted via flexible INTAN cables directed to Port-A of the FPGA evaluation board (10). This board has a power-bank supply (11) and a separate laptop (12) for acquisition in order to avoid any additional noise contamination of recorded small amplitude EC signals.

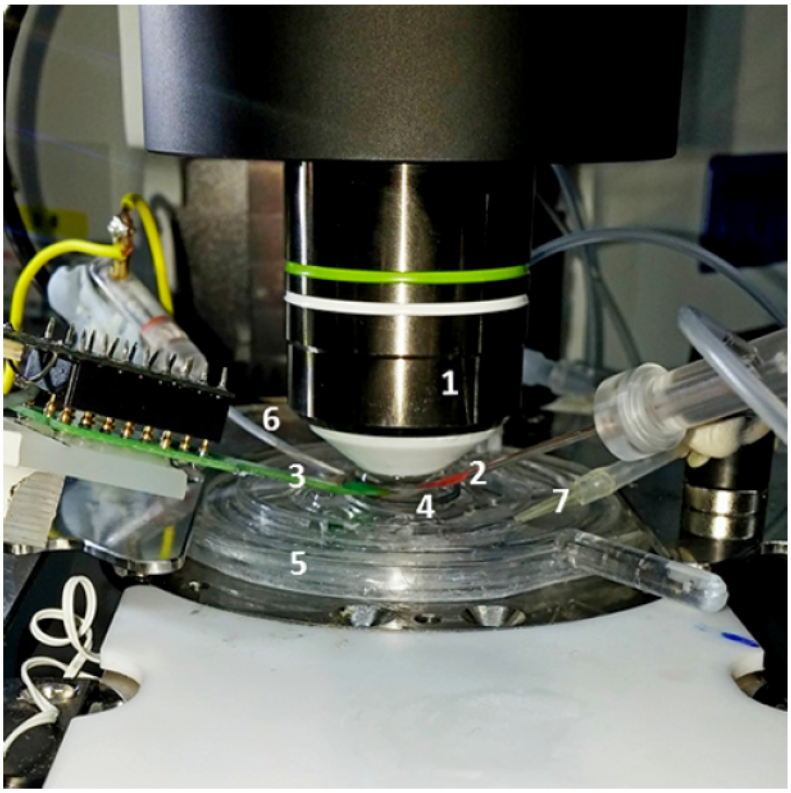

Figure 3.6: Close-up view of the simultaneous IC-EC recording. Numbers represent the following:2P objective (1), patch-clamp (2), EC multi-channel probe (3), brain slice and holder ring (4), dual-perfusion chamber (5), reference electrode pellet (6), outlet of aCSF perfusion (7).

We can have a close-up view of the set-up on Figure 3.6. Labels are the following: Olympus 20x objective of the 2P microscope (1), patch-clamp pipette filled with IC solution (2), EC multi-channel probe (NeuroNexus comb probe shown here) with its connector (3), brain slice

and holder ring (4), dual-perfusion chamber (5), reference electrode pellet (6), outlet of aCSF perfusion (7).

The 2P microscope built by Femtonics Ltd. (Femtonics Ltd., Budapest, Hungary) has a near-infra red (NIR) bright-field camera mode and a two-photon fluorescent working mode as well. The integrated MES software package (Femtonics) was used to control the movement of the objective and display the captured image real-time. This software performs all standard microscopy functions and integrates the control of the hardware units, like the scanner, photomultiplier, light path actuators and other electrical devices. The patch-clamp system (Axon Instruments, USA) consists of several subunits. During the recording, the signal was first transferred to MultiClamp 700B amplifier, that maximizes signal-to-noise ratio and enables whole-cell voltage-clamp and current clamp recordings, then feed to the computer through Digidata 1550B A/D converter. MultiClamp Commander software was used to operate the glass pipette and set various parameters and compensations. pClamp10 software consists of Clampex visualization software, which is suitable for acquiring digitized data, Ramp-test was also performed on this platform, and Clampfit analysis software, which provides a wide variety of tools for statistics, transforms and different layout designs for intracellular data.

Extracellular signals from multi-channel silicon probes were transmitted to the Intan RHD2000 Evaluation system (Intan Technologies, USA), its task is to acquire, pre-amplify and digitize the raw data. It consists of a 32-channel pre-amplifier chip (RHD2132), a RHD2000 FPGA interface board, which is an open-source hardware with up to 128 channels for bio-potential recordings and thin, flexible interface cables for connections. Intan RHD2000 software transfers data to the screen, operates the amplifiers and sampling frequency can be set here. The wideband signals (from 0.1 Hz up to 7 kHz) were recorded with 20 kHz sampling rate.

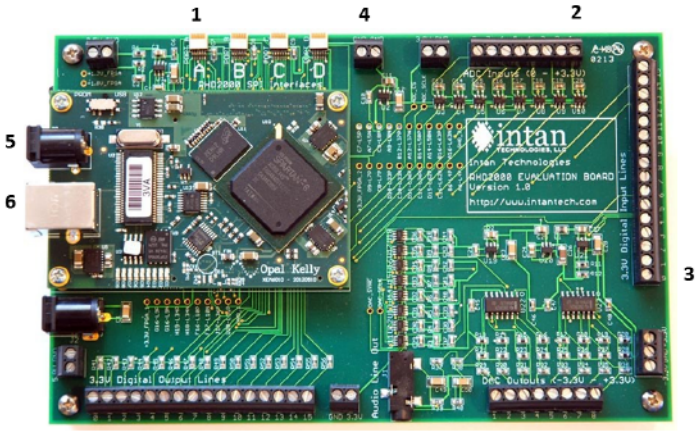

Figure 3.7: Main FPGA board of the INTAN RHD2000 Acquisition System. Highlighted numbers are the following: EC signals (1), Occasional analogous IC signal from patch-clamp (2), Digital trigger signal from the 2P microscope (3), Ground cable (4), Power supply (5) and USB connection (6).

On Figure 3.7 the RHD2000 evaluation board is shown with its input and output connections highlighted with numbers. EC signals, that were recorded by the multi-channel probe, amplified by RHD2132 pre-amplifier chip and transmitted via flexible INTAN cables arrive at port-A (1). Analogous IC signal coming from the Axon Multiclamp amplifier can be connected to the ADC input (2). Digital input trigger signal from the microscope goes to the 3.3 V digital input line (3). Ground cable wired here (4). Battery-powered 5 V power supply is applied here (5). Lastly, USB cable should be connected with this plug (6) to connect the FPGA board and a PC or laptop providing recordable data acquisition.

After every experimental day, the probes were withdrawn and to eliminate tissue residue, cleaned by immersing into 1% Tergazyme solution (Sigma-Aldrich, St. Louis, MO, USA) for at least 30 minutes followed by rinsing with distilled water.

3.4 Data analysis

Different needs in the investigation processes imply different data handling methods and analysis strategies. Here I shortly overview the main software used in data processing and technical steps in structural-anatomical analysis of the tissue after the recording.

3.4.1 Analysis of extracellular signals recorded with silicon probes

Extracellular recordings of the local field potentials (LFP), multiple unit activity (MUA) and single unit activity (SUA) recorded by silicon probes were separately analysed based on the following steps: data containing three-minute-long continuous recordings were saved to internal network storage for further analysis. Files were pre-processed using custom-written MATLAB 2017b programs (The MathWorks, Natick, Massachusetts, USA) and visualized firstly by the NeuroScan 4.5 Software package (Compumedics Neuroscan, Charlotte, North Carolina, USA). To extract the activity of single units from the recorded neural signals, automatic spike sorting was performed using the Kilosort software package [149, 150]. Manual supervision of the single-unit clusters detected by Kilosort was done in Phy, an open-source neurophysiological data analysis package written in Python (source: https://github.com/kwikteam/phy). The selection of well-isolated single units was further aided by using two additional criteria [151]. First, the peak-to-peak amplitude of the mean spike waveform of neurons had to be larger than 50 μV. The peak-to-peak amplitude was defined as the absolute amplitude difference between the negative peak and the largest positive peak of the neuron's mean spike waveform, calculated on the recording channel on which the spike waveform of the particular unit appeared with the largest amplitude. Second, selected single units had to have a clear refractory period, defined by a '*violation rate*' below 2%. The violation rate of a single unit (expressed in percentage) is the proportion of spikes in a particular cluster that are followed within 2 ms by other spikes belonging to the same cluster. Using these two criteria allowed us to exclude the majority of low

quality units as well as to decrease the effect of subjective decisions of the operator during the manual curation of neuron clusters. To differentiate between neurons firing narrow and wide spikes (corresponding to putative interneurons and principal cells, respectively) I computed the trough-to-peak times of the mean spike waveforms [66]. Unsupervised hierarchical clustering (called '*Ward's method with Euclidean distance*') was applied to separate the two types of neurons using the calculated spike duration as input feature [152].

3.4.2 Analysis of simultaneous intra- and extracellular signals

For the comparative analysis of IC-EC signals, saved files, which already contained A/D converted binary, raw data (*.rhd* extension), were converted into appropriate format files. For conversion (to *.cnt* extension) - as described above - I similarly used the MATLAB codes (*rhd2cnt*) written by our lab. Then the NeuroScan 4.5 software package (Compumedics, USA) was used to display and analyse multi-channel data series. A subset of recorded EC files contained the IC signal on their last, additional channel. Briefly, if cable coming from patch-clamp pre-amplifier was divided and connected to the ADC input of the INTAN board, then perfect synchronism could be achieved, and 1 additional channel was added to the EC data containing the patch-clamp IC signal. However, this interconnection often resulted cross-talk artefacts between EC and IC signals, when both recorded by the INTAN chip. (For further explanation of simultaneous data acquisition, please see Figure 3.5 in the previous Section 3.3.2 section and Results 4.2.1 section.) For earlier recordings, IC data (*.abf* format) was only recorded separately by the Multiclamp amplifier and Digidata digitizer, thus there was no additional channel on the EC signal (and consequently, no cross-talk artefact), but this separated IC signal had a small but significant (few tens of ms) time difference compared to EC signals. Luckily, this problem was manageable since I always applied a sufficiently long time window ($\pm$ 100 ms) for comparing EC channels to the IC ground-truth. (This larger time window also allowed to investigate the relationship between the spiking cell and its local environment represented by population signals such as SWR activities [148].)

As the first processing step of the raw EC signal,band-pass filter (500 - 5000 Hz, zero-phase shift) was applied to visualise SUA and MUAs. However, in some cases I continued the data analysis on the unfiltered, broadband signal to reveal the relationship between single cell and summed synaptic or population activities in the LFP band. Detection of IC spikes was calculated on the patch-clamp channel, which can be done by thresholding *in-situ* in NeuroScan using the additional, INTAN-recorded analogous channel (if available) or in MATLAB using the *.abf* file recorded by the patch-clamp acquisition systems. For IC recordings, data are considered as noiseless and spiking events are easy to detect with the highest fidelity. Unlike spike detection for EC signals in general, it is not necessary here to define the threshold level as the average (AVG) plus 3 to 5 times the standard deviation (STD), but can be applied as an appropriate voltage value to cross (here, 0 mV upward threshold crossing was applied). Event

file (*.ev2* extension) was then generated from detected IC spike times (in ms). Subsequently, 100 ms long, symmetric time windows (epochs) were cut on all EC channels around each event, 50 ms before and 50 ms after the time point of each IC spike. The number of EC epochs were equal to the number of IC spikes in one simultaneous recording session. Lastly, epochs were averaged over all EC channels resulting in the so-called '*spike triggered average*' (STA), in which we could observe the '*footprint*' generated by my patch-clamped cell in the extracellular space sampled by multiple, closely located EC contact sites.

Intracellular data processing (regarding the sweeps of Ramp-test and spontaneous gap-free recording) was performed in Clampfit software. When analysing the Ramp test, the program displays the holding current steps and the voltage response given to the current injection and the sweeps can be displayed either individually or by projecting them on each other. In addition, cursors placed on the visual interface of the program can be dragged along the time axis, and the voltage and time values appear at each data point immediately. The examination of amplitude and spike number responses given to changing holding current were performed using the statistics program tool of the Clampfit software, where the baseline, search region and parameters were set. Waveform parameters were evaluated based on spontaneous recordings. Likewise, the trial averages and analysis were performed using the statistics tool of the software.

3.4.3 Fluorescent signals recorded by two-photon imaging

During a whole-cell patch-clamp measurement, soma, apical and basal dendrites of the patched cell became visible by the diffusion of fluorescent dyes from the tip of the micropipette. In the 2P working mode of the microscope Alexa594 dye lights in red, Fluo-4 flashes in green colour, and the probeorientation could also be observed based on its black silhouette. While Alexa594 is a static dye, Fluo-4 changes dynamically following the IC Ca^{2+} concentration changes and thus enables functional mapping [153, 154]. The filling of the neuron with tracer dye also allows *post-hoc* reconstruction techniques, as 2P z-stack projection and Neurolucida histological reconstruction, to more precisely visualise the cell morphology. While 2P z-stack projection can be made *in situ* right after electrophysiological recordings, Neurolucida reconstruction requires a long histological process for the precipitation of biocytin or neurobiotin tracer molecules (but at the same time, this methods provides much better resolution and penetration). Stained sub-cellular compartments are located in different depth in the sample volume. During 2P z-stack projection the images are generated by gradually changing the focal plane in the 'z' axis, the optimal focal difference can be calculated in the image acquisition software. By linking and projecting the pictures one after the other, this technique effectively displays the 3-D microscopy data in 2-D, in this case the cell body and dendritic branching can be visualized, and the out-of-focus signal will be effectively excluded.

3.5 *Post-hoc* histological reconstruction of neuron morphologies

After recording, slices were carefully and quickly removed from the recording chamber, and fixed overnight in 4% paraformaldehyde with 15% picric acid in 0.1 M phosphate buffer (PB, pH 7.4) at 4°C. Then slices were resectioned (Leica 1200S, Wetzlar, Germany) at 60 μm and freeze-thawed above liquid N_2 in 0.1 M PB containing 30% sucrose. I followed a traditional histological analysis published, similar to many published studies in our lab, e.g. in Kerekes et. al (2014) [146]. In this protocol, endogenous peroxidase activity was blocked by 1% H_2O_2 in Tris-buffered saline for 10 min. Cells containing biocytin (or neurobiotin) were revealed with the avidin-biotinylated horse-radish complex reaction (Vector, 1.5 h, 1:250) using *3,3'-diaminobenzidine-tetrahydrochloride* (Sigma, St. Louis,Missouri, 0.05 M in Tris-buffer, pH 7.6) as chromogen. At the end, sections were osmicated (20 min, 0.5% OsO_4), dehydrated in ethanol, and mounted in Durcupan (ACM, Fluka, Buchs, Switzerland). In every case where the histological steps (fixation, re-slicing, and the precipitation of biocytin) have been successfully completed and neuronal processes of the filled cell became visible and traceable, neurons were selected for digital 3-D reconstruction by the Neurolucida system (MBF Bioscience, Williston, VT, USA).

DOI:10.15774/PPKE.ITK.2020.005

Chapter 4

Results

4.1 I. Thesis group: Development and testing of a novel, multi-channel spiky probe for extracellular recordings

The I. Thesis group will focus on only EC recordings within an *in vitro* slice environment. A novel spiky probe will be demonstrated in this study allowing access to deeper cells, and enabling high spatial sampling of their EAPs. Thanks to its arrowhead-like, protruding contact sites, the probe can slightly penetrate into the slice, passing through the surface dead-cell layer. Due to this arrangement, I will report that these probes are able to provide higher single unit yields as well as spikes with higher amplitudes compared to another, commercially available *in vitro* laminar surface design (earlier called as hockey-stick probe introduced in Methods section 3.1.1) [146]. In the following sections, manufacturing processes and packaging methods will be described. Next I show the results of impedance measurements. In addition, the recording performance of the probes will be demonstrated using *in vitro* hippocampal slices. With a quantitative comparison, I will present the improvements of the spiky probe over hockey-stick surface probe. A preliminary result of how the spiky probe can be combined with two-photon imaging will be also presented. Finally I report how the spiky probe is able to capture and oversample the SUAs on multiple contact sites and how recorded EAPs can be analysed to identify putative neuronal cell types based on EC recordings.

4.1.1 Surface materials, fabrication process and packaging

The fabrication process was carried out at IMTEK (IMTEK GmbH, Freiburg, Germany) with the help of Patrick Ruther and Tobias Holzhammer. Fabrication of the Si-based spiky probes is schematically summarized in Figure 4.1. The fabrication process applies 4-inch, single-side polished Si wafers, insulated using a 1-μm-thick, stress-compensated multi-layer stack of silicon oxide (SiO_x) and silicon nitride (Si_xN_y) deposited using plasma enhanced chemical vapour deposition (PECVD) (A). The interconnect and contact pad metallization (line and space of 1.5 and 1.5 μm, respectively) was realised using lift-off patterning of an evaporated layer stack of titanium (Ti, 30 nm), gold (Au, 250 nm) and Ti (30 nm) (B). The Ti layers serve as adhesion

DOI:10.15774/PPKE.ITK.2020.005

promoters between the insulation and the subsequently deposited passivation layers, and the *Au* film. We used the image reversal photoresist AZ 5214E (Merck KGaA, Darmstadt, Germany). Following the lift-off process, the metallization is passivated using another stress-compensated 1.5-μm-thick PECVD SiO_x-Si_xN_y layer stack (C). This is followed by opening the passivation layer to access the probe metallization at the position of the contact sites and contact pads using photolithography (AZ4533, 3.3 m, Merck KGaA) and reactive ion etching (RIE) (D).

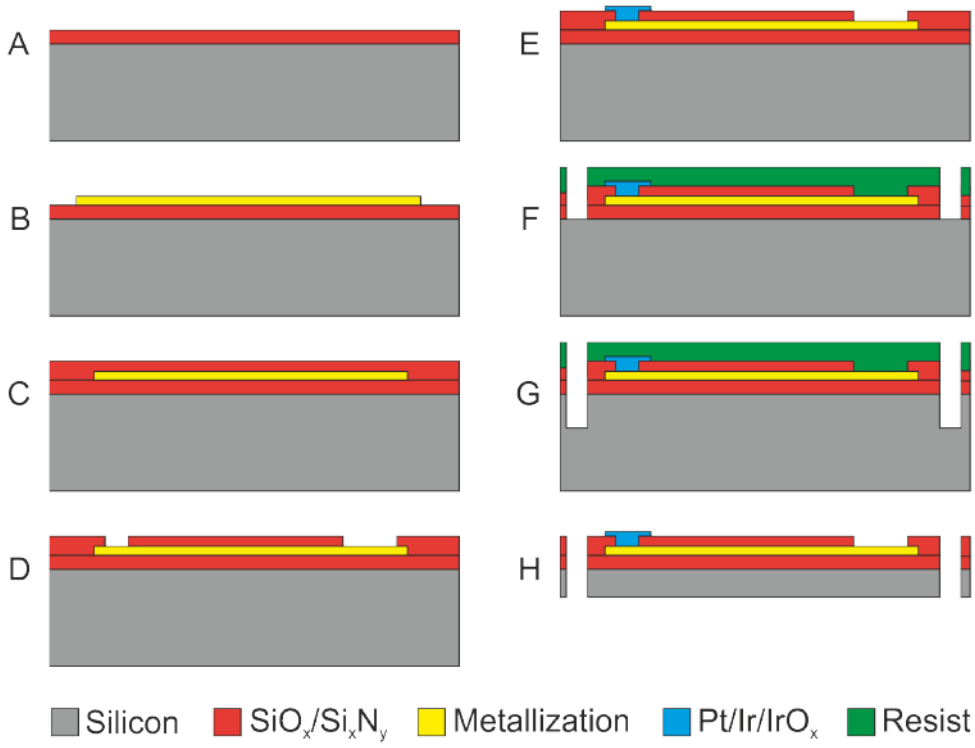

Figure 4.1: Fabrication of *Si*-based spiky probes. (A) PECVD insulation layer, (B) sputter deposition of *Ti* / *Au* / *Ti* and patterning by lift-off using image reversal resist (C & D) deposition and RIE patterning of PECVD passivation layer, (E) deposition and lift-off patterning of *Pt* / *Ir* / IrO_x metallization of contact sites using dual layer lift-off resist, (F) RIE patterning of dielectric layers, (G) DRIE of bulk silicon, and (H) rear side grinding of *Si* to intended probe thickness of 50 μm.

Subsequently, the contact site metallization is deposited using a dual-layer lift-off resist (LOR5A, MicroChem Corp., Westborough, MA, USA and AZ1518, 1.8 μm, Merck KGaA) and sputter deposition of *Ti* (30 nm), platinum (*Pt*, 150 nm), iridium (*Ir*, 100 nm) and iridium oxide (IrO_x, 200 nm, reactively sputtered in an oxygen plasma) (E) [155]. Next, the dielectric layers, i.e. SiO_x-Si_xN_y insulation and passivation layers, are patterned using photolithography (AZ9260, 10 μm, Merck KGaA) and RIE (F). Then, the bulk silicon is etched (using the etching before grinding (EBG) technology [156] to a depth that exceed the intended probe thickness by roughly 30 μm using deep reactive ion etching (DRIE) in an inductively coupled plasma (ICP Multiplex from STS, Newport, U.K.) etching process which applies the Bosch process (G) [157]. Finally, the *Si* wafer is thinned from the rear side using grinding and polishing as offered by DISCO Hi-TEC Europe GmbH, Kirchheim, Germany (H). Probes are then manually picked

DOI:10.15774/PPKE.ITK.2020.005

from the grinding tape using tweezers, glued onto a custom designed printed circuit board (PCB) and wire bonded. The bond wires are finally encapsulated in a glop-top (EPO-TEK 353ND-T, Polytech PT GmbH, Germany) for electrical insulation.

4.1.2 Structural design and probe layout

The silicon shank carries 32 contact sites in a horizontal, laminar arrangement. The contact sites are located at the bottom edge of the shank. Furthermore, they are semi-circularly released from the bulk to form arrowhead-like or spiky shapes (See Figure 4.2/B for schematics and Figure 4.3/B-D for SEM pictures).

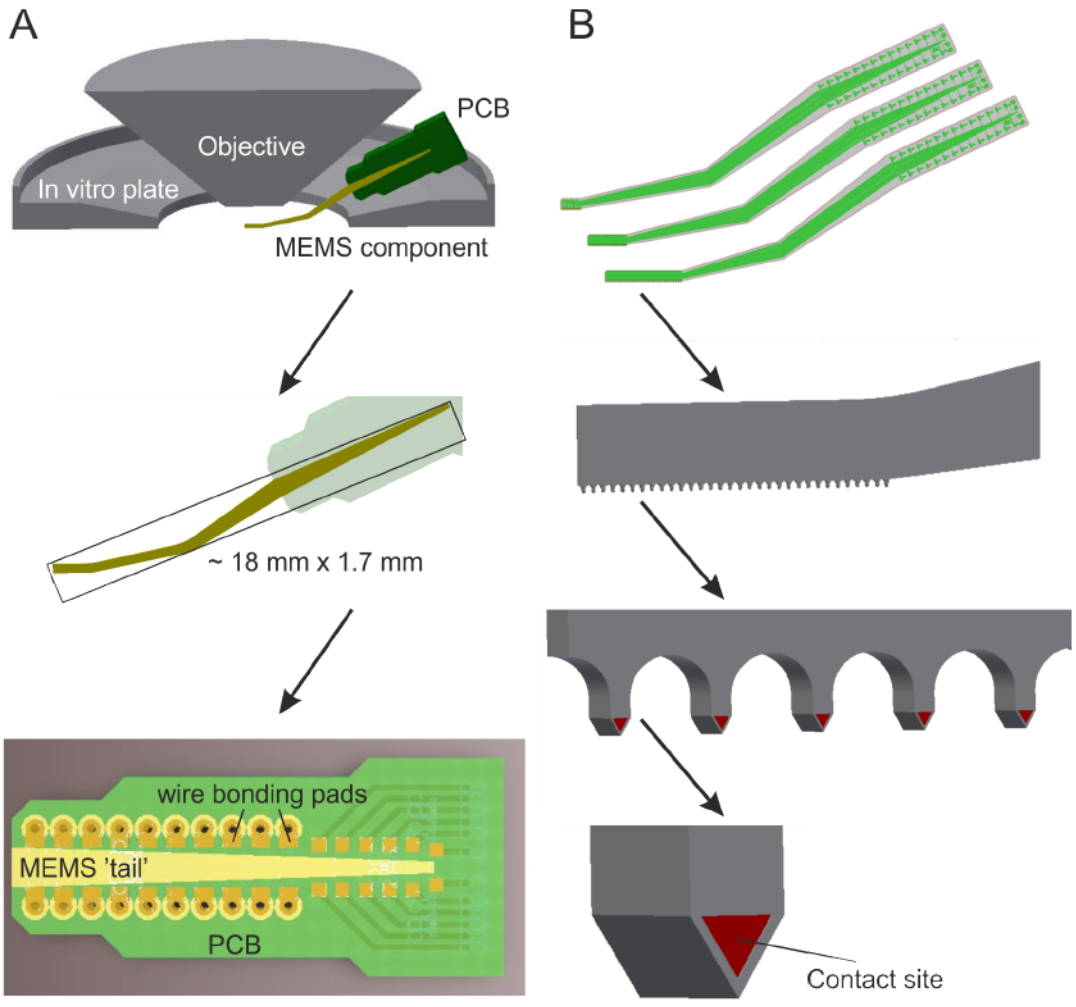

Figure 4.2: Schematics of the experimental design, as well as packaging and bonding of spiky probe layouts. Positioning of the angled shank between in vitro plate and microscope objective (A). Three different versions of the device which differ from each other only in the inter-contact distance (B).

Because of these spiky contact sites, the probe has the ability to penetrate into the brain slice, diving beneath the surface dead-cell layer. Moreover, its tips can even approach individually targeted cells if a precise image-guidance is applied during insertion (for details,

DOI:10.15774/PPKE.ITK.2020.005

please later see Figure 4.7/A-B in Section 4.1.4). The angled probe allows us to obtain combined optical information and simultaneously monitor the measured region with a 2P laser scanning microscope system (Femtonics Ltd., Budapest, Hungary), which has a NIR bright-field camera mode and a two-photon fluorescent mode as well.

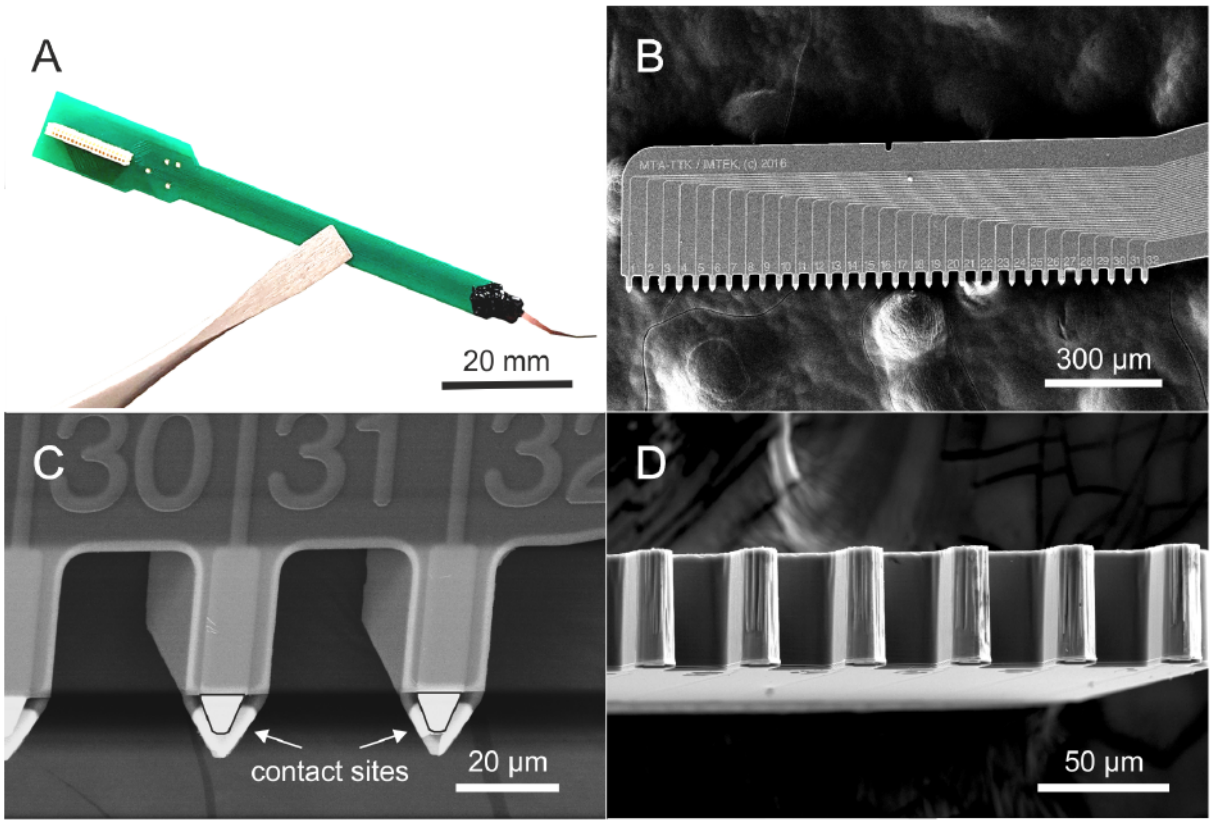

Figure 4.3: Optical photograph and scanning electron microscopy (SEM) images of the spiky probe. Picture of a fully assembled device showing the main probe components from right to left: a single silicon shank (grey and red), glop top protecting the bond wire (black), the printed circuit board (PCB, green) and the Omnetics (white) connector (A). SEM picture of the medium-sized spiky probe version (with inter-contact distance of 50 μm) and related wiring. C-D: SEM close-up views at two different orientations. Please note the arrowhead-shape, protruding contact sites.

Three different versions of the spiky probes were created, which only differ from each other in the spacing of the 32 contact sites. The inter-contact distances (center-to-center) of 25 μm, 50 μm and 100 μm were realized resulting in total spans of 775 μm, 1550 μm and 3100 μm, respectively (see Figure 4.2/B, top as well as Table 3.1 in Methods section 3.1.3). The shortest type is most suitable for high-density recordings, while the longer types can cover more cortical layers and thus have a wider sampling area. The microfabricated part is glued onto and wire-bonded to a rigid printed circuit board (PCB) specifically designed for this purpose. It provides interconnection to the external instrumentation.

DOI:10.15774/PPKE.ITK.2020.005

Detailed tests for the performance and stability of contact sites (presented in the following sections) were obtained by using the high-density version (25 μm inter-contact distances). The dataset of spatially oversampled single units were collected with the same spiky probe version. The other two versions (namely the spiky probes with 50 μm and 100 μm inter-contact distances) were both totally functioning and were tested at least once. I included their impedance results but such detailed *in vitro* recordings presented for the high-density probe are still to be investigated, which go beyond the scope of the current thesis work.

4.1.3 Results of impedance measurements

Before *in vitro* experiments, electrochemical impedance spectroscopy was tested on each probe for diagnostic purposes. A built-in impedance checking protocol was used implemented by the INTAN RHD2000 acquisition system (InTan Technologies, Los Angeles, CA, USA). The impedance magnitudes and phase angles of all contact sites on each probe were measured, at various frequencies ranging from 20 Hz up to 5 kHz. The impedance measurement was carried out in physiological saline solution against an $Ag/AgCl$ reference electrode. It is well known that the impedance of a contact site is inversely proportional to its area [12, 19]. Please note that the spiky probes and hockey-stick probes have different contact sites, and consequently, different recording areas as well. While the contact site of the spiky probe has an equilateral triangle-shape (with a base of $a = 8$ μm and an altitude of $m_a = 8$ μm), the hockey-stick probe has circular contact sites with diameter of $d = 15$ μm. In the case of the high-density spiky probe (with inter-contact distance of 25 μm), the electrode area (triangular) is 32 μm^2, for the medium version (with inter-contact distance of 50 μm) is again 32 μm^2, and for the biggest version (with inter-contact distance of 100 μm) is 50 μm^2. For the hockey-stick probe the diameter of contact sites (circular) is 15 μm resulting an area of 176.7 μm^2. Contact site area can be calculated as follows:

$$T_{triangular} = \frac{a \cdot m_a}{2} = \frac{8 \cdot 8}{2} = 32 \mu m^2, \tag{4.1}$$

$$T_{circular} = \frac{d^2 \cdot \pi}{4} = \frac{15^2 \cdot \pi}{4} = 176.7 \mu m^2 \tag{4.2}$$

Despite the notable difference between contact site areas, contact site diameters are not significantly differ from each other according to the literature [4, 19]. Averaging effect of spatio-temporal signals becomes problematic only if larger diameters ($d \geq$50 μm) are applied. Another simulation study suggests that contact site diameters smaller than 20 μm result in realistic amplitudes compared to simulated point sources (highlighted by blue circles in Figure 4.4). The averaging effect becomes step-by-step more severe when larger diameters are applied, in accordance with previous experimental findings [158]. Based on these literature results, I hypothesise that my chosen probes may behave similarly for signal filtering and thus they are comparable from the point of view of recording performance.

DOI:10.15774/PPKE.ITK.2020.005

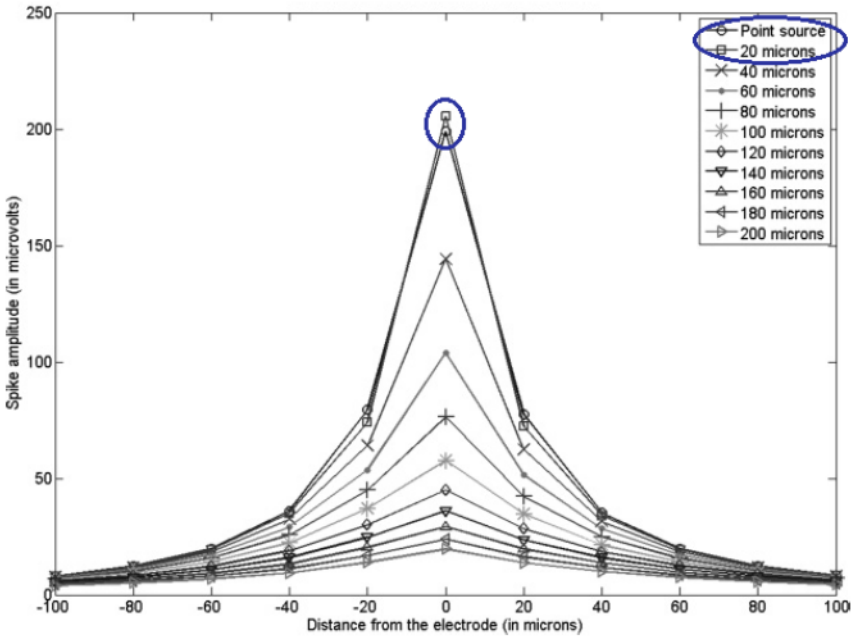

Figure 4.4: Simulation for different contact site diameters and their averaging effect on recorded signal amplitudes [158].

Figure 4.5/A & B show the impedance spectroscopy of the high-density spiky probe (with inter-contact distance of 25 μm), alias the mean impedance magnitudes with corresponding standard deviation, at varying frequency levels (before the first in vitro experiment). Please note that the impedance magnitudes were monotonically decreasing from 20 Hz up to 5 kHz with a small standard deviation between contact sites. I highlight the particular frequency of 1 kHz, where this high-density spiky probe showed average impedance magnitude of 1.27 $\pm$ 0.1 MΩ across all contact sites with an average phase angle of -70 $\pm$ 5°. The phase angles varied much less up to 2 kHz ranges for a given contact site, and they also varied minimally between sites (Figure 4.5/B). Furthermore, two faulty contact sites (6.25% out of 32 contact sites) with impedance magnitudes higher than 3 MΩ at 1 kHz were found on this particular probe, they considered as open circuits and thus were excluded from further analysis.

I have tested the two longer spiky probe versions as well, even if I did not perform more recordings using them in this study. I shortly report the impedance results at 1 kHz, where the average impedance magnitudes on the medium spiky probe (with inter-contact distance of 50 μm) were comparable with the high-density version (since they have equal sized electrode areas), namely 1.27 $\pm$ 0.3 MΩ, with averaged phase angle of -60 $\pm$ 4°, and two faulty contact sites were found (open circuits, 6.25% out of 32 contact sites). Lastly, for the longest probe (with inter-contact distance of 100 μm) the average impedance magnitude was 600 $\pm$ 20 kΩ, with average phase angle of -56 $\pm$ 5°, which were similar to the surface-type hockey-stick probe (magnitudes of 616 $\pm$ 160 kΩ and phase angles of -56 $\pm$ 7°). On the longest spiky probe I found only one faulty site (short cut, 3.125% out of 32 contact sites). The ratio of faulty contact sites remained well below 10% for all three spiky probes. Let us suppose that these faulty

DOI:10.15774/PPKE.ITK.2020.005

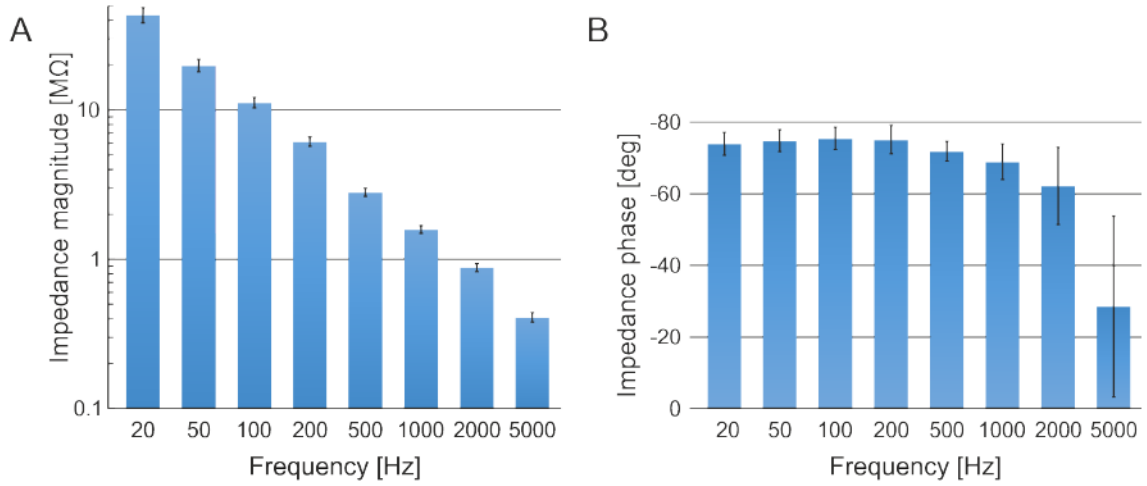

Figure 4.5: Results for impedance spectroscopy. Mean impedance magnitudes (A) and phase angles (B) with corresponding standard deviations at different frequencies ranging from 20 Hz to 5 kHz. Please note the monotonically decreasing magnitudes and phase angle values and the small standard deviations across channels.

contact sites appeared due to the soldering of Omnetics connectors to the PCB, which can be further improved in future work. Nonetheless, the exclusion of faulty sites did not significantly compromise the quality of recordings because of the dense spatial sampling capability. I also

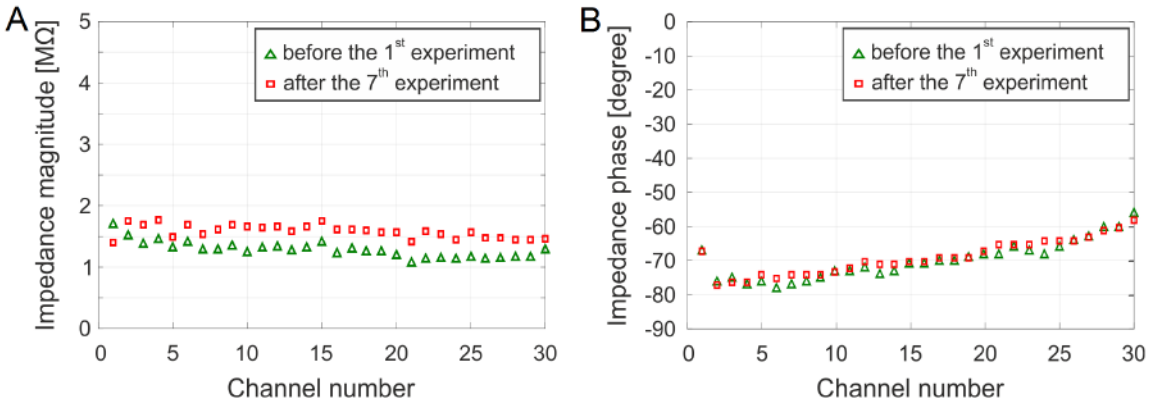

Figure 4.6: Stability and re-usability of spiky contact sites. Impedance magnitudes (A) of all contact sites (at 1 kHz) before the first experiment (green) and after seven experiments (17 insertions), in total (red). Phase angles (B) of all contact sites (at 1 kHz) remained practically identical after the extensive usage.

wanted to test the robustness and re-usability of spiky contact sites. Impedance changes of the high-density spiky probe (with the inter-contact distance of 25 μm) were investigated after an extensive usage (7 experiments with 17 separate insertions, in total) by repeating the impedance test after the last experiment. At this time, I compared the magnitudes and phases only at 1 kHz, since this frequency is widely used as a standard. Other experimental conditions remained unchanged. On Figure 4.6/A & B I show the impedance magnitude and phase changes measured at 1 kHz before and after the extensive usage. The average

DOI:10.15774/PPKE.ITK.2020.005

impedance magnitude of all contact sites was 1.27 ± 0.1 MΩ before the first experiment and was slightly increased after the last experiment to 1.5 ± 0.1 MΩ. However, such minor changes are still acceptable in the literature (e.g. NeuroNexus probes have impedance magnitude values typically between 1-2 MΩ when comparable electrode sizes are used [78]). The impedance phase angles did not change significantly across this time period, starting with an initial average phase angle of -70 ± 5° which remained at around -69 ± 5° after extensive testing. However, this feasibility-test for the robustness of this particular spiky probe does not guarantee universal re-usability. I have to admit that many other factors (such as air humidity or different storage types) can further influence long-term impedance changes and these additional parameters were not investigated in my test.

4.1.4 *In vitro* recording characteristics: a systematic comparison against a commercially available surface design

To validate the electrophysiological performance of the spiky probes, I have performed EC recordings in the hippocampus and neocortex regions of horizontal brain slices from Wistar rats. I show a typical experimental arrangement on Figure 4.7/A. Thanks to the optimal shank curvature and carefully chosen penetration angles, the probe easily fits into the narrow gap between the perfusion chamber and the water-immersion objective of the 2P laser scanning microscopy system (Figure 4.7/A & B). By using the NIR camera-mode of the microscope, precise image-guided positioning of the probe is achievable.

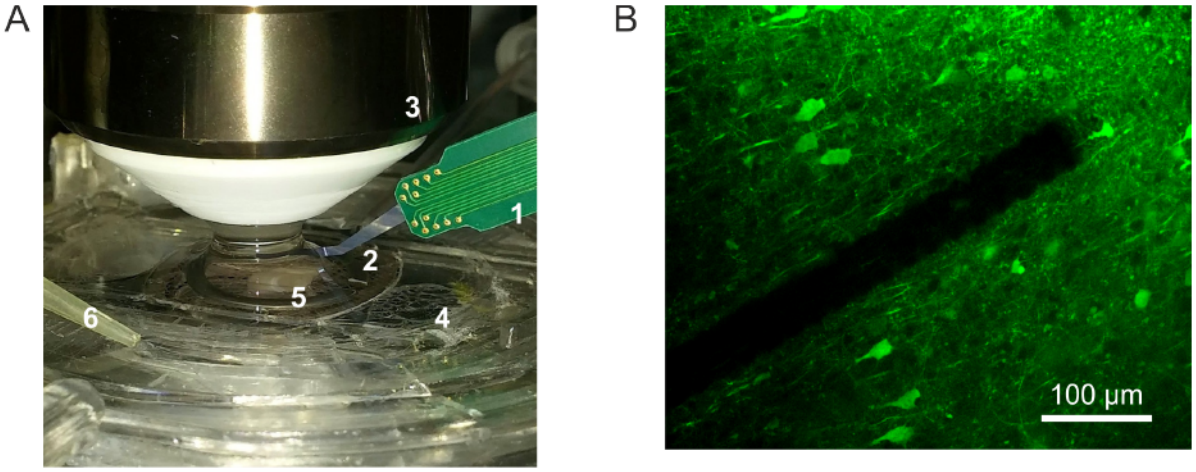

Figure 4.7: Insertion of the spiky probe. A: Photograph of the experimental set-up. Numbers represent the following parts: PCB (1), silicon shank (2), water immersion objective (3), dual-perfusion chamber (4), hippocampal slice and the holder grid (5), outlet of the aCSF (6). (Please see Figure 3.6 in Methods section 3.3.2 for details.) B: Example for visualizing of the high-density spiky probe (with 25 μm inter-contact distance) in 2P imaging (Thy1-GCaMP transgenic mouse neocortex).

DOI:10.15774/PPKE.ITK.2020.005

While inserting the spiky probe, it is important to check whether the protruding contact sites are horizontally placed before approaching the surface of the brain slice. The optimal insertion angle is 22° respect to the main axis of the main shank. Tilting can be easily checked before penetration under the water immersed objective by focusing onto the protruding contact sites. If the horizontal arrangement is achieved, the probe can be lowered and its spiky contact sites can be inserted into the brain slice without any further risk for fracture. If the horizontal arrangement is not achieved, the tilted probe should be retracted and repositioned. As with any type of inserted device, it is not recommended to move in x-y direction once the probe was inserted into the slice. I have not experienced any fracture on the spiky probe while used as described above. I approached cells located in CA1 and subiculum regions of the hippocampus, as well as layer 2/3 cells in the neocortex. These deeper cells are located 50-80 μm beneath the brain slice surface, where – according to the literature – they mainly preserved physiological conditions [17, 18].

As with any *in vitro* recordings, neuronal activities depends on numerous factors, namely oxygenation, perfusion rate of the aCSF, chamber temperature, brain slice quality, or the number of nearby active neurons, which highly depends on the location [17]. In my experience, every single insertion yielded SUAs and MUAs at higher frequencies (between 0.5 kHz – 5 kHz) as well as low-frequency LFP phenomena (from 0.5 Hz up to 100 Hz) with a sufficiently small amount of background noise. Figure 4.7 and 4.8 shows the two typical working modes of the microscope system, the fluorescent 2P imaging mode (Figure 4.7/B), and the basic camera mode (Figure 4.8/B). While the protruding contact sites are clearly visible in the camera mode, they are much less distinguishable from the dark silhouette of the main shank in the 2P mode. It should be noted that photographs and EC recordings were not taken from the same insertion. Figure 4.8/B shows examples of hippocampal SWR activity (gray rectangles) recorded by twelve adjacent contact sites of the spiky probe. Here, the wideband signal was band-pass filtered for extracting the low frequencies (between 0.5 Hz – 40 Hz). On Figure 4.8/C, representative 5-second-long unit activity acquired by fifteen adjacent contact sites. To enhance the visibility of spikes, the recorded wideband data was band-pass filtered focusing on the higher frequencies (between 0.5 kHz – 5 kHz).

After validating the capability of signal acquisition, quantitative comparison was made against the hockey-stick probe (which is basically a similar *in vitro*, laminar, but a surface-type probe, introduced earlier in Methods section 3.1.1) to prove the expected advantages of the penetrating contact sites over a surface design. Neural yields (SUA counts per recording), average and maximal spike amplitudes, as well as noise levels were compared for both types of probes. Firstly, I investigated differences in the noise levels by estimating the root mean square (RMS) noise level in aCSF. In case of the spiky probe, the RMS noise was 9.71 $\pm$ 2.12 μV_{rms} (0.1 – 7500 Hz; average $\pm$ standard deviation) measured on 32 contact sites of the high-density probe (with 25 μm inter-contact distance). While for the surface probe an average of 6.88 $\pm$ 0.58 μV_{rms} was measured (0.1 – 7500 Hz) on 24 contact sites (with 50 μm inter-contact distance).

DOI:10.15774/PPKE.ITK.2020.005

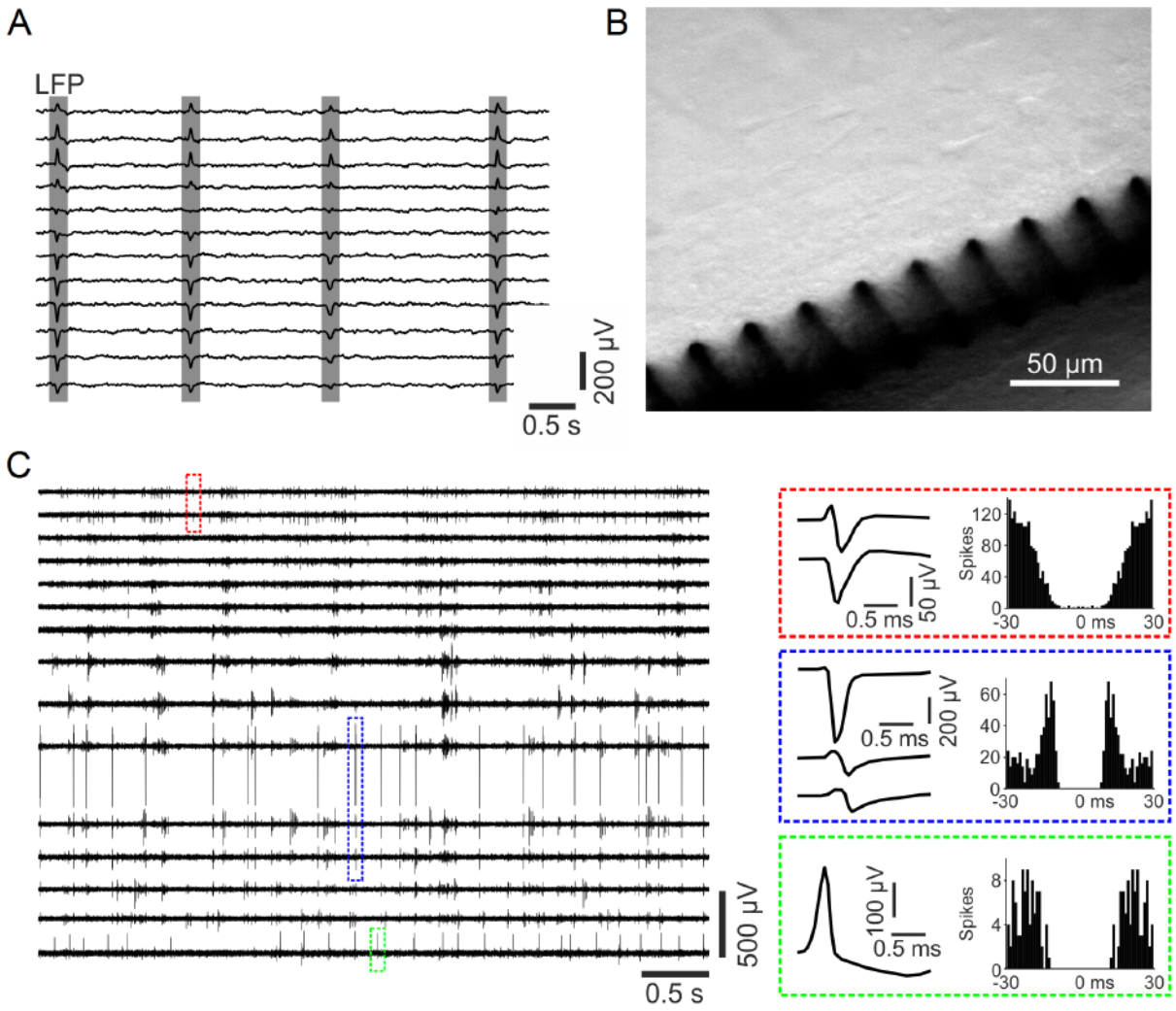

Figure 4.8: In vitro recording characteristics of the spiky probe. Hippocampal LFP with prominent SWR activity (gray rectangles) shown on twelve channels from Wistar rat CA1 region (A). The wideband signal was filtered (0.5 – 40 Hz bandpass) to extract the local field potential (LFP). Example for visualizing the spiky probe in bright-field camera mode in the neocortex (B). Photos and EC recordings were taken from different recording sessions. Representative 5-second-long SUA recording acquired by fifteen adjacent contact sites of the probe (C). To enhance the visibility of spikes, the recorded wideband data was bandpass filtered between 500 and 5000 Hz. Colored dashed rectangles located on the traces mark a single spike of three sample single units. Mean spike waveforms and autocorrelograms (bin size, 1 ms) corresponding to these SUAs are shown on the right.

The input-referred noise of the amplifier was 2.4 μV_{rms}. In the spike band (500 – 5000 Hz), there was only a small difference in the RMS noise level between the two probes, namely 4.63 $\pm$ 0.51 μV_{rms} for the spiky probe versus 3.93 $\pm$ 0.42 μV_{rms} for the hockey-stick probe. Placing the probes on a brain slice elevated the measured noise level by 10 - 20%.

Figure 4.9 shows the distribution of the number of well-separated SUA clusters (Figure 4.9/A) and the distribution of the peak-to-peak amplitude of these waveforms (Figure 4.9/B) for both probes. The total number of well-separated neurons was 32 for the hockey-stick

DOI:10.15774/PPKE.ITK.2020.005

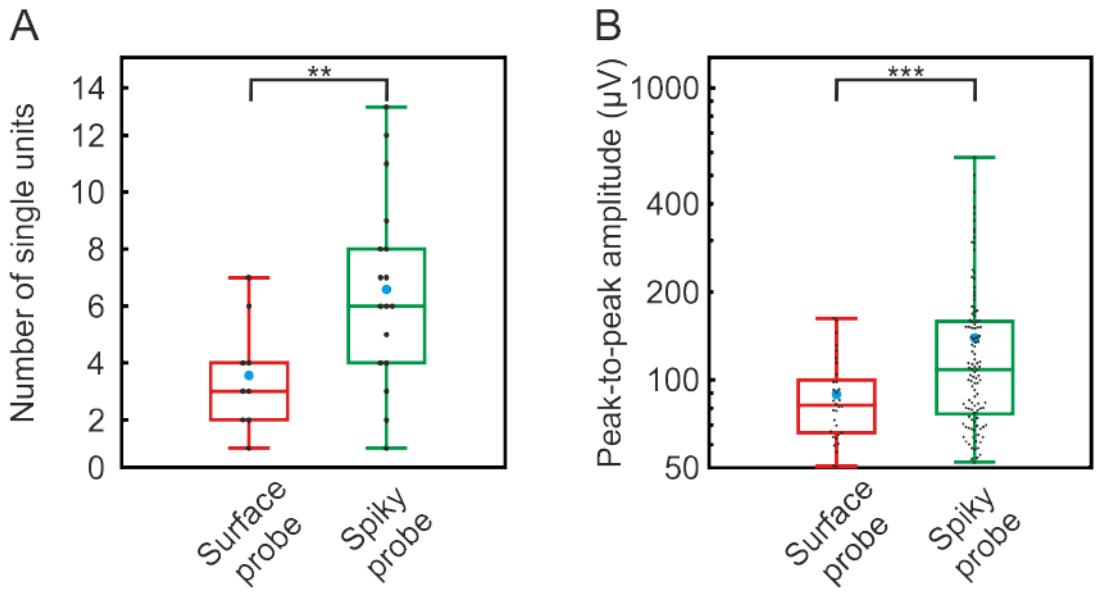

Figure 4.9: Quantitative comparison of recording performances. Box plots showing the distribution of the number of well-separated SUA clusters (A) and the distribution of the peak-to-peak amplitude of spike waveforms (B) for the high-density spiky probe and the hockey-stick surface probe (total number of well-separated SUA for each probe type: surface probe, $n = 32$; spiky probe, $n = 112$). On the box plots, the middle line indicates the median, while the boxes correspond to the 25^{th} and 75^{th} percentile. Whiskers mark the minimum and maximum values. The average is depicted with a blue dot. Black dots correspond to individual measurements. Data on panel (B) are plotted on a logarithmic scale. ** $p = 0.0078$; *** $p = 0.0000049$; Welch's t-test

probe and 112 for the spiky probe. Since I had an unequal number of recordings from the two probes (17 positions for spiky probe, 9 positions for hockey-stick probe), I calculated the more sophisticated '*unit yields per position*' ratio. On the box plots, the middle line indicates the median, while the boxes correspond to the 25th and 75th percentile. Whiskers mark the minimum and maximum values. The average is depicted with blue dots. The average yield was 6.6 for spiky probe and 3.6 for the surface probe. The average signal amplitude was 139.2 $\pm$ 96.4 μV in the case of spiky probe and 89.08 $\pm$ 30.2 μV for the hockey-stick probe. While the maximal signal amplitude was only 162.32 μV for the hockey-stick probe, the spiky probe had 576.79 μV. It is also clearly visible that several extreme big SUAs of spiky probes exceeded the maximal value of the hockey-stick probe. Larger average spike amplitudes may correspond to closer cells, since it was already discussed that single unit EAPs are decreased and flattened over distance [2, 6, 19, 58]. For both compared parameters, i.e. unit yield and amplitude, the spiky probe had significantly better results (** p = 0.0078; *** p = 0.0000049; Welch's t-test), well outperforming the surface probe.

It is important to note that the number of contact sites is not the same for the two probe types. This unbalanced difference could lead us to biased conclusions regarding their electrophysiological performance. Thus I also normalized the results by repeating the same analysis by considering only the first 24 contact sites of the spiky probe. For the exclusion, I have chosen

DOI:10.15774/PPKE.ITK.2020.005

the last 8 contact sites of the spiky probe, since the frontal part of the probe was positioned and fitted to pyramidal layers during insertion. Since both probes are laminar, they became even more comparable by applying this constraint. In addition, the used spiky probe version has an inter-contact distance of 25 μm, while the hockey-stick probe has 50 μm, thus the latter one sampled twice as long area than the former one. These results remained still significant both for single unit yields and for spike amplitudes ($*$ p = 0.044; $***$ p = 0.000019; Welch's t-test). In this constrained case, total single unit yield was 32 for the surface probe and 97 for the spiky probe. Averaged single unit yield was 3.56 $\pm$ 1.94 on the hockey-stick probe resulting in a normalized value of 0.148 $\pm$ 0.081 units per contact site. For the spiky probe, averaged single unit yield was 5.71 $\pm$ 3.2 resulting in a normalized value of 0.238 $\pm$ 0.133 units per contact site. Averaged spike amplitudes were 89.08 $\pm$ 30.21 μV for the surface probes and 138.59 $\pm$ 96.38 μV for the spiky probes. Please note that despite all the numerous apparent benefits of the hockey-stick surface probe such as bigger inter-contact distances, smaller impedances and bigger contact site areas (alias bigger chance to "*being at the right spot*"), the spiky probes (with smaller contact sites, bigger impedances and smaller inter-contact distances) improved the quality of recording significantly.

As the impedance values, together with single unit yield and spike amplitudes remained comparable after 17 insertions, I suppose that these spiky probes can be used repetitively for more than 25-30 times, in other words more than 100 hours of recording may be achievable with the device. However, a thorough monitoring of the quality of contact sites is mandatory when a particular probe is re-used. Lastly, an immediate washing or cleaning procedure is important after every experimental day for maintaining their long-term stability (see Methods section 3.3.2 for related details).

4.1.5 Waveform analysis of extracellular action potentials recorded with high spatial resolution

I report all SUA data obtained using the spiky probe in Figure 4.10/B. I used a hierarchical clustering for separating the recorded EAPs into putative cell types based on their through-to-peak times. Based on the clustering results, spike waveforms having a trough-to-peak time below 0.8 ms were classified as putative interneurons (narrow spikes), while remaining clusters were considered as putative principal cells (wide spikes). In addition, two representative data (Figure 4.10/A & C) illustrate how the close-packed contact sites of the high-density spiky probe (with 25 μm inter-contact distances) can spatio-temporally oversample a single unit EAP. These data also describe how the waveform of the EAP can vary over distance, across several adjacent contact sites. I show the average EAP waveforms and the corresponding autocorrelograms of two different single units recorded with the same probe at the experiment. Autocorrelograms (Figures 4.10/D & E) were plotted in 100 ms duration and divided into 5 ms bins. The sharpest signals (where the waveform has the shortest temporal extent) were detected at Channel #8 (Figure 4.10/A) and Channel #12 (Figure 4.10/C). The spike counts over a recording duration

DOI:10.15774/PPKE.ITK.2020.005

of 3 minutes were #312 and #158, respectively. Based on the work of Barthó et al. (2004) and Csicsvári et al. (1999, 2003), the trough-to-peak time (or the half-width) of spikes itself may be enough for separating two putative cell type groups from the recorded SUAs [65, 66, 83], as it is shown in Figure 4.10/B.

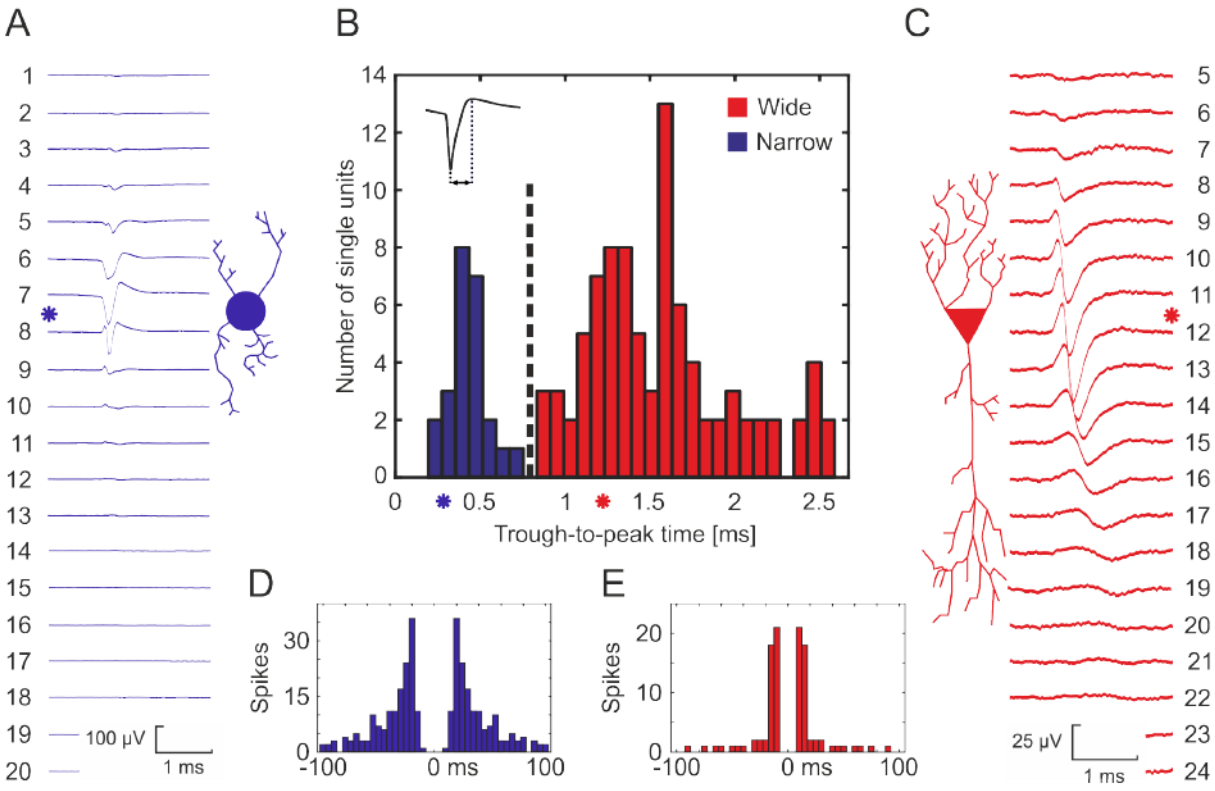

Figure 4.10: Clustering results of putative cell types based on their recorded extracellular waveforms. Averaged EC traces of a putative interneuron (shown in blue) with corresponding autocorrelogram (A and D). Bimodal distribution of trough-to-peak times of recorded SUA waveforms (B). Hierarchical clustering was used to separate units (shown in black dashed line) either as narrow spiking (blue) or as wide spiking (red) SUAs. Asterisks represent trough-to-peak times of the two selected units. Averaged EC traces of a putative pyramidal cell (shown in red) with corresponding autocorrelogram (C and E). Asterisks next to the spike waveforms represent the sharpest signals (possibly the closest contact sites to the soma). Please note the different propagation lengths and different spiking behaviour of the two putative cell types.

Here I investigated additional parameters in the case of two selected single units, namely trough-to-peak time, presence of the initial capacitive peak, features in the autocorrelogram and spatial spread. The second single unit (shown in red) had a trough-to-peak time of 1.2 ms at the sharpest channel, 4 times longer compared to 0.3 ms of the first unit (shown in blue). Moreover, I have found that the initial positive peak on the second unit (red) was present on numerous contributing channels while the first unit (blue) exhibited the initial positive peak visibly only at the sharpest channel. Investigating the autocorrelograms, the first unit (blue) showed distributed firing patterns resulting in a smooth decay in the histogram (Figure 4.10/D). In contrast, the second unit (red) showed fast and regular-spiking behaviour, resulting

DOI:10.15774/PPKE.ITK.2020.005

in a narrow-range and sharp peak on the autocorrelogram close to the middle refractory period (Figure 4.10/E). The initial steepness was higher for the second unit (red) represented by the immediate peak after the refractory period, unlike the first unit (blue), where the initial peak was built from intermediate steps. Referring to Barthó et al. 2004 and Csicsvari et al. 1999, I clustered the first single unit (blue) to a putative interneuron and the second single unit (red) to a putative pyramidal cell [65, 66]. Lastly, please also note the different spatial propagation of the EAP across channels. In the case of putative pyramidal cell, the signal propagation was rather bi-directional and also longer compared to the putative interneuron. The EAP propagation of the putative interneuron was less significant and almost unidirectional. Interestingly, the more localised putative interneuron showed higher peak-to-peak amplitude of 162 μV while the putative pyramidal cell only reached 72 μV. Such differences can however be also emerged from the variable Euclidean distances and orientation of the cells compared to the axis of the laminar probe [58]. The determination of these parameters remains to be investigated in further experiments such as one presented in the II. Thesis group (4.2) in Section4.2.6.

DOI:10.15774/PPKE.ITK.2020.005

4.2 II. Thesis group: Co-localised, simultaneous intra- and laminar extracellular recordings with corresponding morphology: generation of a ground-truth dataset

The main goal of this chapter is to develop a simultaneous experimental protocol as well as to acquire ground-truth data for validating EAP signals detected by previously introduced and tested silicon probes (using both the commercial NeuroNexus comb probes and the spiky probes). In addition to electrophysiology, concurrent 2P imaging must be included to take full advantage of all the multi-modal information available from co-localised recordings. My effort to record from the same neuron using patch-clamp and a multi-channel EC probe requires a very precise temporal and spatial alignment of the two recording systems as well as visual monitoring for effectiveness. The simultaneous IC-EC set-up was briefly introduced in the Methods Section 3.3.2, here I elaborate on this set-up describing the complete experimental protocol in details, the generation and pre-processing of the ground-truth dataset, and lastly, I present a collaborative work on the application of simultaneous IC-EC plus morphology data on single-cell level model-based CSD calculations.

4.2.1 Detailed experimental methods developed for simultaneous recordings

As the first step, microscope objective needs to be adjusted for imaging the slice surface and for seeking the predefined brain region of examination. Regarding brain region, I search for the stratum pyramidale in CA1 region of the hippocampal formation, since apical dendrites of these pyramidal cells are less branched and better outlined compared to CA3 dendrites. It is important to note that not only the probes need to be positioned but the whole slice should be aligned before fixing it by a holder grid. These horizontal slices can be easily oriented visually by looking the characteristic curvatures of hippocampus and corpus callosum such that the CA1 pyramidal layer will become accessible (in other words free from holder strings) and optimally placed for further insertions. When CA1 pyramidal layer is found by the experimenter and checked to be optimally angled for insertion, as a next step, the multichannel extracellular electrode is positioned above the brain slice. Again, I pay particular attention to adjust the correct X-Z angle and X-Y range in order to place the silicon probe as parallel as possible to the main dendritic axis. The three different silicon probe types used in this study (and introduced earlier in Methods Sections 3.1.1, 3.1.2 and 3.1.3) have different settings for optimal insertion. Since the shanks of the Neuronexus probe are parallel to the printed circuit board (PCB), therefore the probe's contact sites are perpendicular to its axis (please see Figure 4.11 for details). The Neuronexus probe should be implanted diagonally at an angle of 19°. Given this position, the objective is capable to focus on the sufficiently flat probe without touching or bending it, as well as, the probe is steep enough to avoid the wall of the recording chamber. In the case of the spiky probe, the implantation angle is slightly steeper (22°). In this condition, the aforementioned beneficial properties are given; however, here the protruding endings (carrying

DOI:10.15774/PPKE.ITK.2020.005

contact sites) of the spiky probe will be inserted vertically. This is a significant difference, while the Neuronexus probe can penetrate to any depth, the spiky probe has an implicit implantation limit of 50 μm (equal to its own protruding endings). Even if the probe itself can be lowered deeper, it is not recommended because the shank will certainly cut the slice making extensive tissue damage. The depth of 50 μm is well-chosen for co-localised recordings (visually guided patch-clamp recordings become hard to implement below 80-90 μm due to the rapid degradation of camera-mode NIR image quality).

As in every *in vitro* extracellular recording, the surface of the slice is considered as a dead-cell layer with cut-off dendrites and flattened somas. Thus one has to dive into the tissue (minimum -20 μm below the surface) in order to find putative intact cells with physiological signals. A major drawback of the 'hockey-stick' probe (used only in the beginning of the study) was that this modified Plexon U-type angled probe cannot penetrate into the tissue. Even if it can record single units and population activity from the surface, these volume conducted signals (possibly rather coming from deeper layers) will be always attenuated by the dead-cell layer. As it was previously shown in this thesis (in Results Section 4.1.4), penetrating spiky probes are significantly outperformed the recording quality achievable with this surface probe. Since surface patch-clamp recordings are similarly problematic (and resulting non-physiological signals from cells with no input) I discarded to use the hockey-stick probe in co-localised simultaneous recordings and only the results made by the Neuronexus comb probe and by the custom-made spiky probe will be presented in the following chapters. Given an optimal vibratome sectioning angle, signals become step-by-step more detectable when going deeper in the slice. From the depth of -20 μm I always found ovoid shape cells (considered as intact) and the signal enrichment and amplification can be well-monitored visually during the insertion.

Stepping back to implantation process, multi-channel silicon probes are implanted on the left side of the recording chamber. However, their contact site layout is different so their insertion protocol will be different as well. While the laminar contact site row of the Neuronexus comb probe is perpendicular to its main shank, the spiky probe has a contact site layout parallel to the shank axis. Optimal insertion protocol is the following: for the comb probe, the shank has to be inserted parallel to the pyramidal layer (alias perpendicularly to apical dendrites), while for the spiky probe, positions are just the opposite: the main axis is perpendicular to the pyramidal layer, thus it is parallel to the apical dendrites (at least along the trunk region). If these positions are achieved, then there is an increased chance to have a patched CA1 neuron parallel to the silicon probe inserted beforehand.

Figure 4.11 shows four representative simultaneous IC-EC recordings, two different sessions for both probe types. The top sub-figures (A, C) are considered to be successful, parallel arrangements between the contact sites and the cellular somato-dendritic axis. Bottom subfigures (B, D) represents angled, suboptimal positions. Naturally, it is very challenging to find completely parallel cellular processes in the close vicinity of the extracellular probe. Even in the case of correct X-Y situation (as shown on top sub-figures (A, C)), there is an inevitable angle

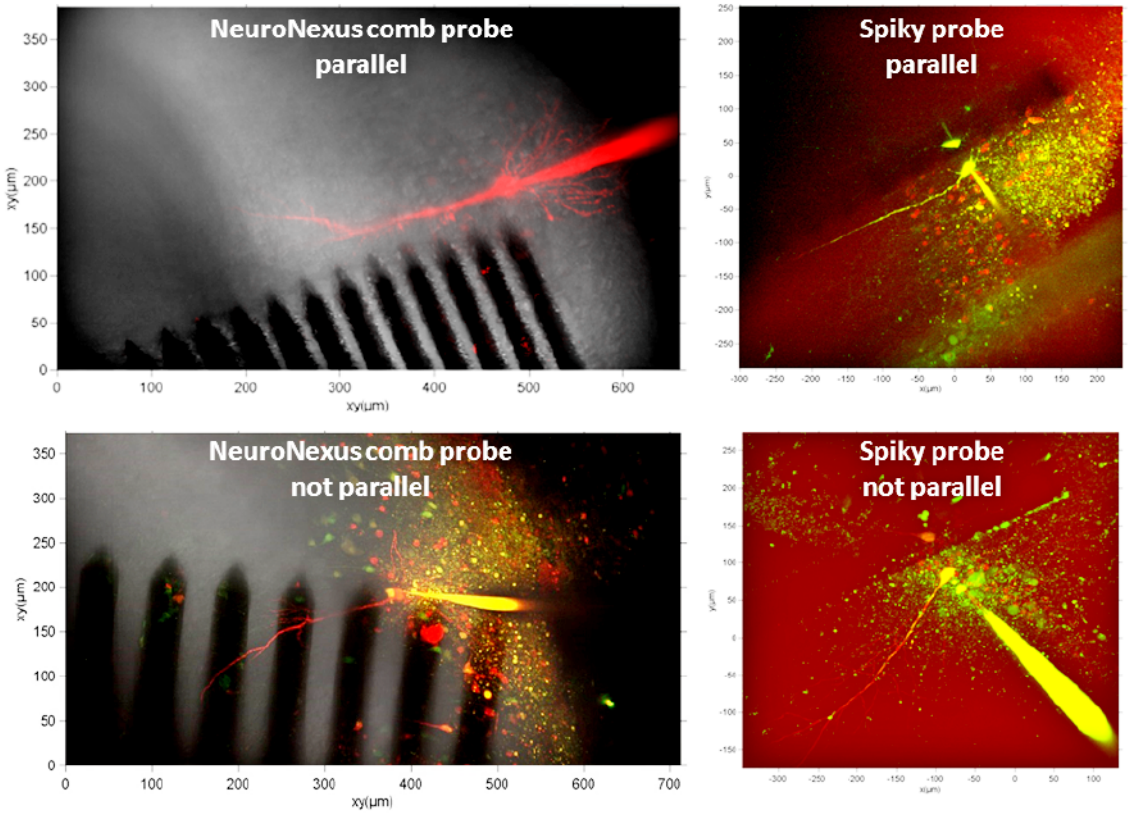

Figure 4.11: Parallel and less parallel arrangements of silicon probes and the intracellular axis in different recording sessions.

in the Z-direction between the cellular axis and the laminar probe which cannot be shown on this 3D→2D Z-stack projections.

Suppose that the EC probe is well positioned above the slice at the right place, angle and direction compared to the CA1 pyramidal layer (for an optimal theoretical arrangement, please visit back to Figure 3.4 in Methods 3.3). The probe was then inserted at a slow velocity ($\sim$ 5-10 μm/s, visually guided, manual insertion via motor-controlled wheels of the Luigs-Neumann controller). After reaching an optimal place and depth with the EC probes (where notable single units and population activities are both present in the raw, broadband signal), I allowed 15 minutes for the brain tissue around the probe to settle before attempting patch-clamp recording. During this period, a freshly drawn micropipette was filled with intracellular solution containing three different markers (previously described, see details in Methods 3.3 and 3.3.1): Alexa594 (red, static, for z-stack reconstruction), Fluo-4 (green, dynamic, Ca^{2+} sensitive) and Neurobiotin tracer dye (for post-hoc histological reconstruction). Attached pipette was then guided and centred to the focus point of the microscopic image (2 mm above the slice), then slowly lowered until reached the surface of the slice. During lowering and penetration, high positive pressure was applied to avoid clogging (or a blockade in the pipette outlet due to tissue contamination). Pipette resistance was checked for every individual pipette in the aCSF, after the application of high positive pressure but before patching. Optimal resistances are expected

DOI:10.15774/PPKE.ITK.2020.005

to be between 6-9 MΩ. Pipettes having resistances lower than 4 MΩ or larger than 10 MΩ were withdrawn and replaced.

Subsequently, a candidate cell for intracellular recording was selected and targeted. When the focus is at tissue level, I observe cells in the targeted region for shape. For target region, I focus on cells located between 20-100 μm below the surface of the slice and located in 20-150 μm distance range from the extracellular probe. Neurons with cell-electrode distance lower than 20 μm were considered to be '*dangerous to approach*' or '*possibly damaged by the extracellular probe*'. Similarly, neurons with cell-electrode distance bigger than 150 μm were also ignored since the chance for capturing their EAP simultaneously by the extracellular probe is extremely small. Cells located deeper than 100 μm are challenging to monitor by using nIR camera (and also challenging to patch them) and surface cells are easily identifiable by their swelled, flattened somas with round nucleus known as dead-cell layer, or cut-cells. Healthy cells should appear as round, ovoid, or elliptical homogeneous structures. Since both extracellular probes were positioned such that their contact site axis penetrated to a depth of 50 μm, cells found within the target region are optimal for simultaneous IC-EC recordings. When a particular candidate cell was selected, I marked it on the computer screen in order to help micropipette guiding. I roughly calculated the insertion place of the micropipette based on triangulation method. In case of missed target, it is always better to retract the pipette and to make the reposition above the slice instead of local repositioning within the tissue. During the approach, the patch-clamp system was functioning in voltage-clamp mode and membrane test was applied to continuously monitor pipette resistance. Close to the target cell, an increase in pipette resistance can be obtained. At the same time, a dimple should appear on the surface of the cell body, at the pipette tip caused by the positive pressure applied earlier. If a combination of these events was detected, we suddenly released pressure - and applied slight suction if needed - to obtain a good seal on the neuron's membrane. Optimally, a high seal resistance (bigger than 1 GΩ, also called '*gigaseal*') can be formed quickly, which will both prevent noise contamination and contribute to the mechanical stability of the patch-clamp. If the gigaseal has formed, fast and slow capacitance were compensated automatically via built-in commands in the Multiclamp system. Then a brief but stronger suction was applied through the tube to rupture the plasma membrane and to allow whole-cell intracellular configuration. After achieving a successful whole-cell configuration, series resistance compensation was similarly calculated automatically, by the program. For the latter, I changed to current-clamp mode where either positive or negative holding current was constantly injected to hold the cell at the desired membrane voltage (close to its resting membrane potential). In current-clamp mode, first step was to run a Ramp test, a pre-defined and incremental series of current injections in order to elicit intracellular action potentials (IAPs) and to find the spiking threshold of the patched cell and by using the spiking parameters (and additional properties such as input resistance) to preliminary characterize the cell type (which will be validated later during the experimental protocol).

Spiking threshold was then determined from Ramp-test and constant holding current injections were adjusted to maintain a membrane potential slightly above the threshold value. By applying this, I was able to generate near-spontaneous spiking behaviour. Holding current injections ranged typically between ± 100 pA, however, in some cases (where the cell had stable spiking at 0 pA level) no holding current was injected and real spontaneous activities were detected. Special care was taken for maintaining constant (unchanged) current injection within one recording session. Current were only adjusted between sessions and changes were tracked. Occasionally, there was a need for re-positioning the pipette within the cell body. This can be done in two-photon mode, since the cell body is immediately filled with fluorescent dyes upon whole-cell configuration (even if other processes are not visible at that time). During adjustment, intracellular membrane potential fluctuations should be continuously monitored and the holding currents are to be adjusted in accordance. If the re-positioning of the pipette is finished, Ramp-test was repeated to re-calculate the sensitive intracellular properties. Please also note that I can only change the pipette position but not the position of the extracellular silicon probe. The latter would certainly cause the loss of the patch-clamped cell due to tissue movements around the probe.

When basic intracellular investigations (Ramp-test, parameter calculations, and pipette adjustment) are successfully finished and the patch-clamped cell is considered to be stable, simultaneous IC-EC recordings can be started. For initializing the simultaneous recording protocol, triggers coming from the two-photon microscope were applied and synchronized. Actually, I made a so called '*fake*' line-scan protocol, where PMT detectors and shutters were closed in the light path (so no imaging information were detected) but digital signals as triggers could be transmitted from the set-up towards IC (Multiclamp amplifier and DIGIDATA digitizer) and EC (INTAN FPGA acquisition system) instruments. For the majority of recordings, IC data has been recorded twice, both by the IC signal processing system and by the ADC input of the FPGA board. This was necessary for achieving sub-millisecond accuracy and for excluding any possible additive delays due to dual signal processing. It is important to note, that IC data recorded on the ADC input of the FPGA board is 3 orders of magnitude larger than multichannel EC data simultaneously recorded on the very same board. In the case of IC recordings, signal amplitudes (during spikes) reach 100 mV changes, while EC SUA signals are ranging usually between 50-500 μV). I experienced significant cross-talk artefacts on EC channels in times when IC spikes occurred. Thus I lowered the gain of the IC signal to its minimal values (1, which means tenfold amplification). Moreover, I had to implement a level-shifter for IC signals, since the ADC input of the INTAN FPGA board can only accept positive voltage values (from 0 V to 3.3 V). This was done by manually adjusting the DC offset of the patch-clamp in Multiclamp. Note that this value may vary for each recording session (since it depends on the actual membrane potential). DC offset shifting values were always tracked for each recording session and later they have been transformed back (during off-line analysis in MATLAB) to

DOI:10.15774/PPKE.ITK.2020.005

get the real intracellular voltage values. By applying these regularizations, cross-talk artefacts could be minimized and at the same time, a proper synchronisation could be achieved.

In simultaneous IC-EC mode, 3 minute long sessions were recorded while holding currents remained constant. This length was short enough to maintain unchanged physiological conditions, but also long enough to collect reasonable amount of spikes. Inclusion criteria for a successful simultaneous measurement were the following three conditions: I expected detections of at least 100 spikes for each 3 minute session (1), constant holding current injected for maintaining stable spiking had to be small enough, ideally below 250-300 pA (2), and after pre-processing, spikes of the patch-clamped cell should be detectable on at least one EC channel in the spike-triggered average (STA) form (3). This STA is also referred sometimes as "spike-field" of the patch-clamped cell in literature [22]. Please note, that spikes of the patch-clamped cell not often appeared on any EC channels in the raw dataset, even if this would be necessary for blind EC spike sorting (without the knowledge of ground-truth spiking) [122, 159]. Here I only state that for my inclusion criterion, I need to be able to detect extracellular footprints of the patch-clamped cell in the averaged STA signal, which is a weaker requirement than the EAP appearance in raw recordings. Luckily, this can occasionally results in spike detections of patch-clamped cell for both (raw and pre-processed) types of EC signals.

If simultaneous IC-EC datasets were successfully recorded and the patch-clamp could still be considered stable, as a final step, I changed back to two-photon mode on the microscope and made a large-volume z-stack projection for revealing the 3D morphology and cell-electrode distances. The Field-of-View (FoV) of the z-stack projection was set to cover both the EC probe location and main cellular compartments (soma, apical trunk region and proximal apical and basal dendrites). Depth levels (z-dimension) ranged from -200 μm to 0 μm, which is the surface of the slices. As described before in this section, patch-clamped cells were located always between -40 and -100 μm below the surface and EC contact sites were positioned to -50 μm depth. The resolution of the z-stack (or the step between stacks) was 3 μm, which was enough to capture small dendritic processes along the 3D morphology.

In the end of the experimental protocol, patch-clamp recording was set back to voltage-clamp mode, pipette was then carefully withdrawn (with visual monitoring in tIR camera-mode), slice was removed from the dual perfusion chamber and dropped immediately into room temperature paraformaldehyde (PFA) fixative solution for *post-hoc* histological reconstruction.

Here, I have tried to delineate important steps and underscore crucial parameter settings that must be controlled for achieving successful and rigorous intra- and extracellular recordings from the very same cell. In the following section, results recorded by the experimental protocol will be presented and even further modification possibilities will be discussed.

4.2.2 Main parameters of the ground-truth dataset

At the time of submission, a total of #16 neurons were successfully recorded from #12 animals with the developed simultaneous and co-localised protocol. This library building is currently in progress and to be updated whenever a new successful, candidate data becomes available. Apparently, every recording session has its different *pros* and *cons* regarding cellular properties or recording settings. All these varying parameters will be released together with the dataset. I advise the Reader to select cells having the most favourable, pre-defined criteria based on this summary table. Currently, out of the #16 neurons included in this library, only #1 interneuron was recorded and #15 were found as pyramidal cells. The goal is to hunt for interneurons in the near future and possibly, this number will be increased. Regarding probe types, #7 neurons were recorded using my custom-made spiky probe (for technical details, please see Methods 3.1.3 and the first thesis group in Results 4.1). These neurons are coded in the dataset as (sp_1-7). Within this dataset, #4 neurons were recorded with the densest version (with inter-contact distance of 25 μm) and #3 neurons with the medium version (with inter-contact distance of 50 μm). The only interneuron I recorded until now (namely, sp_4) belongs to a session made by the medium spiky version. Moreover, #9 neurons were recorded using the Neuronexus comb-probe (detailed description can be found in Methods 3.1.2). These neurons are coded in the dataset as (nn_1-9), where #4 sessions were made using the long version of the comb-probe (with inter-contact distance of 100 μm) and #5 neurons were recorded with the dense version (with inter-contact distance of 50 μm).
In the following chapters, representative IC and EC data will be presented from this ground-truth library using both types of silicon probes.

4.2.3 Intracellular firing patterns of pyramidal cells and interneurons

Intracellular analysis will be presented for two representative cells in the recordings: a putative pyramidal cell and a putative interneuron (unclassified into subclass). Ramp tests always started from hyperpolarized conditions where there was no spiking activity detected. Current step (or the difference between individual sweeps) was set to 20 pA and the stimulation length was 500 msec for all the steps. Figure 4.12 and Figure 4.13 depict qualitative and quantitative spiking responses respectively, against the increasing holding current injections for these different cell types. In the dataset, pyramidal cell was taken from the sp_1 simultaneous recording, and the interneuron belongs to the sp_4 recording.

On Figure 4.12, 10 current steps were concatenated and visualized together both for the pyramidal cell and for the interneuron. It is easy to see how differently they react to increasing current pulses. While spikes of the pyramidal cell increased gradually (or linearly) during the test, the recorded interneuron showed a very nonlinear, fast-spiking response.

On Figure 4.13, quantified numerical results are shown from the same Ramp tests. The majority of Ramp-tests were performed completely according to the predefined protocol; I recorded

DOI:10.15774/PPKE.ITK.2020.005

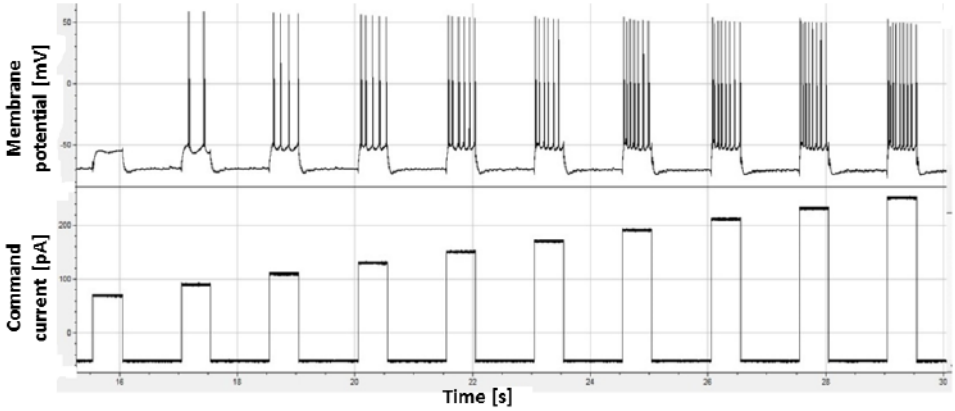

(a) Ramp test for a pyramidal cell

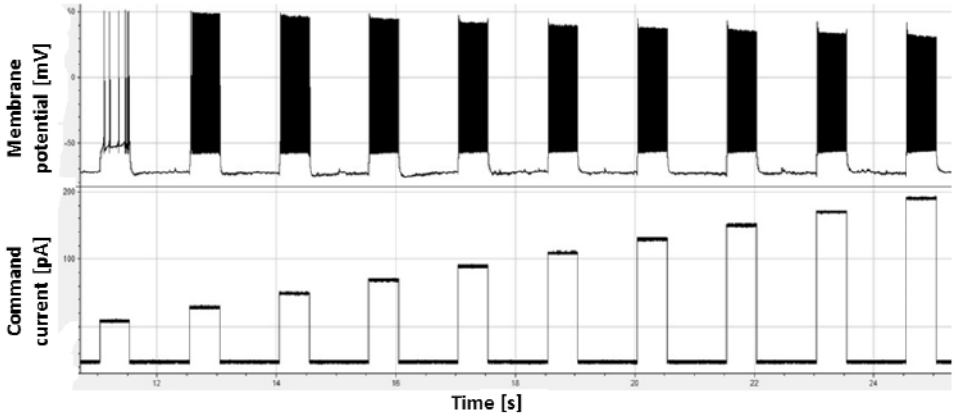

(b) Ramp test for an interneuron

Figure 4.12: 10 concatenated sweeps of Ramp-tests for both two cell types showed qualitatively different spiking responses against increased holding current injections

40 sweeps, starting from -130 pA minimum current injection until reaching the maximum of +650 pA. However, I only plotted 27 sweeps, between the minimum limits of -130 pA to +390 pA. This difference is due to the fact, that for increasing positive current given to interneurons, this types show an excessive activity with high-frequency firing, therefore in order to spare the neuron for further investigation and avoid excito-toxicity, I decided to manually stop the test and exclude the last 13 sweeps from comparative analysis. On Figure 4.13/A we see changes in spike counts for increasing holding current injections. Each marker represents the number of summed spikes for one particular sweep (individual 0.5 sec stimulation). While pyramidal cell have a linear dependence on the holding current inputs, for interneuron the increase in spike numbers follows a nonlinear trajectory. But in both cases, saturation can be noticed, spike count approximated to a certain limit value (20 for pyramidal cell and 150 for interneuron), which they did not exceed. (Please note, that cell types are only putative and estimated yet, even if differences in spiking dynamics are already clearly visible, post-hoc reconstructions are to be performed for final cell type identification and validation.) Figure 4.13/B represents decreased spike amplitudes along the Ramp-test. Moreover it shows that the first spike of pyramidal cell started 4 sweeps later (at +90 pA) than in the case of the interneuron (+10 pA). Finally, ampli-

DOI:10.15774/PPKE.ITK.2020.005

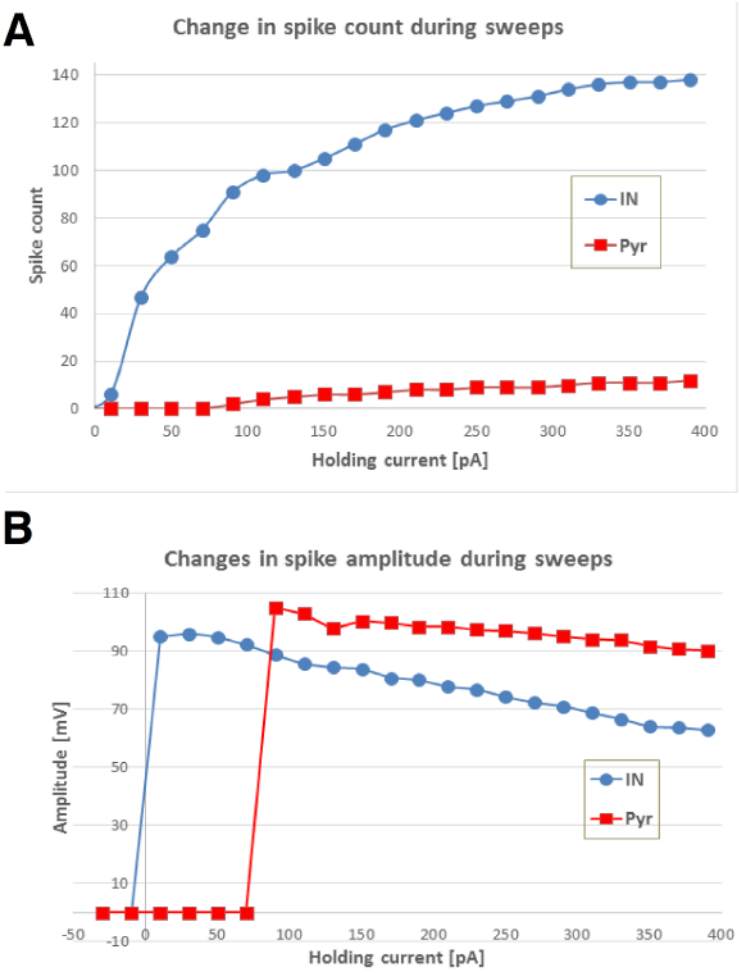

Figure 4.13: Quantified changes in spiking behaviour for an interneuron and a pyramidal cell during Ramp-test protocol. Difference is clearly visible in the spike count responses of two putative cell types (A). Changes in spike amplitudes caused by fatigue in response to increasing holding currents (B).

tudes are slightly bigger for pyramidal cell in this particular case (but this can vary between cells patched differently), but the attenuation in the spike amplitudes over sweeps is more prominent (nearly two times bigger) for the interneuron. This means that while interneurons are more sensitive to current injections, by responding rapid spiking activity, they cannot maintain the same amplitudes for increased input currents (and thus for higher spiking spiking frequencies).

On Figure 4.14 a comparison of three intracellular waveform parameters is presented during spontaneous spiking activity. These intracellular signals were recorded in 3-minute long gap-free mode after performing the Ramp-test (for detailed protocols please see subsection 4.2.1). Parameters considered for waveform analysis were the following: spike half-width (A, yellow) [ms], peak amplitude (B, green) [mV], and spike rise time (C, orange) [ms]. At the beginning of this recording session, it was important to set a similar baseline for both neuron types, because this served as a common reference point. As for the pyramidal cell, I reached -48 mV resting membrane potential with +10 pA holding current, and for the interneuron I injected -30

DOI:10.15774/PPKE.ITK.2020.005

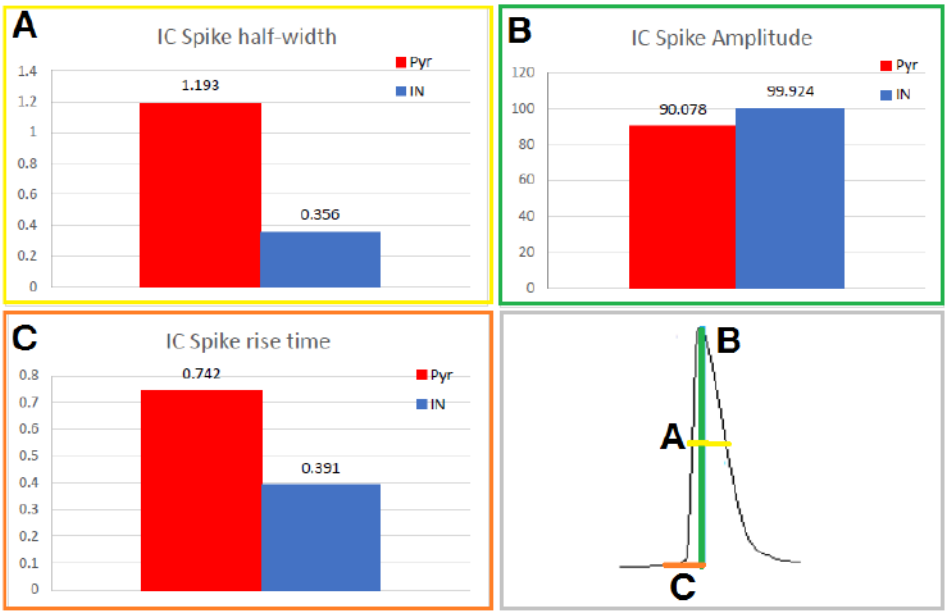

Figure 4.14: Intracellular waveform differences in spiking activity of the two cell types under spontaneous, 'gap-free' recording mode (injecting small, constant holding current to maintain their membrane potential slightly above the spiking threshold). Investigated parameters are the following: IC spike half-width (A, yellow), Maximal IC spike amplitude (B, green), IC spike rise time (C, orange).

pA current to adjust the baseline to -50 mV. With these settings, my goal was to adjust the membrane potential close to its natural threshold value and to perform continuous recording with spontaneous-like neuronal activity. Based on the computed waveform parameters, I can conclude that the complete waveform of the interneuron is clearly narrower than the pyramidal cell waveform. While interneuron has a spike half-width of 0.356 ms, for the pyramidal cell, the spike half-width is 1.193, and similarly, the interneuron has smaller rise time of 0.391 ms, compared to 0.742 ms for the pyramidal cell. These temporal findings are in agreement with the results of extracellular waveform analysis described in the first thesis group (please see subsection 4.1.5) and may serve as a ground-truth for extracellular cell type classification. In contrast to clear temporal differences, the spike (or peak) amplitudes are highly dependent on the experimental conditions and on the successfulness of patch-clamp, thus amplitudes can vary even within one cell type across trials. Here, the amplitude of the analysed pyramidal cell was smaller, but the difference remained practically negligible.

4.2.4 Extracellular spike-triggered averages of patch-clamped cells

Multi-channel EC signals were pre-processed before comparative analysis. (Please see Methods 3.4.1 and 3.4.2 sections for details.) Briefly, the process of analysing EC data started with the spike detection based on the additional IC channel. Events files are generated containing the spike timings of the detected IC spikes. As described earlier, I wanted to detect multi-channel EC "footprints" of these IC recorded spike times. To achieve this, epoch file (*.eeg* extension)

DOI:10.15774/PPKE.ITK.2020.005

were generated, using a 200 ms long symmetrical time window (± 100 ms) around each event time. Next, epochs were averaged across all channels (*.avg* extension). These averaged windows were defined as extracellular spike-triggered averages (STAs) of patch clamped cells. For the majority of paired recordings, a high proportion of spike co-occurrence could be detected on multiple STAs (across neighbouring EC channels) with sub millisecond delay, confirming my earlier assumption that EC and IC probes sampled the very same cell (which was further validated by visual monitoring of the recording). Although EC footprints of IC spikes had very short latency, if signals remained unfiltered, long STA time windows allowed us for investigating the relationship of the patched cells to their local population (represented as sharp waves or MUA in phase).

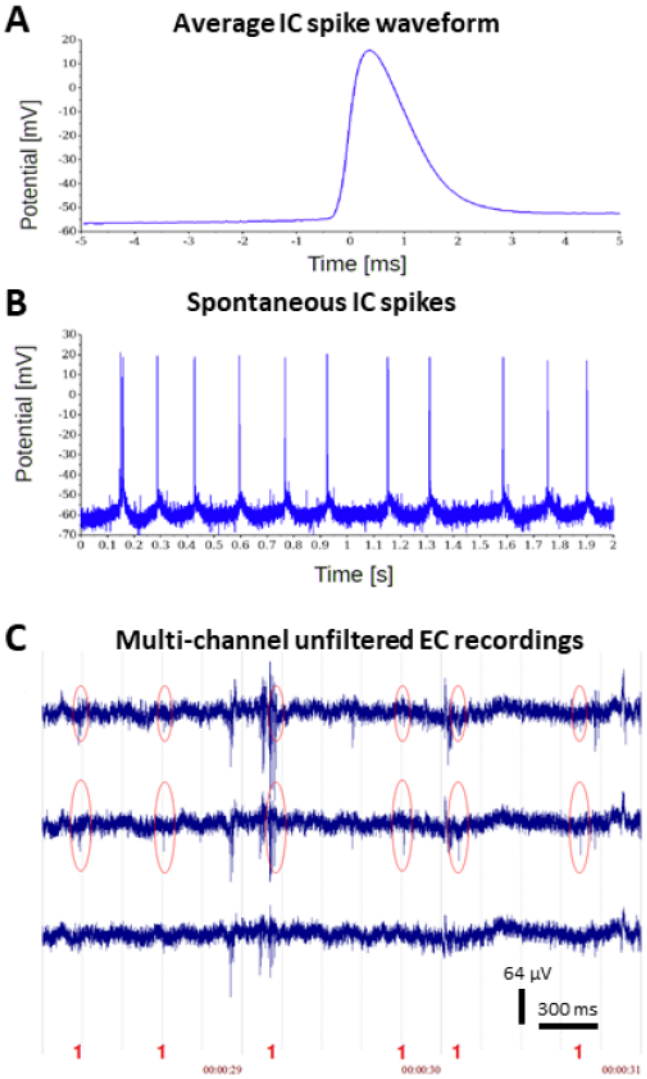

Figure 4.15: Ground-truth recording example. Averaged IC waveform recorded by patch-clamp (A). Current-clamp spontaneous spiking activity in gap-free recording mode (B). Three contributing EC channels are selected and plotted together with corresponding IC events (C). Spike times in red are shown in the bottom row. I could identify the EC contributions of IC spiking on multiple channels even in the raw, unfiltered data (EAPs are highlighted with red circles).

Figure 4.15 depicts an example for ground-truth recordings (*sp_7* in the dataset). Figure 4.15/A shows the averaged IC waveform recorded by patch-clamp. On Figure 4.15/B we see spontaneous spiking activity of the patch-clamped cell held by constant low current injections in gap-free (or continuous mode). On Figure 4.15/C three particular EC channels are selected and plotted (while all channels were recorded) together with the corresponding IC events (or spike times, represented as red '*one*' markers in the bottom row). Here, I actually could find the footprints of IC spiking on multiple EC channels even in this raw, unfiltered data (EAPs are highlighted with red circles). Such a dataset may prove especially useful for spike-sorting approaches based on blind source separation and for validation of different sorting algorithms. But even if the patched-cell is not that easily recognisable, further analysis can resolve its hidden effect on the EC potential. If IC data cannot be firstly visible on any EC channels during raw recordings, STAs of the ground-truth dataset is still can be very useful for for validation and improvement of computational modelling of single-cell EC fields, i.e. determining how a neuron's location and morphology contribute to its extracellular signature. Such an application will be shown in the following section based on a ground-truth dataset having smaller (and hardly visible) amplitudes.

To reveal a detailed spatio-temporal EC contribution of the patch-clamped cell, on Figure 4.16 I show how the aforementioned data can be further analysed. Figure 4.16/A show one epoch of 20 channels (out of 32). As described earlier, the number of epochs generated based on the event file equals to the number of IC spike in one recording session. The patch-clamped cell is most visible on the 12^th channel (middle row, 4^{th} channel from left). Please also note in this case the presence of SWR activity gradient on multiple neighbouring channels which precedes the intracellular spike (or termed as phase-locked). On Figure 4.16/B, spike-triggered averages (STAs) can be seen for the same selected 20 channels. EC footprint of the patch-clamped cell is biggest on the 12^{th} and decays in both directions. The effect of phase-locked, occasional SW activity is less prominent (it may be averaged out across all epochs). 4.16/C show the same STA signals but overlaid from channel 9 to channel 17. This sub-plot can provide detailed spatio-temporal information about the patch-clamped cell in the EC space with time resolution of sub millisecond in time and linear space resolution (here, using the densest spiky probe) of 25 μm. Note that the epochs (therefore the STAs as well) were aligned in time to the peak of the patch-clamped cell (stored in the event file), while the spike was initiated 0.2-0.5 ms earlier. Though the small sample size of my simultaneous dataset precludes strong, direct conclusions, such detailed EC STAs together with ground-truth IC spikes and reconstructed morphology can provide invaluable data for further data analysis methods or model-based single cell calculations as shown in the following section using one of the first recorded neurons by my simultaneous experimental protocol.

DOI:10.15774/PPKE.ITK.2020.005

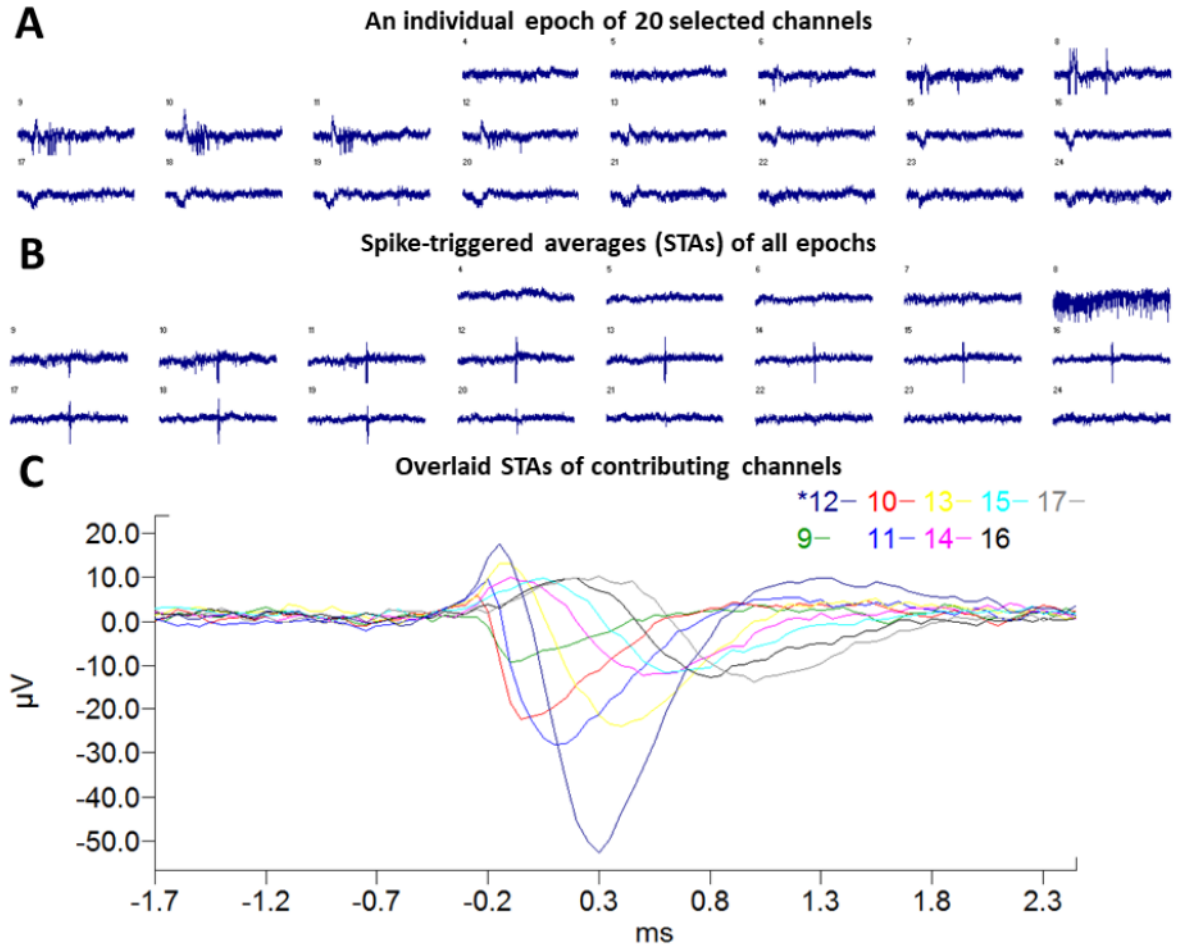

Figure 4.16: Extracting average spiking activity (STAs) from ground-truth recordings. Epoch of 20 channels out of the total 32 (A). The patch-clamped cell is most visible on the 12^{th} channel (middle row, 4^{th} channel from left). Please note the presence of SWR activity gradient on multiple neighbouring channels which is phase-locked and precedes the IC spike. Spike-triggered averages (STAs) for the same selected 20 channels (B). Negative EAP footprint of the patch-clamped cell is largest on the 12^{th} and decays in both directions. Same STA signals but overlaid from channel 9 to channel 17 (C).

4.2.5 3-D reconstruction of cell and probe locations

Patch-clamped cells were implicitly filled with histological tracer molecules via diffusion of the IC solution containing either biocytin or neurobiotin. While well-filled neurons have already showed detailed dendritic morphology in fluorescent two-photon z-stack projection using Alexa 594 (red) and Fluo-4 (green) dyes, histological tracers are much smaller molecules allowing the *post-hoc* reconstruction of very fine processes (including axons). (For technical details of the histology, please see Methods section 3.5) In every case where all histological steps (fixation, re-slicing, and the precipitation of the tracer) were successful, neurons were chosen to be digitally 3-D reconstructed by the Neurolucida system.

Figure 4.17 shows two examples taken from the dataset including both the filled neuronal

DOI:10.15774/PPKE.ITK.2020.005

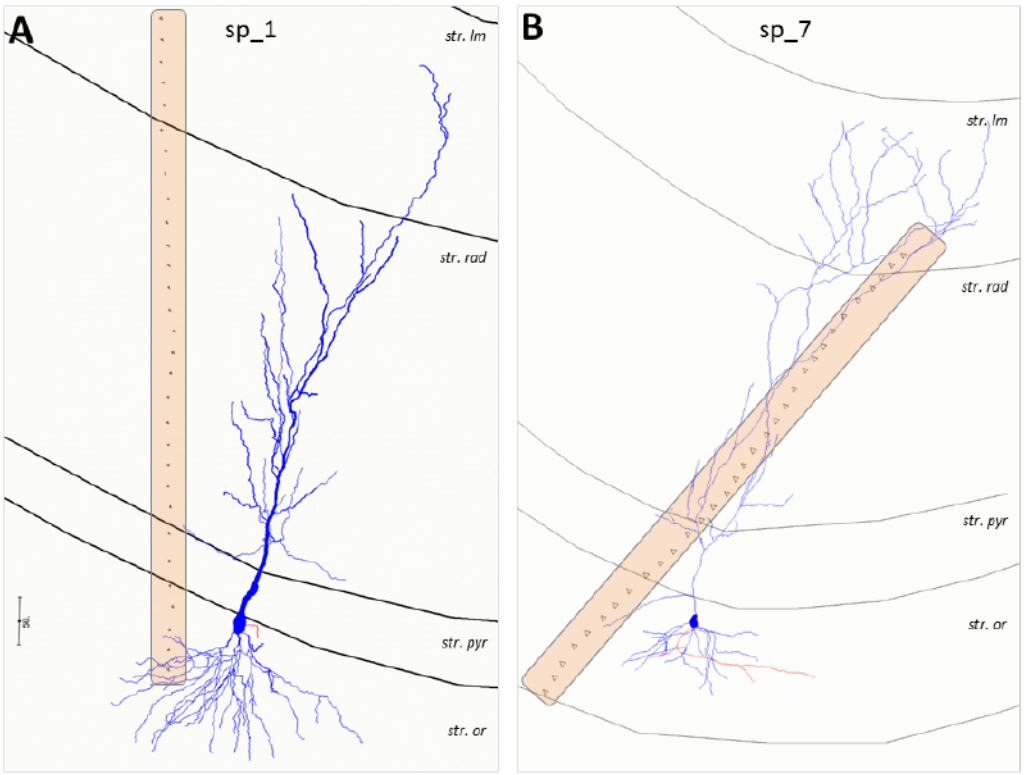

Figure 4.17: 2-D snapshots of two complete 3-D reconstructions of the complete neuronal morphologies and corresponding EC probe traces. Please note the effect of small but visible tissue displacement caused by the fixation and re-slicing processes on the linearity of EC contact sites.

morphology (blue colouring corresponds to dendrites and red for axons) and the markers (small circles or triangles in orange boxes) of EC contact site positions. Regarding the axis of EC contact sites, a small but visible tissue displacement was present in Figure 4.17/B (*sp_7*) caused by the fixation and re-slicing processes. Rectangles of different widths (in light orange) indicate the amount of tissue displacement along the EC contact sites. The effect of tissue displacement was much less on Figure 4.17/A (*sp_1*), as here the points of contact sites form a quasi-linear axis (which can be further checked for all different rotation angles in 3-D). Although the complete axonal arborisation could not be revealed here, initial axons were found in both cases after zoom-in (shown in red). Please also note, that both cells were located partly outside of the main pyramidal layer. This was similar for the majority of patch-clamped cells in the dataset. The cause is profane, as these '*outsider*' cells proved to be easier to access by the micropipette, nevertheless, they still belong the main pyramidal layer.

With the help of Neurolucida 3-D reconstructions, cell-electrode distance (or more precisely, the distance between contact sites and sub-cellular compartments) can be calculated. Having all these structural data together with IC-EC electrophysiology, my next goal is to support model-based single-cell calculations with real experimental validation. Such an example will also be discussed in the following sections.

4.2.6 Experimental estimation of cell- electrode distances

Estimation of the Euclidean distances between sub-cellular compartments and the closest contact site of the EC probe was carried out in two different ways. In a few cases where only the firstly made two-photon z-stack projection was available (without *post hoc* histological processes and the Neurolucida 3-D morphological reconstruction), triangulation was calculated using the sharpest x-y stacks (or focal planes) both for sub-cellular compartments and for contact sites, respectively. After measuring the planar *(x-y)* distance between two points, I determined the depth (z) distance by calculating the difference between stacks (or focal planes) in the z-stack projection. Then I applied Pythagorean theorem to calculate the hypotenuse (or *'c'*) of the triangle, where the two sides are the planar cell-electrode distance (*'a'*) and the depth difference (*'b'*), as follows: $c = \sqrt{a^2 + b^2}$. Since the z step (alias the resolution of the z-stack projection) was set to 3 μm, my distance estimation had an implicit inaccuracy of ± 1.5 μm. Furthermore, considering my own bias (as the subjective, human factor during the calculations) I have certainly introduced an additional error of at least 3-4 μm based on the indefinable sharpness range on the z-stack figures.

In other cases where exact Euclidean coordinates were available both for sub-cellular compartments and for contact sites, we recalculated the triangulation based on the results of the Neurolucida 3-D reconstruction. Again, we possibly introduced some errors with the putative tissue displacements (caused by the fixation and re-slicing processes or inherent software alignment errors). Finally, results of the two different distance estimation methods were compared. Until now, I have not found any notable difference ($d > 10$ μm) between the two distance measuring methods, however, in this case I would consider such a dataset as unconditional and it would be possibly excluded from further, distance-based analysis (titled as a data with "*uncertain estimation*" or "*missing spatial information*").

4.2.7 Application of ground-truth experimental data in cellular-level, model-based calculations

We have seen in Background section 2.2.2 that governing inward and outward currents can be estimated from the measured EC potentials by the inverse-method of CSD. Several CSD strategies were invented to localise current sources on different scales depending on the nature of the specific experimental paradigms. One of the most recent CSD method presented in the literature was the single-cell CSD on realistic neuron morphologies called skCSD [62]. Credits belong to Zoltán Somogyvári, Dorottya Cserpán and Daniel Wójcik for the development of this collaborative project and the author would like to thank that the recorded ground-truth dataset was used for the validation of this novel method.

To examine the experimental feasibility of the skCSD method, we analysed one simultaneous IC-EC data (*nn_8* in the dataset) recorded using the Neuronexus comb-probe together with the patch-clamp filled complete 3-D morphology and pre-calculated cell-electrode distances. The

DOI:10.15774/PPKE.ITK.2020.005

skCSD reconstruction is shown in 4.18 at the moment of firing. Then a 10 ms long video of the spike triggered average is shown on the following Figure **4.19** (clickable in the digital PDF version, after allowing pop-up conditions).
In this recording session, 154 IC spikes were detected on the 3 minutes patch-clamp signal by 0 mV upward threshold crossing. Here, only ±5 ms wide time windows (epochs as introduced earlier) were cut around the events of each spikes on each channels of the EC potential recordings and averaged, to access the fine details of the EC spatio-temporal potential pattern which accompanied the firing of the recorded neuron on all channels. Two faulty channels were malfunctioning (2, 5); however, as the skCSD method allows retrieving CSD maps from arbitrarily distributed contacts, this has not prevented the analysis and the faulty channels were excluded from further calculations. Averaged spatio-temporal potential maps (or STAs) were high-pass filtered by subtracting a moving window average with 100 ms width. This filtering, together with the STA procedure, ensured that the resulted EC potential map contains only the contribution from the actually recorded cell. The price we paid was filtering out EC signals of the spontaneous repetitive sharp-wave like activity of the slice (as also shown in the previous sections), which was correlated by the firing of the recorded neuron and thus the presumptive synaptic inputs of the recorded neuron as well. In addition, one more temporal smoothing by a moving average with 0.15 ms window was used to reduce the effect of noise.

Figure 4.18 captures a moment from the skCSD reconstruction for a typical CA1 pyramidal cell. Figure 4.18/A shows EC potentials measured with the 5 contact sites placed closest to the soma or the neuronal axis. The 0 ms marks the time of the IC membrane potential crossing the 0 mV threshold. The black vertical line marks the 0.40 ms time instant for which the EC potentials and skCSD reconstruction are shown. On Figure 4.18/B, 2-D projection of the cell morphology and positions of EC contact sites marked by stars, the 5 contact sites used in the top panel of the figure are labeled with matching colors. The amplitudes of measured potentials are shown as color-coded circles around the contact sites. Figure 4.18/C depits the skCSD reconstruction on the branching morphology representation. This is a '*snapshot*' of the cell firing, the red color indicates the sinks close to the soma, the blue marks the current sources on the dendrites. Figure 4.19 shows the STAs and skCSD reconstructions as a short video (clickable in digital PDF version, after allowing pop-up conditions). The video shows the recorded potentials and skCSD reconstruction for a 10 ms time window centred around the spike (as described in section 4.2.4. The top panel presents the STAs of the potentials during 5 ms before and after the spike recorded at 5 contact sites closest to the soma. The lower left panel shows the morphology of the cell, contact site positions, and the recorded potentials. Similarly to the above mentioned snapshot picture, contact sites are marked by stars and the amplitudes of the recorded potential are shown as color-coded circles around the contact sites.

DOI:10.15774/PPKE.ITK.2020.005

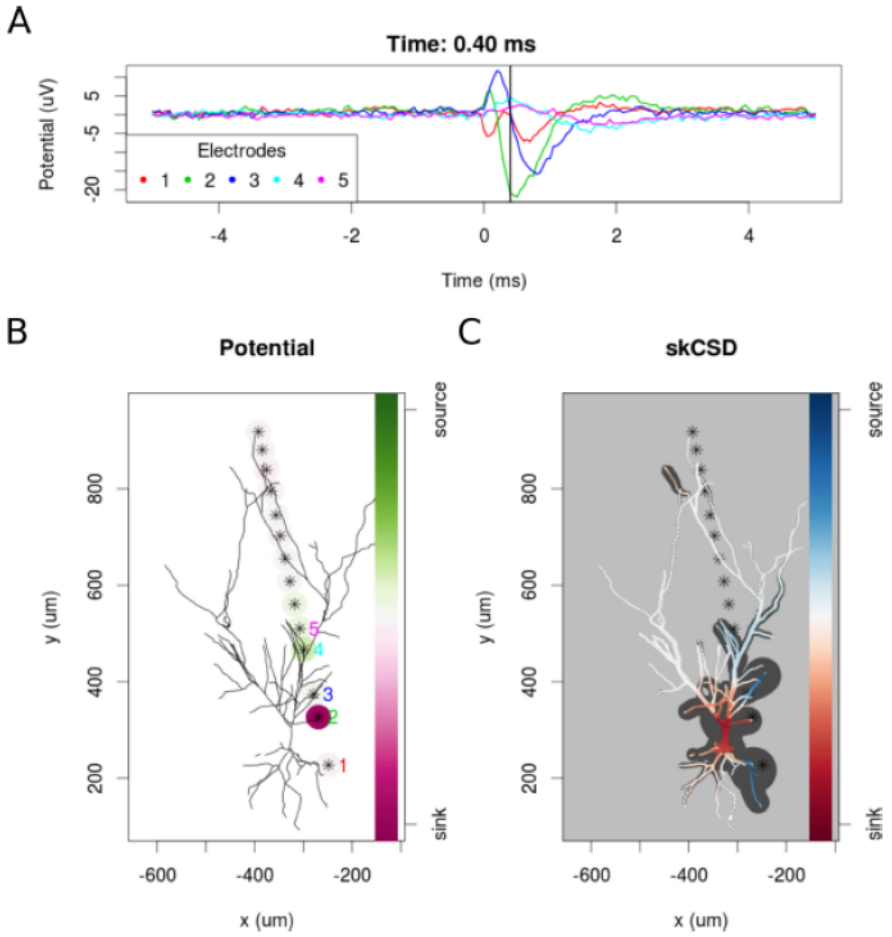

Figure 4.18: skCSD reconstruction of spike-triggered average for a CA1 pyramidal cell. Time course of the EC potentials for 5 selected channels (A). 2-D projection of the cell and silicon probe positions with overlaid EC potential dynamics (B). Reconstruction of current source densities based on the measured EC potentials and modelled cellular morphology (C).

At -0.05 ms the brief appearance of a sink (red) in the basal dendrites is visible which can be a consequence of the activation of voltage-sensitive channels in the axon hillock, or the first axonal segment leading to the firing of the cell (as introduced according to the literature in section 2.1.2. Since there were no contact site sufficiently close to the axon initial segment, the skCSD method did not resolve it, instead it resolved to introduce the activity into the basal dendrite. This phenomenon is quickly replaced by a sink at the soma and in the proximal part of the apical dendritic tree, accompanied by sources (blue) in the basal and in the more distal apical dendrites. The extracellular potential on the second contact site reaches its minimum at 0.45 ms, which signals the peak of the spike. The deep red of the soma at this point signifies a strong sink, while the blue of the surrounding parts of the proximal apical and basal dendrites indicate the current sources set by the return currents. At 1.30 ms a source appears at the soma region, which indicates hyperpolarizing currents. Overall, the observed spatio-temporal CSD dynamics is dominated mostly by the somatic currents, responsible for the spike generation, and the corresponding counter currents.

DOI:10.15774/PPKE.ITK.2020.005

Movie

Figure 4.19: Movie: skCSD reconstruction of spike-triggered average for a hippocampal pyramidal cell (clickable in digital PDF version, after allowing pop-up conditions)

This example demonstrates the feasibility of the skCSD method on recorded experimental data and may help in planning further experiments (as an iterative '*experiment-data analysis*' cycle), aiming to reveal the spatial distribution and temporal dynamics of the synaptic input currents which evoke the firing of a neuron.

DOI:10.15774/PPKE.ITK.2020.005

4.3 III. Thesis group: Combination of multi-channel extracellular recordings and two-photon laser scanning microscopy imaging for the experimental characterisation of photoelectric artefacts

It was shown in the previous sections that microelectrodes (Section 2.3) and optics (Section 2.4) have independently experienced rapid growth in technological development and emerging applications. Referring back to this literature review, extracellular electrophysiology and two-photon imaging (combined with optogenetics) both have advantages and disadvantages in sense of spatial and temporal resolution or structural and functional information extracted. The idea to put them together in one combined experiment comes naturally to gain maximal benefit from both techniques. Researchers were initially enthusiastic to combine the two modalities, however, initial attempts revealed a phenomenon apparently similar to Heisenberg's '*observer principle*', that is the present of the observer affects the observed signal. Namely, optical excitation generates a so called '*photoelectric artefact*' that interferes with electronics and thus can contaminate (practically, often prevent) the EC recordings. According to this observer principle, one must record EC potentials or scan the surrounding tissue but not both at the same moment in time and space. Mutually exclusive combinations may be allowed, as simultaneous EC-2P recordings may not be problematic if recording locations are placed sufficiently far away from each other (not co-localised). Similarly, same FoV (co-localised) but subsequent (not synchronous) recordings may be applied without any photoelectric contamination. However, there is an ever growing need to compare the two signal types in terms of causal roles, sensitivity or ground-truth validation, and to achieve this, both co-localised and synchronous measurements are required. In the following chapters I will shortly overview the features of photoelectric effect and list some possible strategies to overcome its artefact during EC-2P measurements. Then I describe my co-localised and simultaneous recording protocol in details and introduce the off-line, iterative filtering algorithm developed in collaboration. Lastly, I present a few preliminary, representative EC-2P data where photoelectric artefact was successfully reduced, while discussing the limitations and future possibilities of those recordings.

4.3.1 Properties of the photoelectric effect

Photoelectric effect was first observed by Alexandre Edmond Becquerel in 1839. He observed that an unequal illumination of two identical electrodes placed in an electrolyte generated electrochemical currents. This '*photovoltaic*' or '*photoelectric*' effect was then called the Becquerel-effect. Later, in 1887 Heinrich Hertz also reported electromagnetic waves in the presence of high-frequency light. But in fact, Albert Einstein was the first who analytically described the characteristics of the effect (in 1905) for which he awarded the Nobel Prize in 1921. The most important feature found by him was threshold type nature of the effect, below

DOI:10.15774/PPKE.ITK.2020.005

which no electrons can be emitted from the conductor regardless the amplitude or the length of exposure of light. In the case of incoherent light source, emitted photons have a certain wavelength range with randomly oriented phases. Although incoherent light can be collected into beams, their efficiency (or intensity, e.g. number of photons) is usually not high for a small illuminated area. On the other hand, lasers were named after their following abbreviations: '*light amplification by stimulated emission of radiation*', thus they polarise emitted photons forming a virtually single frequency beam with correlated phase (naturally, with a small error range in real implementation). They can maintain this diffraction-limited, narrow beam over relatively large distances. But this capability only holds for transmission in an ideal media. Biological tissue is highly turbid and photons must undergo absorption and scattering which limits penetration into deeper samples. According to the '*Beer-Lambert Law*', light penetration into tissue is a function '*optical scattering coefficient*' μ_s and the '*optical absorption coefficient*' μ_a [160]. While the μ_s in brain tissue decreases with increasing wavelength, the μ_a has a more complex profile. At visible light is highly attenuated by both the high absorption and high scattering, while for NIR light, μ_a is low enough for allowing greater penetration. Thus NIR range is optimal for laser light sources as also applied in Ti:Sapphire laser systems used in this current thesis work.

The aforementioned cut-off threshold for photoelectric effect is highly dependent on the material of the conductor. Surprisingly, this threshold frequency described by Einstein only holds for single-photon events. Maria Göppert-Mayer (already mentioned as the discoverer of 2P effect) found that when two (or even more) photons simultaneously collide at the target, they can greatly reduce the cut-off threshold and thus generate photoelectric effect even for lower applied light intensities.

4.3.2 Strategies to attenuate photoelectric artefacts in combined recordings

Several strategies have been used to avoid or at least to attenuate photoelectric effect but each approach has its own limitations. First, adjusting incoming photons to zero over the conductive medium via masking the location of the implanted probe may have beneficial effects. While masking (or optical blocking) can attenuate photoelectric artefact via absorption, it cannot completely eliminate any residual effect, since photons are scattering in surrounding tissue. A second approach is the use of incoherent light sources. This reduces the probability of photoelectric events, although we lose the benefits of coherent illumination. In addition to this, incoherent light sources cannot be applied for evoking 2P excitation.

In theory, a further technique called '*common-average referencing*' can be also used in the case of multiple, equally illuminated contact sites and an identical reference electrode. But practically, this becomes very difficult or infeasible to realise and maintain perfectly identical illumination for every site (even for the reference) during recordings due to tissue scattering, unwanted movements and to the large distances between contact sites.

DOI:10.15774/PPKE.ITK.2020.005

One can select substantially longer wavelength than the photoelectric cut-off threshold, this can again reduce the photoelectric artefact. However, when applying any of the widely used fluorophores in 2P microscopy, the wavelength necessary for detection falls to the NIR range and coherent light will typically generate overwhelming artefacts. Unfortunately, this cut-off threshold is usually more sensitive than the power required for the emission of excited photons. As an exceptional case, laser power can be as minimal as possible in the case of *in vitro* (single layer) cell cultures and planar MEA recordings resulting in a diminished artefact to negligible levels.

From data analysis point of view, principal component analysis (PCA) can also be used to identify and isolate the majority of repetitive artefact patterns that introduce the largest variance in the recorded data. However, additional strategies are still necessary to completely remove the contribution of the photoelectric artefact. A similar deficiency holds for simple filtering types, which (if applied for longer frequency ranges) may in turn cause too much loss in the useful information content of the signal. Specially tailored comb filters and adaptive filters were developed e.g. in steady-state visual BCI applications or for decreasing noise in MRI experiments or electrocardiography recordings, but there is no application yet published in cellular-level neurotechnology [161, 162, 163].

Most recently, a material dependent challenge is rapidly emerging to find near-transparent conductors ideal for combined electro-optical recordings [20, 164, 165]. Such conductors include '*indium tin oxide*' (ITO), '*poly(3,4-ethylenedioxythiophene*' (PEDOT), or graphene [166, 167, 168, 169]. While none of these materials is fully transparent (and they are getting even darkened over time), the main bottleneck is that these thin-films can typically be deposited on another conductive substrate. Naturally, if any conductive substrate is used, photoelectric effect will be activated.

It seems so far that there is no functional method currently available for using silicon probes (or any other solid-state conductor) in combined recordings. Thus the only way to combine co-localised and simultaneous EC and 2P without any disturbing photoelectric artefact would be the use of ionic conductors instead of solid-state probes. These ionic conductors are mainly made from a glass micropipette with a pulled sharp, opened tip. Opening at the tip of EC pipettes can be slightly bigger than for pipettes used in patch-clamp studies (introduced in Methods section 3.2) and instead of IC solution, they are filled with aCSF or saline. The solid conductor, usually an $Ag/AgCl$ wire (inserted for the back part of the pipette) and the tip will be isopotential due to the conductive solution. Luckily, however, the wire ending will remain relatively far away from the coherent light and as a consequence, photoelectric effect along the wire will be negligible. On contrary, I have to mention open issues such as fragility of these glass devices or glial infiltration and clogging which can prevent longer recordings and thus have to be considered when designing such a device. Even if there are a few theoretical prototypes for microfabricated ionic conductor arrays with well-controlled site spacing, until the date of thesis submission, there were no successful and stable realisation published for ionic conductor arrays

DOI:10.15774/PPKE.ITK.2020.005

in EC recordings. Such a promising framework was recently developed by me and colleagues in our lab (patent pending, please visit related reference in Section 7.2 for details), but there is no functional hardware implementation published yet in this topic therefore this patent does not form an integrative part of this dissertation.
During the following couple of sections I would like to resolve this very pessimistic overview listed here. I present a recording protocol and data analysis method for successfully eliminating photoelectric artefacts in co-localised and simultaneous EC-2P recordings obtained with commercial silicon probes [170].

4.3.3 Experimental procedure

Three Thy1-GCaMP6 transgenic mice were used for data acquisition [115]. *In vitro* neocortical slices were similarly prepared as described elsewhere (in Methods section 3.3.1) except that in this study coronal slices were cut instead of horizontal slices for better mimicking *in vivo* recording conditions, Thereby a perpendicular orientation for probe implantation could be assured respect to the surface of the brain). Experimental set-up including stage, manipulators, aCSF solution, dual-perfusion chamber, reference electrode, temperature and oxygen supply were all similarly applied as described in Methods section 3.3.2 and Results section 4.2.1.
In the 2P imaging side, the Coherent Ultra II laser was working in resonant mode providing random access, almost real-time and whole-area imaging of the surrounding neural tissue. The objective of the 2P microscope had a working distance of 2 mm and a 20× magnification. Typical FoV of the 2P imaging was around 300 × 300 μm. The applied laser wavelength was set to 920 nm which guaranteed the maximal absorption capability of GCaMP6-based Ca^{2+} imaging [115]. On the EC electrophysiology side, longer type NeuroNexus comb probe (with inter-contact distance of 100 μm) was used (please see Table 3.1 in Methods section 3.1 for comparison).
Gaining successful combined EC-2P dataset from this set-up needed some more elaboration before recording. Firstly, slice was scanned through by the microscope in 2P mode for hunting a place with outstanding neural activities. Ca^{2+} signals are known as a proxy for IAPs thus I considered this region, as the optimal insertion place, hypothetically. The implantation of the silicon probe was carried out in normal CCD Camera mode via motorised manipulators with the slowest possible velocity achievable by hand-controlled wheels. When high-amplitude SUA activities appeared on several channels, insertion was stopped, otherwise - if the probe has not found detectable EC signals in a reasonable insertion range - probe was withdrawn and relocated. I left the probe to settle into the tissue for couple of minutes before the first recorded session while small adjustments could be made for positioning the probe even closer to one of the SUAs if needed. With all these preparation in hand, it was ensured that both EC and 2P recordings will contain relevant, high-quality signals during a following, relatively long recording protocol.

DOI:10.15774/PPKE.ITK.2020.005

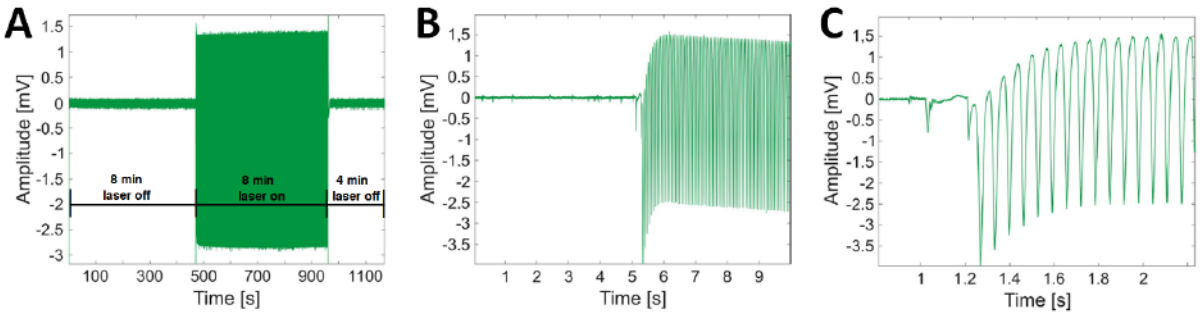

Figure 4.20: 20 minutes long gap-free recording protocol consisting three sub-sections (A) and the initialisation of the photoelectric artefact with two increasing magnifications (B-C).

A 20 minute long, gap-free recording session consisted three sub-sessions. In the first part, 8 minutes of laser-free sub-session was recorded in order to provide reference data before any photoelectric contamination. Secondly, 2P imaging was initiated and as a consequence, photoelectric artefacts were introduced while EC recording was unchanged. This session lasts similarly for 8 minutes. The third and last sub-session of the recording protocol was performed again without 2P laser imaging for obtaining further control data, but this time, after the generated photoelectric effect. Figure 4.20 shows one recording protocol with highlighted sub-sections and the initialisation of the photoelectric artefact in two increasing magnifications. With such a three-step protocol EC changes become tractable before and after laser imaging while combined recordings are also present in the middle part of the session. During this middle part, laser generated photoelectric artefacts exceeded the amplitudes of the highest SUAs at least an order of magnitude. While this artefact covered all SUA signals and made them apparently undetectable, during this period laser scanned 2P images contained numerous active cells and dendrites as also shown in Figure 4.21.

After defining proper '*Region-of-Interests*' (ROIs) for these "*blinking*" cells, quantitative Ca^{2+} spike train dynamics can be extracted (examples are shown on the left) in terms of changes in fluorescence intensities $[\frac{dF}{F}]$. Please note the approximate locations EC probe tips and contact sites highlighted in yellow. High amplitude artefacts generally appeared as large saw tooth-like waves (as in Figure 4.20/C). The main frequency of such waves seemed to correspond to the imaging frame rate of the 2P laser. The frame rate of the imaging is indeterminate (and is a function of many uncontrollable, fixed system parameters). Moreover, these sharp saw teeth and other effects introduce various harmonics other than the main frequency, and thus the elimination of photoelectric artefacts required more subtle methods than applying e.g. a notch or a band-stop filter, as already predicted in the introductory literature review.

DOI:10.15774/PPKE.ITK.2020.005

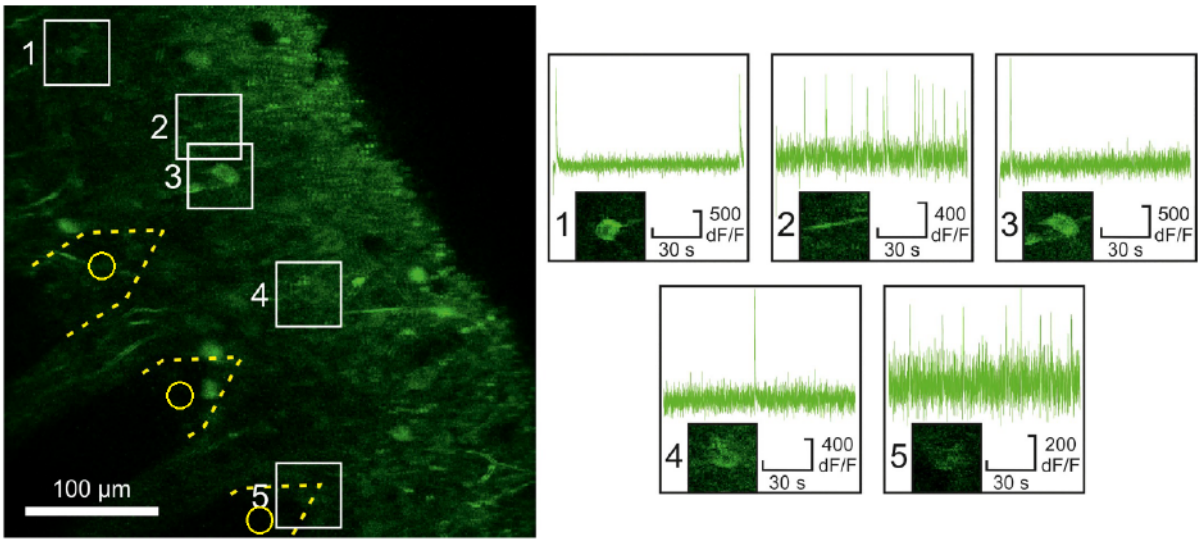

Figure 4.21: Imaging the close vicinity of the implanted silicon probe in a combined EC-2P recording. Imaging reveals both activities of somas and dendtrites (examples are shown on the left) in the same FoV of EC contact sites (highlighted by yellow circles).

4.3.4 Off-line filtering algorithm

Multi-channel EC signals recorded by the INTAN RHD2000 FPGA-based acquisition system were similarly pre-processed as introduced in Methods section 3.4.1 and re-used in Results section 4.1.4. MATLAB software was used for off-line signal visualisation, filtering and analysis. Fig 4.22 summarizes the steps that had been performed by other colleagues in the lab (credits belong to Gábor Orbán and Gergely Márton, details used with permission of the co-authors) in order to accomplish the identification of spike clusters in laser contaminated data.

Firstly, raw signals were band-pass filtered between 300 Hz and 3 kHz to highlight and detect SUAs. Next, a '*Fast Fourier Transformation*' (FFT) was performed to check the characteristic frequencies of the artefact which was found to be in relation with the imaging frame rate of the 2P scanner. This main frequency was found around 15 Hz. Comparing the frequency spectra of the first (laser-off period) part (in every complete session) to their second part (laser-on period), it was evident that the imaging laser gave rise to a population of high peaks in the frequency domain with a periodicity of 15.5 Hz corresponding to the imaging frame rate.

Considering this nature of the artefact, it was a straightforward idea to use a comb filter algorithm to eliminate periodical peaks. Filter modules were built from a set of comb-filters. The parameter defining the number of modules in the algorithm is called N_M. Each module contains band-stop filters fitted to a certain amount of peaks (or centres) in the frequency domain (peaks denoted by f_{peak} and number of filters in one module is N_F). The distance parameter between applied filters in one module (D_F) is a constant 15 Hz here representing the periodicity of the artefact.

DOI:10.15774/PPKE.ITK.2020.005

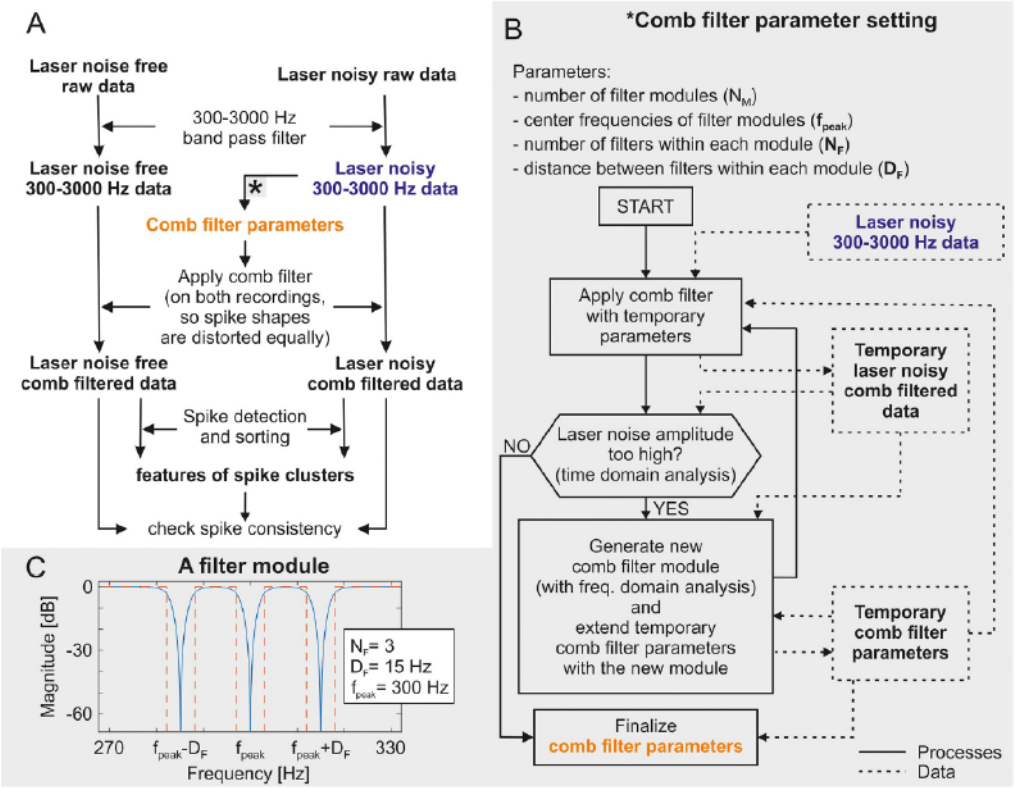

Figure 4.22: Steps of the iterative filtering process. Flowchart for comparative analysis of laser noise-free and laser-noisy data (A), parameter setting algorithm (B) and one representative filter module (C).

Steps for parameter setting are shown in Figure 4.22/B and also in Figure 4.23/B-D. Within a module, N_F will be selected dynamically to reach a pre-defined threshold of 15% from f_{peak} (Figure 4.23/B, grey line and circle show the threshold and the centre frequency, respectively). This will define, how many band-stop filters are needed to go below the threshold with a (D_F) step size. Band-stop filters are identical and have very steep characteristics with cut-off frequencies at below 3 Hz and above 3 Hz of each peak, which result in a 6 Hz of rejected band as shown in Figure 4.22/C and Figure 4.23/D. When such a filter module is generated and applied in one cycle, I switch back to time domain to check whether this temporary filter state was sufficient to reduce photoelectric artefact below 40 μV as a stopping criterion. This voltage value can also be modified if needed, based on the signal quality and the original noise of the EC recording. If periodic laser noise was reduced sufficiently, then temporary filter parameters became finalised. Otherwise, I switch to frequency domain (by applying FFT again on this new data) and a new filter module will be generated with new f_{peak} and N_F parameters. Filtering from now turned to be an iterative process by jumping back and forth between frequency and time domains and defining new modules until sufficiently reduced amount of laser contamination is achieved.

DOI:10.15774/PPKE.ITK.2020.005

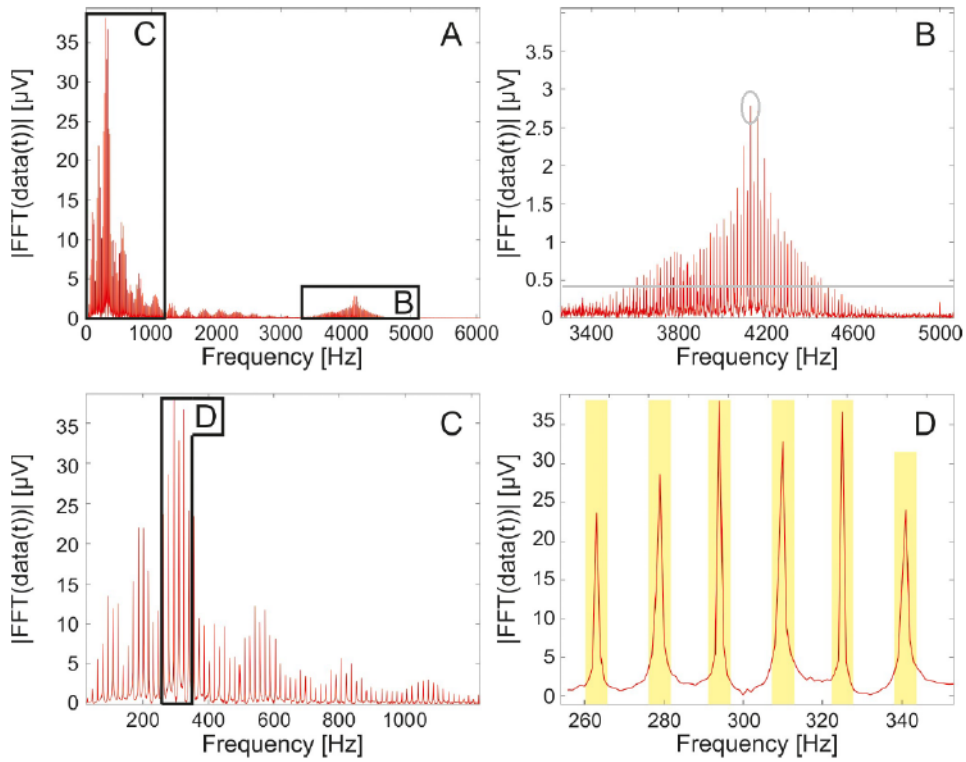

Figure 4.23: FFT spectrum for EC recordings during 2P imaging. High magnitude harmonics are highlighted below 1.2 kHz (C) and at higher frequencies (B). Please note the overlap of the harmonics (B). Rejected 6 Hz frequency ranges (yellow) around periodical peaks within one filter module (D).

4.3.5 Preliminary results from simultaneous opto-electrical measurements

Regarding my experiments when contact sites were located within the FoV of 2P imaging, the laser was able to create artefacts with amplitudes of typically 50 times greater than the amplitude of the largest SUAs. Moreover, we have seen how complicated spectrum of the photoelectric noise prevents the elimination of the artefact via simple filters. As the following preliminary results suggest, the utilization of a comb filter-based algorithm can enable future studies to detect and sort SUAs from these combined EC-2P recordings.

The main trick is that constructed comb filters were applied on both the laser noise free and the laser noisy data in order to '*equally distort*' the spike waveforms in both cases. Later on, this allowed us to match the features of different spike clusters in the laser free and laser noisy measurements. Unfortunately the imaging laser generated artefacts were non-uniform along contact sites, thus recordings from different channels required filters with custom-set parameters. For this reason, we could not perform semi-automatic spike sorting in the Kilosort software package, as described earlier in the I. Thesis (4.1) in Section 4.1.4 and in corresponding Methods section 3.4.1 but we had to use custom-made MATLAB routines. Spike detection was performed by simple voltage thresholding. Three features of each spike were defined for spike sorting: the location of the largest negative amplitude, and values at 250 microseconds (or 5 data points) before and after these peaks. This feature extraction method is similar to traditional

DOI:10.15774/PPKE.ITK.2020.005

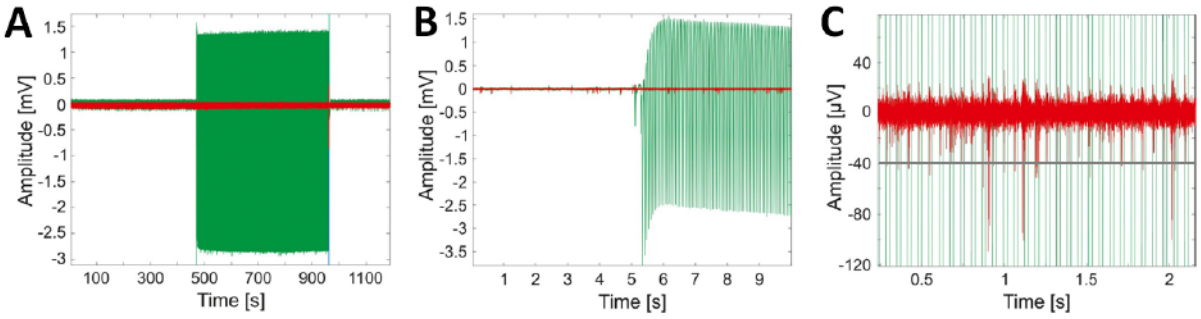

Figure 4.24: Final filtered signal (red) is overlaid on the original (unfiltered, green) data. It is visible that the laser generated photoelectric artefact was significantly reduced and SUAs emerged from the background noise.

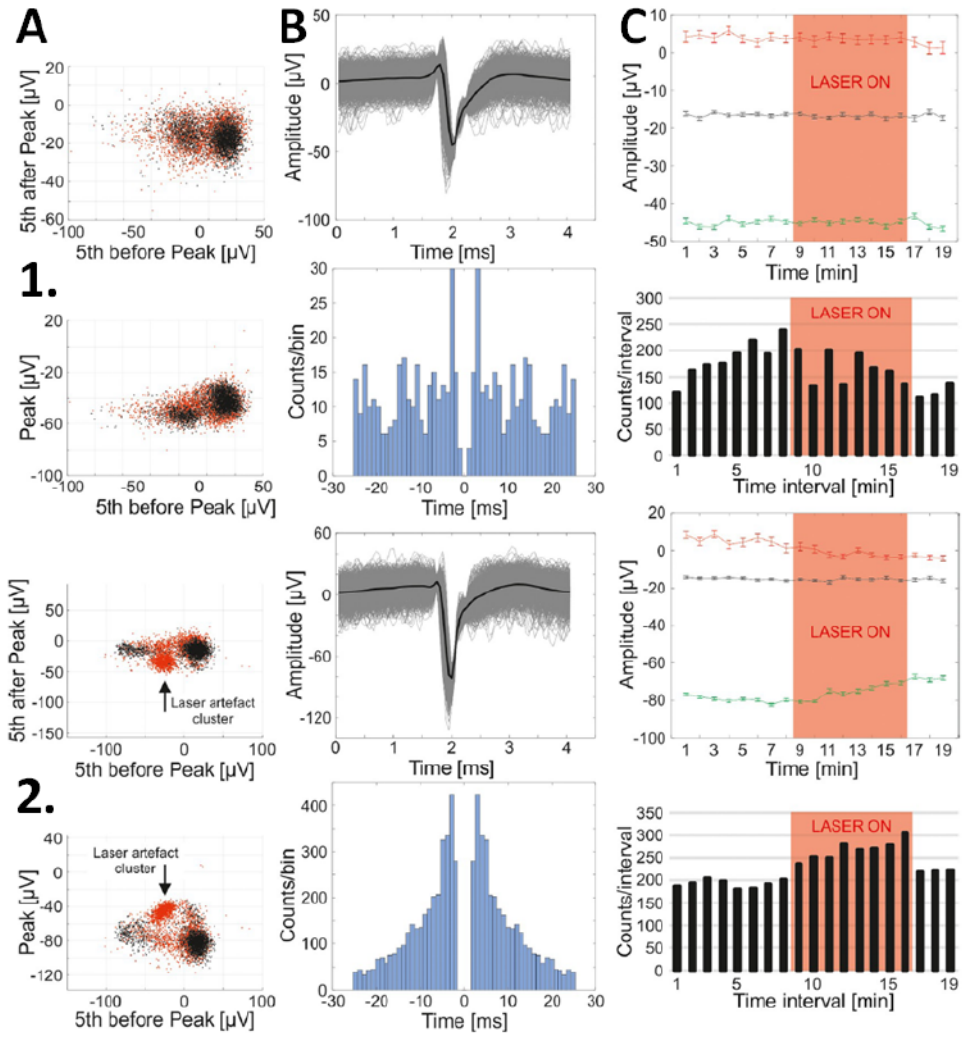

Figure 4.25: Results of the feature extraction (from two different viewpoints) for two representative SUA clusters (A). Averaged spike waveforms and autocorrelograms for these two units (B). Temporal changes of the selected spike features and spike count histograms (C). Laser-on periods are highlighted with red bars.

DOI:10.15774/PPKE.ITK.2020.005

PCA, however it proved to be more robust and easier to use throughout our analysis. The clusters were manually accepted or discarded based on their spike waveforms and corresponding autocorrelograms, in accordance with earlier methods. Figure 4.24 is almost identical to Figure 4.20 except that the final filtered signal (red) is overlaid on the original (unfiltered, green) data. It is clearly visible that the laser generated photoelectric artefact was significantly reduced and SUAs now are emerging from the background noise. It is also evident, however, that artefacts did not disappear and small amplitude spike-like, periodic (15 Hz) artefacts are still present even on the filtered signal around the threshold line (shown in grey on Figure 4.24/C). Fortunately, we can still observe major SUA amplitudes far exceeding the amplitude of these artefacts. Figure 4.25/A shows the results of the feature extraction (from two different viewpoints) for two representative SUA clusters. Black clouds of spikes were detected during laser-off period and red spikes under 2P imaging. Averaged spike waveforms and autocorrelograms for these two units can be seen in 4.25/B. Temporal changes of three selected spike features and spike count histograms are shown in 4.25/C, where laser-on period is highlighted with red bars. While amplitudes (second component, shown in black lines on rightmost subfigures) remained quasi stable for both selected units, please note the incidental modulatory effect of the applied laser on spike counts (lower subfigures). I will shortly discuss putative reasons of this unwanted effect in the following Discussion Chapter 5.

DOI:10.15774/PPKE.ITK.2020.005

Chapter 5

Discussion of the results

Methodological challenges are present in all experimental paradigms related to brain research, thus they show very rapidly expanding fields. From the point of view of the current study, my main goal has been to explore novel approaches to the combined recording of neural signals, namely intra-, extracellular and two-photon fluorescent signals. There were several '*upsides*' of this work that led us to the development of a novel multi-channel electrode, or to different multi-modal datasets using the methodological advancements presented here in this dissertation. However, there were several '*downsides*' as well. As it was shown earlier within the literature review (in Section 2.5), it is critical to demonstrate the recording capabilities and to define limitations of the developed instruments and methods for the correct interpretation of their resulted data. Nevertheless, these issues should not only be considered as obstructions but also as opportunities for future improvements. In this chapter I will shortly discuss all three Thesis groups one after another, although now I will be focusing rather on their flaws instead of their merits. Even if it would be desirable to provide solutions for all emerging drawbacks, some of these major hurdles remained yet unanswered. These issues stress the importance of future work and I will give an outlook for perspectives in the final Section 6.2.

In the I. Thesis group I have presented and tested a penetrating spiky probe for EC recordings, *in vitro*. Thanks to the protruding contact sites, the spiky probe can record from a deeper neural tissue environment resulting in higher spike amplitudes as well as a higher single unit yield compared to a commercially available surface probe. The spatio-temporally oversampled EAPs were visible on multiple contact sites and preliminary clustering methods were applied for separating putative cell type based on their waveform differences.
It has to be admitted however, that the current experimental approach is not designed for long-term recordings. My main focus was to increase the cell accessibility of the contact sites during acute brain slice recordings, consequently, to increase signal yield and recording quality. Future developments may enable such devices to be applied in both chronic and acute recordings, as well as in combination with other modalities such as intracellular recordings, combined optogenetics or microfluidic drug delivery applications [166, 171]. I showed an

DOI:10.15774/PPKE.ITK.2020.005

example for combined 2P imaging and proposed that the spiky probe makes possible consecutive recording and imaging of the tissue at the same region. However, the stability of multi-layered contact sites under higher two-photon laser scanning is yet to be investigated. In addition, as only the contact sites penetrate into the deeper tissue, they may cause less tissue damage than commercially available penetrating probes (such as the 16-shank comb probe from NeuroNexus), but a proper histological validation is also to be performed in this regard. Lastly, I propose one more advantage of the design, namely that it can overcome the so called 'dead-spot problem' [136]. A dead-spot problem appears when the contact sites along the shank are located too far from the tip or the edge of the shank. It becomes difficult or even impossible to approach and record from the closest active cells by an IC glass micropipette, simultaneously, as the probe itself attenuates the neighbouring signals. Recent works in the literature (introduced earlier in section 2.5.2) showed how these paired IC-EC recordings could make new ground-truth data for multi-channel EC electrophysiology [21, 22, 136]. With my protruding design, such co-localised recordings may become easier to perform and to achieve higher signal amplitudes. Moreover, the angled shank can fit under the objective of a 2P laser scanning microscope, thus it is also possible to complete the electrophysiological data with optical information. I conclude that the spiky probe can be a step towards multi-modal experimental designs (as it will be detailed soon within the II. Thesis group (4.2) in section 4.2.1), while they also expand the limits and neural yield achievable by laminar multi-channel electrophysiological systems.

Moving forward to the II. Thesis group, numerous challenges and opportunities were already listed in the ground-truth review Section 2.5.2 regarding the simultaneous IC-EC experiment and its recorded dataset. As it was mentioned in the 4.2.4 section, not every patch-clamped cell can be identified yet in the gap-free recording by using only the EC signal and by applying spike sorting methods. The reason for this restriction is that we still have a considerable distance of 70-80 μm between the EC probe and the patched cell, but according to the literature, the electrode-cell distance must be between 20-50 μm to successfully apply any detection and clustering method. My goal is to get closer to the cells by further optimizing the measurement set-up and process and to record more cells with sortable spike amplitudes. Furthermore, during the simultaneous recording of the IC and EC signals, synchronization problems and artefacts can be emerged between the two systems. When the cell fires, the IC acquisition system necessarily applies the so called '*bridge-balance*' (BB) compensation, which may cause a considerable artefact on the closely placed EC channels. This makes challenging to analyse the exact zero time point of the IC spike. It is possible to remove (e.g. subtract) this crosstalk artefact from any of the EC channels, but consequently, we have to pay the price of loosing some useful information on these particular channels. Although the crosstalk phenomenon is still present in a subset of the recorded dataset, I already have a few successful preliminary data, where IC and EC signals are clear from any crosstalk artefacts. In these

DOI:10.15774/PPKE.ITK.2020.005

cases, a preliminary BB compensation was only set during Ramp tests (when only IC data is recorded) and for simultaneous IC-EC recordings, it was switched off. This is still a sub-optimal solution, since BB compensation is needed for plausible IC spike waveform, however, this change does not affect the accuracy of spike times. Thus these data can be extremely useful for spike sorting applications but not for single-cell calculations. But it is important to note that these aspects are to be further improved as it will be also mentioned in the final Perspectives in Chapter 6.2.

Regarding the application of ground-truth data in skCSD analysis, I also have found drawbacks both for the methods and for the applicability of the data. Technically, skCSD can be applied to any data coming from even a single contact site just like - as an example - the age profile of a human population can also be estimated from a single specimen. But obviously, in these cases, the estimate would be a poor reflection of the distribution of interest. Improving the sampling (by applying more contact sites), the quality of the estimate improves, yet ultimately it is hard to judge *a priori* how many contact sites is enough and what level of precision is required to obtain correct results. Having the estimated distribution of currents, it would be interesting to decompose it into physiologically meaningful components, such as synaptic currents, leak currents, voltage-gated currents for different channels, etc. This seems rather challenging and I do not see a direct way of achieving this from experimental data. It is possible that an application of statistical decomposition methods will prove useful, as in the case of kCSD for population activity [59, 60, 172]. However, I find the contributions to the EC potential from individual currents highly counter-intuitive [173]. In theory, the reconstruction of somatic membrane potential (based on the IC patch-clamp) makes possible the distinction between the two components of the CSD, the resistive and the capacitive current. This distinction provides a clue to the clear interpretation of the CSD distribution, as resistive component corresponds to the active channel currents, both synaptic and voltage sensitive channel membrane currents, while capacitive current corresponds to the passive counter currents. The importance of this distinction is further emphasized by different properties of the resistive membrane current distribution and the CSD: as the CSD is the net membrane current, the sum of the CSD along a whole intact cell should be zero in each time moment, according to the charge conservation (also mentioned in Section 2.2.2). In contrast to this, the sum of the resistive current is not necessarily zero, and it governs the membrane potential dynamics. Thus, estimation of the spatial distribution of the resistive membrane current makes possible the distinction between active and passive sinks and sources of the CSD map and localization of the synaptic input currents, which makes the neuron fire. Even if I have data for the parallel multichannel EC and single channel IC somatic recordings are present now, the necessary tools for skCSD are still under development. I plan to investigate these calculations further in the future. To attempt experimental application of skCSD one must have at least (1) an identified cell of known morphology, and (2) a set of simultaneous EC recordings generated by this cell. Please note that simultaneous IC recording is not essentially needed here, only the morphology. But both

DOI:10.15774/PPKE.ITK.2020.005

other aspects pose their own challenges. Once we have the necessary data the natural question is how to select the parameters of the method in the specific context of a given set-up, specific morphology, and recordings. Although recording the EC potential with a silicon probe, filling a neuron with a dye, and reconstructing its morphology, are standard experimental techniques, using them simultaneously remains a challenge due to the size of the experimental devices which need to be arranged within a small volume. Cells in the vicinity of the silicon probe can be filled individually, or with other bulk loading techniques. Individual recording and dyeing with a glass micropipette provides not only the morphology, but also unambiguous spike times, giving an opportunity to determine the EC potential footprints of the recorded cell. Although these would be favourable data, IC recording less than 100 μm far away from the multi-channel EC probe remained extremely challenging and provided very low succes-rates. Experimental set-ups featuring the necessary equipment already exist ([21, 22, 130, 136]) and introduced in this thesis (in Table 2.5.2 in Background section 2.5.2), but as far as I know, have not been used in this way and have no morphological reconstructions available in their datasets. On the other hand, bulk dyeing techniques result in more filled neurons, although the quality of the dyeing, and thus the quality of the 3D morphology reconstructions, is considerably lower in these cases. Although there are speculative methods for estimation of the cell position relative to the EC contact sites ([5, 58]), association of multiple optically labelled neurons with the recorded extracellular spike patterns is still unsolved. If we can sort the spikes elicited by the neuron of interest we can calculate the STAs of the EC potentials reducing all uncorrelated contributions. Unfortunately, in live tissue, contributions from neighbouring cells will have some correlations due to shared input or due to the so called '*ephaptic coupling*' [130].
As an application of the ground-truth dataset, my colleagues and me have shown how a series of EC recordings in combination with cell morphology can be used to estimate the CSD located on the cell contributing to the recorded EC potential. Since it is now feasible experimentally to obtain the relevant data, I believe that the method proposed here may find its uses in future works to constrain the biophysical properties of the neuron membrane, facilitate verification of morphological reconstructions, as well as guide new discoveries by offering a more global picture of the distribution of the currents along the cell morphology.

Lastly, in the III. Thesis group I presented an experimental method for recording EC signals with penetrating multi-channel silicon probes combined with co-localised and simultaneous 2P microscopy imaging within the same FoV. This was successfully done in such a manner that SUA clusters could be tracked and extracted throughout the whole recording session. While spike waveform parameters remain relatively stable under 2P imaging, I surprisingly realised that these two units were special in a sense that both have been modulated differently under laser-on period. Please note the decreased spike counts for the first unit and increased spiking for the second unit within the red bars. While it is currently unclear, why this phenomenon was not present for other SUA clusters, I hypothesise that such modulations caused by the

DOI:10.15774/PPKE.ITK.2020.005

photoelectric artefact may be due to direct electric stimulation (excitation) of the close vicinity or indirect inhibition (via an excitation of a monosynaptic inhibitory connection) or even due to minimal tissue heating. Electrical stimulation mediated by photoelectric artefact is a novel emerging field as suggested firstly by Takashi Kozai and colleagues (2019) [160, 174] and has its own advantages. However, this is rather undesirable right now in my case, since I planned to image multi-modal spontaneous activity, but the observer's effect previously mentioned in topic introduction can be still present in some parts of the recordings. Further investigations are to be performed to resolve the modulation effect of laser generated artefacts.
Another clear limitation of this proposed method is that when a SUA coincides with a photoelectric wave artefact, it becomes probably also eliminated from the filtered data. However, comparing the width and the density of the laser generated artefacts in time domain with respect to SUA spikes, this limitation should only affect approximately 8.5% of the signal, according to rough pre-calculations. Moreover, a '*clean*', laser noise-free recording data is required before and after the actual combined recording period in order to verify the validity of the obtained spike features, but this requirement may be difficult or unwanted in other applications giving an additional limitation of this work. Lastly, generated artefacts were non-uniform along contact sites, thus recordings from different channels required filters with custom-set parameters. This variability makes our filter design challenging or even infeasible when applying to data recorded with high-density channel silicon probes. An automatic and robust algorithm is to be developed on this matter.

Despite of all the limitations of the aforementioned individual research topics, we have seen that findings of the three Thesis groups yielded new insights into neural signaling by combining intra-, extracellular and two-photon fluorescent signals. Firstly, the penetrating spiky probe was able to significantly outperform a commercial *in vitro* surface probe and provided high-quality single unit data from slice recordings. According to my knowledge, results described in the II. Thesis group were the first attempts in literature to estimate the distribution of current sources along a realistic single neuronal morphology from EC recordings. Lastly, I believe it was again the first time when the possibility of obtaining combined 2P and EC data has been successfully implemented for silicon probes and transgenic *in vitro* slice recordings. These methods might allow future researchers to reveal additional (yet unknown) interconnections between intracellular events, fluorescent activities and high-density extracellular recordings. The application of simultaneous, multi-modal measurements might also give rise to novel findings in designing future brain-computer interfaces.

DOI:10.15774/PPKE.ITK.2020.005

Chapter 6

Conclusions and outlook

6.1 Summary of novel scientific results with related publication

I. Thesis group: Development and testing of a novel, multi-channel spiky probe for extracellular recordings

Thesis Ia. ***I have designed a novel multi-channel, laminar in vitro silicon probe with protruding, 'spiky' contact sites for improved brain slice recordings. I have optically verified the fabricated arrowhead shape, protruding contact sites under scanning electron microscopy. Moreover, I have characterised the electrochemical impedance magnitudes and phase angles as well as the noise level of the spiky probe in physiological saline solution.***

The spiky probe comprises a single silicon shank carrying 32 protruding $Pt/Ir/IrO_x$ contact sites with three possible spacing layouts of 25 μm, 50 μm and 100 μm. With the help of the optimally angled shank, I have shown that the spiky probes are compatible with large in vitro, water-immersion objectives used typically in two-photon microscopy imaging.
The high-density spiky probe (with inter-contact distance of 25 μm) used in the comparative test showed an average impedance magnitude of 1.27 $\pm$ 0.1 MΩ at 1 kHz across all contact sites with an average phase angle of -70 $\pm$ 5°. In addition, I have tested the robustness and re-usability of spiky contact sites. Impedance changes were investigated after an extensive usage (7 experiments with 17 separate insertions, in total) by repeating the impedance test after the last experiment. The average impedance magnitude of all contact sites was slightly increased after the last experiment to 1.5 $\pm$ 0.1 MΩ. The impedance phase angles did not change significantly across this time period (-69 $\pm$ 5° after extensive testing). I have also measured the root mean square noise levels for the 32 contact sites. In the spike band (500 – 5000 Hz) the noise level was only 4.63 $\pm$ 0.51 μV_{rms}. Placing the probe onto the brain slice elevated the measured noise level by 10 - 20%.

DOI:10.15774/PPKE.ITK.2020.005

Thesis Ib. ***With the aid of protruding contact sites I have proven quantitatively that the spiky probe provides higher neuronal yield and higher signal amplitude compared to a commercial surface probe. Moreover, I have also shown that the high-density spiky probe is suitable for separating single unit clusters into putative cell types based on a spatio-temporal analysis of their extracellular waveforms oversampled by multiple adjacent contact sites.***

The high-density spiky probe (with inter-contact distance of 25 μm) was compared to a commercially available, laminar surface probe called 'hockey-stick' (in vitro U-type probe, Plexon Inc., Texas, USA). The average single unit yield was 6.6 for spiky probe per position and 3.6 for the hockey-stick surface probe. The average signal amplitude was 139.2 $\pm$ 96.4 μV in the case of spiky probe and 89.08 $\pm$ 30.2 μV for the hockey-stick probe. The maximal measured signal amplitude was only 162.32 μV for the hockey-stick probe, while the spiky probe had a maximal amplitude of 576.79 μV. Consistent with prior studies, larger average spike amplitudes may correspond to closer cells, since extracellular spikes are decreased and flattened over distance [2, 6, 19, 58].
Using the close-packed contact sites of the high-density spiky probe (with 25 μm inter-contact distances) I have illustrated how this probe can spatio-temporally oversample single unit spikes. I have investigated further parameters in the case of two representative single units, namely trough-to-peak time, presence of the initial capacitive peak, features in the autocorrelogram and spatial spread. I clustered the two representative units into putative cell types using these extended, multi-channel level criteria.

- ***Publication related to the I. Thesis group:*** [69].

II. Thesis group: Co-localised, simultaneous intra- and laminar extracellular recordings with corresponding morphology: generation of a ground-truth dataset

Thesis IIa. ***I have created a novel measurement method providing ground-truth data for multi-channel electrophysiology, in vitro. Using this co-localised and simultaneous experimental protocol, both intra- and extracellular data can be acquired reliably from targeted neurons. I have also provided structural information for the ground-truth electrophysiological data by the reconstruction of the full 3D neuronal morphology and corresponding cell-electrode distances in the tissue. From these recordings I have constructed and released an online, open-source library of the recorded cells together with all the physiological and morphological information listed throughout the thesis. The library and the corresponding tabular guide serves as an ever-expanding, constantly updated ground-truth data collection.***

I have described the steps developed for the recording of co-localised and simultaneous intra- and extracellular signals with sub-millisecond accuracy. Extracellular recordings were complemented with a whole-cell patch-clamp recording in the closest vicinity of the silicon probe. Since these *in vitro* experiments were designed under a two-photon microscope system, proper visual monitoring both for the electrode and for cell positions could be achieved. Inclusion criteria for a successful simultaneous measurement were the following three conditions:

DOI:10.15774/PPKE.ITK.2020.005

- I expected detection of at least 100 spike times for each 3-minute recording session to assure reasonable spike count in every data file (1).
- Holding current injected for maintaining stable spiking had to remain constant throughout each recording session and within a physiological range, ideally below 300 pA (2).
- After pre-processing, spikes of the patch-clamped cell should be detectable on at least one extracellular channel in the spike-triggered average form (3).

Additionally, I have also performed a Ramp-test in the beginning of each whole-cell patch-clamp recording to characterise putative cell types and to determine various useful intracellular parameters of the patched cell.
In addition to electrophysiology, concurrent two-photon imaging was included in the experimental protocol to take full advantage of the available multi-modal set-up. The field-of-view of the two-photon z-stack projection was set to cover both the track of the silicon probe and main cellular compartments (soma, apical trunk region, proximal apical and basal dendrites). Depth levels (z- dimension) typically ranged from -200 μm to 0 μm, (which is the surface of the slices). The resolution of the z-stack (or the step between stacks) was 2-3 μm, which was enough to capture small dendritic processes along the 3D morphology. In the end of the experimental protocol, patch pipette was carefully withdrawn, slice was removed from the dual perfusion chamber and fixated in paraformaldehyde solution for *post-hoc* histological reconstruction. Patch-clamped cells were passively filled with fluorescent markers (Alexa594 and Fluo-4) and with histological tracer molecule (Neurobiotin) via diffusion of the intracellular solution. In cases where all histological steps (fixation, reslicing, and the precipitation of Neurobiotin) were successful, neurons were chosen to be digitally reconstructed in 3D by the Neurolucida system. With the help of 3D reconstructions, Euclidean cell-electrode distances between contact sites and sub-cellular compartments could be calculated properly.
At the time of submission, a total of #16 neurons were successfully recorded from #12 animals by using the simultaneous and co-localised protocol introduced here in *Thesis IIa* (6.1). This library building is currently in progress and to be updated whenever a new successful, candidate data becomes available.

Thesis IIb. With the aid of my acquired simultaneous electrophysiology dataset, a novel single-cell source localisation method called skCSD (developed in a collaborative study) was firstly tested and validated on real experimental data with reconstructed neuronal morphology.

Having all these structural data together with simultaneous electrophysiology made possible to support model-based single-cell calculations with real experimental validation. This was the first time in literature, when researchers were able to compute single-cell level current source densities (or the transmembrane sources of the extracellularly measured potentials) along a detailed, real neuronal morphology. The observed spatio-temporal dynamics was in accordance with previously estimated patterns, namely that somatic currents mostly dominate the process of spike generation and they are balanced by corresponding counter currents along the proximal dendritic tree. This example demonstrated the feasibility of the skCSD method on recorded experimental data and may help in planning further experiments (as an iterative '*experiment-data analysis cycle*'), aiming to reveal the spatial distribution and temporal dynamics of the synaptic input currents which evoke the firing of a neuron.

- ***Publication related to the II. Thesis group:*** [62].

DOI:10.15774/PPKE.ITK.2020.005

III. Thesis group: Combination of multi-channel extracellular recordings and two-photon laser scanning microscopy imaging for the experimental characterisation of photoelectric artefacts

Thesis IIIa. ***I have designed and carried out experiments for acquiring both laser artefact-free and laser contaminated data in one experimental session. My generated dataset is suitable for the characterisation of generated photoelectric artefacts and for the comprehensive evaluation of any artefact suppression algorithm.***

Firstly, I have proved experimentally, that the generated photoelectric artefact is not identical with a simple scanner noise and it has a varying nature across multiple contact sites. Moreover, I have carried simultaneous two-photon imaging and extracellular silicon probe recordings in the same field-of-view. Two-photon excitation was set to be sufficient for detecting reliable transgenic Ca_{2+} signals without causing damage on the metal-based extracellular probe. With the aid of this experiment, multi-cellular Ca_{2+} signals and co-localised extracellularly detected units become comparable.

Thesis IIIb. ***I have shown that single unit clusters can be detectable even under contaminated signal conditions, as well as clustered spikes before-, under- and after laser scanning remained tractable based on their signal amplitudes, waveforms and autocorrelograms.***

Spike sorted single unit activities remained tractable before and after the laser scanning period after applying an iterative artefact filtering process (which algorithm was developed in collaboration with other colleagues). However, I also pointed out that in a few cases photoelectric artefact (due to laser scanning) may have some effects on the dynamics of scanned cells (e.g. indirect excitation mediated by photoelectric currents).

- ***Publication related to the III. Thesis group:*** [**170**].

DOI:10.15774/PPKE.ITK.2020.005

6.2 Application of results and future perspectives

Open questions and opportunities regarding each Thesis group were detailed in corresponding Section 5. All the three experimental problems I have addressed throughout the dissertation are very application oriented, even if their current stages of realisation are different.

Firstly, I have presented and tested penetrating a silicon-based multi-channel spiky probe. While the current shank design proved a significant improvement for *in vitro* recordings, it is certainly not designed for long-term recordings. Future developments may enable such devices to be further designed in both chronic and acute *in vivo* applications via smaller modifications. Another possible future application would be the investigation of different tissue samples using the same probes, e.g. post-operative human *in vitro* tissue samples. Dimensions of the spiky probes are variable in a wide range, and the longest spiky version (equipped with the largest inter-contact distances of 100 μm) would cover a sufficiently large area to be applicable for human neocortical slices and for multi-layered structures.

Regarding the second Thesis group, multiple potential collaborators indicated their interest in using my dataset containing co-localised and simultaneous intra- and extracellular recordings with corresponding morphology. However, as I have mentioned before, some of the intracellularly patch-clamped cells were not visible immediately on the raw extracellular signal, thus they prevented the application of blind spike sorting on the extracellular single unit activities. In these cases, the calculation of spike triggered averages was the only way for comparing intra- and extracellular signals. As a possible continuation of this study, my goal will be to get even closer to the cells with the silicon probes by further optimizing the measurement set-up and process and as a consequence, to record more cells with sortable spike amplitudes. I will also focus on recording more interneurons to expand the usability of the ground-truth dataset. The simultaneous experimental protocol can also be applied on different regions, such as neocortex or human post-operative slices. The first collaborative application of the dataset has already occurred within the framework of the theses. We have shown how the series of extracellular recordings in combination with neuronal morphology can be used to estimate current source densities located on the cell contributing to the recorded extracellular potential. Unlike simple somatic patch-clamp recordings, here we are able to obtain intracellular information along the whole cellular morphology, not just at a single point. This new approach may move the field a bit forward by opening a new experimental window into information processing by single cells allowing for their global monitoring, which was not possible previously. It will be equally important from the theoretical side, as theoretical paradigms are informed by what we are able to extract from available measurements. Since it is now feasible experimentally to obtain the relevant data with the aid of my developed protocol, I believe that the data proposed here may find its uses in future works to constrain the biophysical properties of the neuron membrane, as well as guide new discoveries by giving a coherent view of the global synaptic bombardment and return currents within a targeted neuron.

DOI:10.15774/PPKE.ITK.2020.005

Lastly, I have proposed an experimental solution for the investigation and elimination of photoelectric artefacts in co-localised two-photon imaging and extracellular silicon probe recordings. This study showed that it is possible to get insight into the extracellular activity even under two-photon laser scanning. However, I have found putative modulations in spiking behaviour caused by the photoelectric artefact which were undesirable consequences of simultaneous scanning. Further investigations are to be performed to resolve the indirect stimulation effect of laser generated artefacts. Regarding the application of the filtering algorithm, it would be beneficial to develop an automated and more robust software which is independent of the type of silicon probe used and can be applied to other layouts or different channel counts. The greatest challenge would be to search for correlations and causal roles between co-localised fluorescently active (or 'blinking') cells and extracellularly detected single unit spikes. Similarly to the second Thesis group, the application of simultaneous, multi-modal measurements may give rise to novel findings in designing improved neural interfaces.

DOI:10.15774/PPKE.ITK.2020.005

Chapter 7

References

7.1 Author's publications related to the theses

Peer-reviewed journal publications

- D. Meszéna, B. P Kerekes, I. Pál, G. Orbán, R. Fiáth, T. Holzhammer, P. Ruther, I. Ulbert and G. Márton. A silicon-based spiky probe providing improved cell accessibility for in vitro brain slice recordings. ***SENSORS & ACTUATORS B – CHEM***, 297C, 126649, 2019. (IF: 6.39, Q1/D1) DOI: 10.1016/j.snb.2019.126649 [69]

- G. Orbán, D. Meszéna, K. R. Tasnády, I. Ulbert and G. Márton. Method for spike detection from microelectrode array recordings contaminated by artifacts of simultaneous two-photon imaging. ***PLOS ONE***, 14(8): e0221510, 2019. (IF: 2.78, Q1) DOI: 10.1371/journal.pone.0221510 [170]

- D. Cserpán, D. Meszéna, L. Wittner, K. Tóth, I. Ulbert, Z. Somogyvári and D. Wójcik. Revealing the distribution of transmembrane currents along the dendritic tree of a neuron with known morphology from extracellular recordings. ***eLIFE***, 6:e29384, 2017. (IF: 7.73, Q1/D1) DOI: 10.7554/eLife.29384 [62]

7.2 Other publications of the author

Preprints and works in progress

- R. Fiáth, D. Meszéna, M. Boda, P. Barthó, P. Ruther and I. Ulbert. Recording site placement on planar silicon-based probes affects neural signal quality: edge sites enhance acute recording performance. ***SCIENTIFIC REPORTS***, 2020. (IF: 4.01, Q1/D1) (*Under review*) (Preprint on ***BioRxiv***) DOI: 10.1101/2020.06.01.127308

- G. Dimitriadis, J. P. Neto, A. Aarts, [...] G. Marton, D. Meszéna, S. Mitra, [...] B. Raducanu, P. Ruther, T. Schroeder, W. Singer, P. Tiesinga, I. Ulbert, S. Wang, M. Welkenhuysen, A. R Kampff. Why not record from every channel with a CMOS scanning probe? ***PNAS***, 2020. (IF: 9.58, Q1/D1) (*Under review*) (Preprint on ***BioRxiv***) DOI: 10.1101/275818 [81]

- T. Marek, G. Orbán, D. Meszéna, G. Márton, I. Ulbert, G. Mészáros and Zs. Keresztes. Optimization Aspects of Electrodeposition of Photoluminescent Conductive Polymer Layer onto Neural Microelectrode Arrays. ***MATERIALS CHEMISTRY AND PHYSICS***, 2020. (IF: 2.78, Q2) (*Under review*)

DOI:10.15774/PPKE.ITK.2020.005

Peer-reviewed journal publications

- G. Márton, E. Z. Tóth, L. Wittner, R. Fiáth, D.Pinke, G. Orbán, D. Meszéna, I. Pál, E. L. Győri, Z. Bereczki, Á. Kandrács, K. T. Hofer, A. Pongrácz, I. Ulbert and K. Tóth. The neural tissue around SU-8 implants: a quantitative *in vivo* biocompatibility study. ***MATERIALS SCIENCE & ENGINEERING C***, 112C, 110870, 2020. (IF: 4.96, Q1/D1) DOI: 10.1016/j.snb.2019.126649 [101]

- A. Zátonyi, G. Orbán, R. Modi, G. Márton, D. Meszéna, I. Ulbert, A. Pongrácz, M. Ecker, W. E. Voit, A. Joshi-Imre, and Z. Fekete. A softening laminar electrode for recording single unit activity from the rat hippocampus. ***SCIENTIFIC REPORTS***, vol. 9, no. 1, p. 2321, 2019. (IF: 4.12, Q1/D1) DOI: 10.1038/s41598-019-39835-6 [104]

Patent

- I. Ulbert, G. Márton, D. Meszéna, B.P. Kerekes, G. Orbán, K.R. Tasnády, D. Pinke. A design of an ionic conductance-based multielectrode system for mitigating photoelectric artefacts. Hungarian Patent Application (pending), *Registration number: 45B01FEF1C, File number: P 17 00527, Date: 15th December 2017.*

Selected talks and posters

- D. Meszéna, G. Orbán, K. R. Tasnády, I. Ulbert and G. Márton. Towards co-localised microelectrode array recordings and two-photon microscopy. *HunDoc 2020*, Szeged, Hungary, 2020. (Invited talk)

- Z. Somogyvári, D. Meszéna, D. Cserpán, L. Wittner and I. Ulbert. Spatio-temporal membrane potential and resistive current reconstruction from parallel multielectrode array and intracellular measurements in single neurons. 10^{th} *IBRO World Congress of Neuroscience*, Daegu, Korea, 2019. (Poster)

- G. Orbán, D. Meszéna, K. R. Tasnády, I. Ulbert and G. Márton. Towards simultaneous microelectrode array recordings and two-photon microscopy. *XVI Meeting of the Portuguese Society for Neuroscience*, Lisbon, Portugal, 2019. (Poster)

- R. Fiáth, D. Meszéna, I. Ulbert. Impact of the recording site location on the recording performance of silicon probes in acute experiments. *FENS Regional Meeting*, Belgrade, Serbia, 2019. (Poster)

- E. Z. Tóth, D. Meszéna, A Dublecz, D.Pálfi, K. Tóth, L. Erőss, A. Bagó, D. Fabó, I. Ulbert and L. Wittner. Back-propagating action potentials in human neocortical pyramidal cells and interneurons: A preliminary study. *Gordon Research Conference: Dendrites*, Ventura, CA, US, 2019. (Poster)

- D. Meszéna, I. Pál, B. P. Kerekes, G. Marton, K. Tóth, L. Wittner, Z. Somogyvári and I Ulbert. Simultaneous intra- and linear extracellular recordings with corresponding morphology: towards a ground-truth data for multichannel electrodes. *SfN Neuroscience 2018*, San Diego, CA, US 2018. (Poster)

- K. Tóth, E. Z. Tóth, L. Wittner, R. Fiáth, D. Meszéna, I. Pál, E. L. Győri, D. Pinke, Z. Bereczki, G. Orbán, A. Pongrácz, I. Ulbert and G. Márton. Biocompatibility of the SU-8 in the central nervous system. *SfN Neuroscience 2018*, San Diego, CA, US 2018. (Poster)

- G. Orbán, T. Marek, D. Meszéna, B. P. Kerekes, K. R. Tasnády, I. Ulbert, G. Mészáros, Zs. Keresztes, G. Márton. Fluorescent conductive polymer coating on implanted microelectrodes for visualization under two-photon microscopes. 11^{th} *FENS Forum of Neuroscience*, Berlin, Germany, 2018. (Poster)

- D. Meszéna, B. P. Kerekes, I. Pál, T. Holzhammer, P. Ruther, I. Ulbert and G. Márton. A novel, silicon-based spiky probe providing improved cell accessibility for in vitro brain slice recordings. *Gordon Research Conference: Neuroelectronic Interfaces*, Galveston, Texas, US, 2018. (Poster)

DOI:10.15774/PPKE.ITK.2020.005

- D. Cserpán, D. Meszéna, L. Wittner, K. Tóth, I. Ulbert, Z. Somogyvári and D. Wójcik. Revealing the Distribution of Transmembrane Currents along the Dendritic Tree of a Neuron with Known Morphology from Extracellular Recordings. 2^{nd} *Nencki Symposium*, Warsaw, Poland, 2017. (Poster)

- D. Meszéna, I. Pál, B. P. Kerekes, G. Márton, Z. Somogyvári and I. Ulbert. Integrative experimental design for simultaneous electrophysiology and two-photon calcium imaging in the rat hippocampus, in vitro, 10^{th} *FENS Forum of Neuroscience*, Copenhagen, Denmark, 2016. (Poster)

- I Pál, KT. Hofer, B. P. Kerekes, K. Tóth, B. Rózsa, D. Meszéna and I. Ulbert. Modulation of interictal-like and spontaneous population activity by microsurgical intervention in rat brain slices, 10^{th} *Forum of Neuroscience*, Copenhagen, Denmark, 2016. (Poster)

- D. Meszéna and I. Ulbert. Simultaneously recorded multimodal signals in the hippocampal CA1 region, in vitro. *EMBO Practical Course in Advanced Optical Microscopy*, Marine Biological Association, Plymouth, United Kingdom, 2016. (Poster)

- D. Meszéna and I. Ulbert. Parameter estimation and validation of the single-cell CSD method using simultaneous electrode recordings and two-photon microscopy, 3^{rd} *Baltic-Nordic Summer School on Neuroinformatics*, Tartu, Estonia, 2015. (Poster)

- D. Meszéna, E. Lakatos, G. Szederkényi. Sensitivity analysis and parameter estimation of a human blood glucose regulatory system model. In.: Proceedings of the 11^{th} *International Workshop on Computational Systems Biology*, TISCP 64, pp. 28, Lisbon, Portugal, 2014. (Talk)

- E. Lakatos, D. Meszéna, G. Szederkényi. Identifiability analysis and improved parameter estimation of a human blood glucose control system model. ***LECTURE NOTES IN COMPUTER SCIENCE***, A. Gupta and T.A. Henzinger (Eds.): CMSB 2013, LNBI 8130 Springer, pp. 248-249, 2013. (Talk) (IF: 1.12, Q2), DOI: 10.1007/978-3-642-40708-6

- L. Négyessy, J. Minich, D. Meszéna, A. Buzás, B. Jákli, M. Bányai, E. Procyk, P. Barone, F. Bazsó. From Neuronal Communication to the Flow of Information in the Cerebral Cortex. 11^{th} *Digital Speech and Image Processing*, Kovacica, Serbia, 2012. (Talk)

In Annual Proceedings of the PPCU FITB Doctoral School

- D. Meszéna. Towards a better understanding of intra- and extracellular neural signals and their relationships. *in PhD Proceedings Annual Issues of the Doctoral School, Faculty of Information Technology and Bionics, Pázmány Péter Catholic University* – 2017. G. Prószéky, P. Szolgay Eds. Budapest: Pázmány University ePress, 2017, pp 27–27.

- D. Meszéna. Targeted simultaneous recordings on rat hippocampal CA1 cells, in vitro. *in PhD Proceedings Annual Issues of the Doctoral School, Faculty of Information Technology and Bionics, Pázmány Péter Catholic University* – 2016. G. Prószéky, P. Szolgay Eds. Budapest: Pázmány University ePress, 2016, pp 69–71.

- D. Meszéna. Using two-photon imaging combined with simultaneous recordings to validate CSD analysis. *in PhD Proceedings Annual Issues of the Doctoral School, Faculty of Information Technology and Bionics, Pázmány Péter Catholic University* – 2015. G. Prószéky, P. Szolgay Eds. Budapest: Pázmány University ePress, 2015, pp 81–84.

DOI:10.15774/PPKE.ITK.2020.005

List of Figures

DOI:10.15774/PPKE.ITK.2020.005

DOI:10.15774/PPKE.ITK.2020.005

DOI:10.15774/PPKE.ITK.2020.005

DOI:10.15774/PPKE.ITK.2020.005

List of Tables

DOI:10.15774/PPKE.ITK.2020.005

Bibliography

[1] György Buzsáki. **Large-scale recording of neuronal ensembles.** *Nature neuroscience*, **7**(5):446, 2004. 2, 12, 100

[2] György Buzsáki, Costas A Anastassiou, and Christof Koch. **The origin of extracellular fields and currents-EEG, ECoG, LFP and spikes.** *Nature reviews neuroscience*, **13**(6):407, 2012. 2, 3, 12, 13, 14, 25, 54, 92, 100

[3] Darrell A Henze, Zsolt Borhegyi, Jozsef Csicsvari, Akira Mamiya, Kenneth D Harris, and Gyorgy Buzsaki. **Intracellular features predicted by extracellular recordings in the hippocampus in vivo.** *Journal of neurophysiology*, **84**(1):390–400, 2000. 3, 18, 19, 20, 28, 30, 100

[4] Kimberly M Scott, Jiangang Du, Henry A Lester, and Sotiris C Masmanidis. **Variability of acute extracellular action potential measurements with multisite silicon probes.** *Journal of neuroscience methods*, **211**(1):22–30, 2012. 3, 48

[5] Zoltán Somogyvári, Dorottya Cserpán, István Ulbert, and Péter Érdi. **Localization of single-cell current sources based on extracellular potential patterns: the spike CSD method.** *European Journal of neuroscience*, **36**(10):3299–3313, 2012. 3, 12, 17, 19, 89

[6] Gaute T Einevoll, Christoph Kayser, Nikos K Logothetis, and Stefano Panzeri. **Modelling and analysis of local field potentials for studying the function of cortical circuits.** *Nature reviews neuroscience*, **14**(11):770, 2013. 3, 12, 13, 25, 54, 92

[7] Yoshinao Kajikawa and Charles E Schroeder. **How local is the local field potential?** *Neuron*, **72**(5):847–858, 2011. 3, 13, 25

[8] Klas H Pettersen, Anna Devor, Istvan Ulbert, Anders M Dale, and Gaute T Einevoll. **Current-source density estimation based on inversion of electrostatic forward solution: effects of finite extent of neuronal activity and conductivity discontinuities.** *Journal of neuroscience methods*, **154**(1-2):116–133, 2006. 3, 14, 17

[9] Klas H Pettersen and Gaute T Einevoll. **Amplitude variability and extracellular low-pass filtering of neuronal spikes.** *Biophysical journal*, **94**(3):784–802, 2008. 3, 14

[10] Klas H Pettersen, Henrik Lindén, Anders M Dale, and Gaute T Einevoll. **Extracellular spikes and CSD.** *Handbook of neural activity measurement*, **1**:92–135, 2012. 3, 12, 13, 17

[11] Richárd Fiáth, Bogdan Cristian Raducanu, Silke Musa, Alexandru Andrei, Carolina Mora Lopez, Chris van Hoof, Patrick Ruther, Arno Aarts, Domonkos Horváth, and István Ulbert. **A silicon-based neural probe with densely-packed low-impedance titanium nitride microelectrodes for ultrahigh-resolution in vivo recordings.** *Biosensors and bioelectronics*, **106**:86–92, 2018. 3, 19, 20

DOI:10.15774/PPKE.ITK.2020.005

[12] Joana Pereira Neto, Pedro Baião, Gonçalo Lopes, João Frazão, Joana Nogueira, Elvira Fortunato, Pedro Barquinha, and Adam Raymond Kampff. **Does impedance matter when recording spikes with polytrodes?** *Frontiers in neuroscience*, **12**:715, 2018. 3, 20, 48

[13] László Grand, Lucia Wittner, Stanislav Herwik, Emmanuelle Göthelid, Patrick Ruther, Sven Oscarsson, Hercules Neves, Balázs Dombovári, Richárd Csercsa, György Karmos, et al. **Short and long term biocompatibility of NeuroProbes silicon probes.** *Journal of neuroscience methods*, **189**(2):216–229, 2010. 3, 26

[14] Zsófia Bérces, Kinga Tóth, Gergely Márton, Ildikó Pál, Bálint Kováts-Megyesi, Zoltán Fekete, István Ulbert, and Anita Pongrácz. **Neurobiochemical changes in the vicinity of a nanostructured neural implant.** *Scientific reports*, **6**:35944, 2016. 3

[15] Takashi DY Kozai, Andrea S Jaquins-Gerstl, Alberto L Vazquez, Adrian C Michael, and X Tracy Cui. **Brain tissue responses to neural implants impact signal sensitivity and intervention strategies.** *ACS chemical neuroscience*, **6**(1):48–67, 2015. 3, 22, 26

[16] Steven M Wellman and Takashi DY Kozai. **Understanding the inflammatory tissue reaction to brain implants to improve neurochemical sensing performance**, 2017. 3, 26

[17] Norbert Hajos, Tommas J Ellender, Rita Zemankovics, Edward O Mann, Richard Exley, Stephanie J Cragg, Tamás F Freund, and Ole Paulsen. **Maintaining network activity in submerged hippocampal slices: importance of oxygen supply.** *European journal of neuroscience*, **29**(2):319–327, 2009. 3, 36, 52

[18] Amir Segev, Francisco Garcia-Oscos, and Saïd Kourrich. **Whole-cell Patch-clamp Recordings in Brain Slices.** *JoVE (Journal of visualized experiments)*, **112**:e54024, 2016. 3, 52

[19] Marie Engelene J Obien, Kosmas Deligkaris, Torsten Bullmann, Douglas J Bakkum, and Urs Frey. **Revealing neuronal function through microelectrode array recordings.** *Frontiers in neuroscience*, **8**:423, 2015. 3, 20, 27, 48, 54, 92

[20] Woodrow L Shew, Timothy Bellay, and Dietmar Plenz. **Simultaneous multi-electrode array recording and two-photon calcium imaging of neural activity.** *Journal of neuroscience methods*, **192**(1):75–82, 2010. 3, 78

[21] André Marques-Smith, Joana Pereira Neto, Goncalo Lopes, Joana Nogueira, Lorenza Calcaterra, João Frazão, Danbee Kim, Matthew G Phillips, George Dimitriadis, and Adam Kampff. **Recording from the same neuron with high-density CMOS probes and patch-clamp: a ground-truth dataset and an experiment in collaboration.** *BioRxiv*, page 370080, 2018. 3, 29, 30, 87, 89

[22] Brian D Allen, Caroline Moore-Kochlacs, Jacob G Bernstein, Justin P Kinney, Jorg Scholvin, Luís F Seoane, Chris Chronopoulos, Charlie Lamantia, Suhasa B Kodandaramaiah, Max Tegmark, et al. **Automated in vivo patch-clamp evaluation of extracellular multielectrode array spike recording capability.** *Journal of neurophysiology*, **120**(5):2182–2200, 2018. 3, 29, 30, 63, 87, 89

[23] Santiago Ramón y Cajal. **Histologie du systéme nerveux de l'homme and des vertébrés.** *Maloine (Paris)*, **2**:891–942, 1911. 6, 7, 100

DOI:10.15774/PPKE.ITK.2020.005

[24] Frederico AC Azevedo, Ludmila RB Carvalho, Lea T Grinberg, José Marcelo Farfel, Renata EL Ferretti, Renata EP Leite, Wilson Jacob Filho, Roberto Lent, and Suzana Herculano-Houzel. **Equal numbers of neuronal and nonneuronal cells make the human brain an isometrically scaled-up primate brain.** *Journal of comparative neurology*, **513**(5):532–541, 2009. 6

[25] György Buzsáki. **Two-stage model of memory trace formation: a role for "noisy" brain states.** *Neuroscience*, **31**(3):551–570, 1989. 7

[26] Tamas F Freund and Gyorgy Buzsaki. **Interneurons of the hippocampus.** *Hippocampus*, **6**(4):347–470, 1996. 8

[27] Thomas Klausberger and Peter Somogyi. **Neuronal diversity and temporal dynamics: the unity of hippocampal circuit operations.** *Science*, **321**(5885):53–57, 2008. 8

[28] P Somogyi et al. **A specific 'axo-axonal'interneuron in the visual cortex of the rat.** *Brain res*, **136**(2):345–350, 1977. 8

[29] Eszter Boldog, Trygve E Bakken, Rebecca D Hodge, Mark Novotny, Brian D Aevermann, Judith Baka, Sándor Bordé, Jennie L Close, Francisco Diez-Fuertes, Song-Lin Ding, et al. **Transcriptomic and morphophysiological evidence for a specialized human cortical GABAergic cell type.** *Nature neuroscience*, **21**(9):1185–1195, 2018. 8

[30] János Szentágothai. **The modular architectonic principle of neural centers.** *Reviews of physiology, biochemistry and pharmacology*, **98**:11–61, 1983. 9, 100

[31] Bart Ellenbroek and Jiun Youn. **Rodent models in neuroscience research: is it a rat race?** *Disease Models & Mechanisms*, **9**(10):1079–1087, 2016. 10, 100

[32] Alan L Hodgkin and Andrew F Huxley. **A quantitative description of membrane current and its application to conduction and excitation in nerve.** *The journal of physiology*, **117**(4):500–544, 1952. 11, 14

[33] Greg J Stuart and Bert Sakmann. **Active propagation of somatic action potentials into neocortical pyramidal cell dendrites.** *Nature*, **367**(6458):69, 1994. 12

[34] György Buzsáki and Adam Kandel. **Somadendritic backpropagation of action potentials in cortical pyramidal cells of the awake rat.** *Journal of neurophysiology*, **79**(3):1587–1591, 1998. 12, 13

[35] Rafael de NO LORENTE. **Analysis of the distribution of the action currents of nerve in volume conductors.** *Studies from the Rockefeller institute for medical research. Reprints. Rockefeller Institute for Medical Research*, **132**:384–477, 1947. 12

[36] WH Freygang and K Frank. **Extracellular potentials from single spinal motoneurons.** *The journal of general physiology*, **42**(4):749–760, 1959. 12, 28, 30

[37] Alessio Paolo Buccino, Miroslav Kuchta, Karoline Horgmo Jaeger, Torbjorn Vefferstad Ness, Pierre Berthet, Kent-Andre Mardal, Gert Cauwenberghs, and Aslak Tveito. **How does the presence of neural probes affect extracellular potentials?** *Journal of neural engineering*, **16**(2):026030, 2019. 12

[38] Henrik Lindén, Tom Tetzlaff, Tobias C Potjans, Klas H Pettersen, Sonja Grün, Markus Diesmann, and Gaute T Einevoll. **Modeling the spatial reach of the LFP.** *Neuron*, **72**(5):859–872, 2011. 13

DOI:10.15774/PPKE.ITK.2020.005

[39] Anita Kamondi, Laszlo Acsady, and György Buzsáki. **Dendritic spikes are enhanced by cooperative network activity in the intact hippocampus.** *Journal of neuroscience*, **18**(10):3919–3928, 1998. 13

[40] Carl Gold, Darrell A Henze, Christof Koch, and György Buzsáki. **On the origin of the extracellular action potential waveform: a modeling study.** *Journal of neurophysiology*, **95**(5):3113–3128, 2006. 14

[41] Carl Gold, Darrell A Henze, and Christof Koch. **Using extracellular action potential recordings to constrain compartmental models.** *Journal of computational neuroscience*, **23**(1):39–58, 2007. 14, 15

[42] Henrik Lindén, Klas H Pettersen, and Gaute T Einevoll. **Intrinsic dendritic filtering gives low-pass power spectra of local field potentials.** *Journal of computational neuroscience*, **29**(3):423–444, 2010. 14

[43] Isabel Delgado Ruz and Simon R Schultz. **Localising and classifying neurons from high density MEA recordings.** *Journal of neuroscience methods*, **233**:115–128, 2014. 14

[44] Charles Nicholson and John A Freeman. **Theory of current source-density analysis and determination of conductivity tensor for anuran cerebellum.** *Journal of neurophysiology*, **38**(2):356–368, 1975. 14, 17

[45] Ulla Mitzdorf. **Current source-density method and application in cat cerebral cortex: investigation of evoked potentials and EEG phenomena.** *Physiological reviews*, **65**(1):37–100, 1985. 14, 17

[46] John Clark and Robert Plonsey. **A mathematical evaluation of the core conductor model.** *Biophysical journal*, **6**(1):95–112, 1966. 14

[47] Wilfrid Rall. **Electrophysiology of a dendritic neuron model.** *Biophysical journal*, **2**(2):145–167, 1962. 14

[48] Wilfrid Rall and Gordon M Shepherd. **Theoretical reconstruction of field potentials and dendrodendritic synaptic interactions in olfactory bulb.** *Journal of neurophysiology*, **31**(6):884–915, 1968. 14

[49] Carles Nicholson and Rodolfo Llinas. **Field potentials in the alligator cerebellum and theory of their relationship to Purkinje cell dendritic spikes.** *Journal of Neurophysiology*, **34**(4):509–531, 1971. 14

[50] Harilal Parasuram, Bipin Nair, Egidio D'Angelo, Michael Hines, Giovanni Naldi, and Shyam Diwakar. **Computational modeling of single neuron extracellular electric potentials and network local field potentials using LFPsim.** *Frontiers in computational neuroscience*, **10**:65, 2016. 14

[51] Henrik Lindén, Espen Hagen, Szymon Leski, Eivind S Norheim, Klas H Pettersen, and Gaute T Einevoll. **LFPy: a tool for biophysical simulation of extracellular potentials generated by detailed model neurons.** *Frontiers in neuroinformatics*, **7**:41, 2014. 14

[52] Espen Hagen, Solveig Naess, Torbjorn V Ness, and Gaute T Einevoll. **Multimodal Modeling of Neural Network Activity: Computing LFP, ECoG, EEG, and MEG Signals With LFPy 2.0.** *Frontiers in neuroinformatics*, **12**, 2018. 14

DOI:10.15774/PPKE.ITK.2020.005

[53] Espen Hagen, Solveig Naess, Torbjorn V Ness, and Gaute T Einevoll. **LFPy: multimodal modeling of extracellular neuronal recordings in Python**. *BioRxiv*, page 620286, 2019. 14

[54] Torbjorn V Ness, Chaitanya Chintaluri, Jan Potworowski, Szymon Leski, Helena Glabska, Daniel K Wojcik, and Gaute T Einevoll. **Modelling and analysis of electrical potentials recorded in microelectrode arrays (MEAs)**. *Neuroinformatics*, **13**(4):403–426, 2015. 15

[55] Nikos K Logothetis, Christoph Kayser, and Axel Oeltermann. **In vivo measurement of cortical impedance spectrum in monkeys: implications for signal propagation**. *Neuron*, **55**(5):809–823, 2007. 16

[56] Claude Bédard and Alain Destexhe. **Generalized theory for current-source-density analysis in brain tissue**. *Physical review E*, **84**(4):041909, 2011. 16

[57] Espen Hagen, David Dahmen, Maria L Stavrinou, Henrik Lindén, Tom Tetzlaff, Sacha J van Albada, Sonja Grün, Markus Diesmann, and Gaute T Einevoll. **Hybrid scheme for modeling local field potentials from point-neuron networks**. *Cerebral cortex*, pages 1–36, 2016. 17

[58] Zoltán Somogyvári, László Zalányi, István Ulbert, and Péter Érdi. **Model-based source localization of extracellular action potentials**. *Journal of neuroscience methods*, **147**(2):126–137, 2005. 17, 54, 57, 89, 92

[59] Szymon Leski, Klas H Pettersen, Beth Tunstall, Gaute T Einevoll, John Gigg, and Daniel K Wójcik. **Inverse current source density method in two dimensions: inferring neural activation from multielectrode recordings**. *Neuroinformatics*, **9**(4):401–425, 2011. 17, 88

[60] Jan Potworowski, Wit Jakuczun, Szymon Leski, and Daniel Wójcik. **Kernel current source density method**. *Neural computation*, **24**(2):541–575, 2012. 17, 88

[61] Daniel K Wójcik. **Current source density (CSD) analysis**. *Encyclopedia of computational neuroscience*, pages 915–922, 2015. 17

[62] Dorottya Cserpán, Domokos Meszéna, Lucia Wittner, Kinga Tóth, István Ulbert, Zoltán Somogyvári, and Daniel K Wójcik. **Revealing the distribution of transmembrane currents along the dendritic tree of a neuron from extracellular recordings**. *eLife*, **6**:e29384, 2017. 17, 18, 72, 93, 97

[63] Erik W Schomburg, Costas A Anastassiou, György Buzsáki, and Christof Koch. **The spiking component of oscillatory extracellular potentials in the rat hippocampus**. *Journal of neuroscience*, **32**(34):11798–11811, 2012. 18

[64] Douglas J Bakkum, Urs Frey, Milos Radivojevic, Thomas L Russell, Jan Müller, Michele Fiscella, Hirokazu Takahashi, and Andreas Hierlemann. **Tracking axonal action potential propagation on a high-density microelectrode array across hundreds of sites**. *Nature communications*, **4**:2181, 2013. 19

[65] Jozsef Csicsvari, Hajime Hirase, András Czurkó, Akira Mamiya, and György Buzsáki. **Oscillatory coupling of hippocampal pyramidal cells and interneurons in the behaving rat**. *Journal of neuroscience*, **19**(1):274–287, 1999. 19, 56, 57

DOI:10.15774/PPKE.ITK.2020.005

[66] Peter Barthó, Hajime Hirase, Lenaic Monconduit, Michael Zugaro, Kenneth D Harris, and György Buzsáki. **Characterization of neocortical principal cells and interneurons by network interactions and extracellular features**. *Journal of neurophysiology*, **92**(1):600–608, 2004. 19, 41, 56, 57

[67] Hernan Gonzalo Rey, Carlos Pedreira, and Rodrigo Quian Quiroga. **Past, present and future of spike sorting techniques**. *Brain research bulletin*, **119**:106–117, 2015. 19

[68] Xiaoxuan Jia, Joshua H. Siegle, Corbett Bennett, Samuel D. Gale, Daniel J. Denman, Christof Koch, and Shawn R. Olsen. **High-density extracellular probes reveal dendritic backpropagation and facilitate neuron classification**. *Journal of neurophysiology*, **121**(5):1831–1847, 2019. 19

[69] Domokos Meszéna, Bálint Péter Kerekes, Ildikó Pál, Gábor Orbán, Richárd Fiáth, Tobias Holzhammer, Patrick Ruther, István Ulbert, and Gergely Márton. **A silicon-based spiky probe providing improved cell accessibility during in vitro slice recordings**. *Sensors and actuators B: Chemical*, **297**:126649, 2019. 19, 92, 97

[70] Patrick Ruther and Oliver Paul. **New approaches for CMOS-based devices for large-scale neural recording**. *Current opinion in neurobiology*, **32**:31–37, 2015. 20

[71] John P Seymour, Fan Wu, Kensall D Wise, and Euisik Yoon. **State-of-the-art MEMS and microsystem tools for brain research**. *Microsystems and nanoengineering*, **3**:16066, 2017. 20, 21, 22, 27, 100, 101

[72] David H Hubel. **Tungsten microelectrode for recording from single units**. *Science*, **125**(3247):549–550, 1957. 20

[73] István Ulbert, Eric Halgren, Gary Heit, and George Karmos. **Multiple microelectrode-recording system for human intracortical applications**. *Journal of neuroscience methods*, **106**(1):69–79, 2001. 20, 31, 32

[74] Istvan Ulbert, Gary Heit, Joseph Madsen, George Karmos, and Eric Halgren. **Laminar analysis of human neocortical interictal spike generation and propagation: current source density and multiunit analysis in vivo**. *Epilepsia*, **45**:48–56, 2004. 20, 31, 32

[75] Charles M Gray, Pedro E Maldonado, Mathew Wilson, and Bruce McNaughton. **Tetrodes markedly improve the reliability and yield of multiple single-unit isolation from multi-unit recordings in cat striate cortex**. *Journal of neuroscience methods*, **63**(1-2):43–54, 1995. 20

[76] Kenneth D Harris, Darrell A Henze, Jozsef Csicsvari, Hajime Hirase, and Gyorgy Buzsaki. **Accuracy of tetrode spike separation as determined by simultaneous intracellular and extracellular measurements**. *Journal of neurophysiology*, **84**(1):401–414, 2000. 20

[77] Arash A Fomani and Raafat R Mansour. **Fabrication and characterization of the flexible neural microprobes with improved structural design**. *Sensors and actuators A: Physical*, **168**(2):233–241, 2011. 20

[78] Timothy J Blanche, Martin A Spacek, Jamille F Hetke, and Nicholas V Swindale. **Polytrodes: high-density silicon electrode arrays for large-scale multiunit recording**. *Journal of neurophysiology*, **93**(5):2987–3000, 2005. 20, 51

DOI:10.15774/PPKE.ITK.2020.005

[79] Antal Berényi, Zoltán Somogyvári, Anett J Nagy, Lisa Roux, John D Long, Shigeyoshi Fujisawa, Eran Stark, Anthony Leonardo, Timothy D Harris, and György Buzsáki. **Large-scale, high-density (up to 512 channels) recording of local circuits in behaving animals**. *Journal of neurophysiology*, **111**(5):1132–1149, 2013. 20

[80] Bogdan C Raducanu, Refet F Yazicioglu, Carolina M Lopez, Marco Ballini, Jan Putzeys, Shiwei Wang, Alexandru Andrei, Veronique Rochus, Marleen Welkenhuysen, Nick van Helleputte, et al. **Time multiplexed active neural probe with 1356 parallel recording sites**. *Sensors*, **17**(10):2388, 2017. 20, 21

[81] George Dimitriadis, Joana P Neto, Arno Aarts, Andrei Alexandru, Marco Ballini, Francesco Battaglia, Lorenza Calcaterra, Francois David, Richard Fiath, Joao Frazao, et al. **Why not record from every channel with a CMOS scanning probe?** *BioRxiv*, page 275818, 2018. 20, 97

[82] James J Jun, Nicholas A Steinmetz, Joshua H Siegle, Daniel J Denman, Marius Bauza, Brian Barbarits, Albert K Lee, Costas A Anastassiou, Alexandru Andrei, Cagatay Aydin, et al. **Fully integrated silicon probes for high-density recording of neural activity**. *Nature*, **551**(7679):232, 2017. 20, 21

[83] Jozsef Csicsvari, Darrell A Henze, Brian Jamieson, Kenneth D Harris, Anton Sirota, Péter Barthó, Kensall D Wise, and Gyoörgy Buzsáki. **Massively parallel recording of unit and local field potentials with silicon-based electrodes**. *Journal of neurophysiology*, **90**(2):1314–1323, 2003. 20, 56

[84] László Grand, Anita Pongrácz, Éva Vázsonyi, Gergely Márton, Dorottya Gubán, Richárd Fiáth, Bálint Péter Kerekes, György Karmos, István Ulbert, and Gábor Battistig. **A novel multisite silicon probe for high quality laminar neural recordings**. *Sensors and actuators A: Physical*, **166**(1):14–21, 2011. 20

[85] Karsten Seidl, Michael Schwaerzle, Istvan Ulbert, Herc P Neves, Oliver Paul, and Patrick Ruther. **CMOS-based high-density silicon microprobe arrays for electronic depth control in intracortical neural recording–characterization and application**. *Journal of microelectromechanical systems*, **21**(6):1426–1435, 2012. 20

[86] Jörg Scholvin, Justin P Kinney, Jacob G Bernstein, Caroline Moore-Kochlacs, Nancy Kopell, Clifton G Fonstad, and Edward S Boyden. **Close-packed silicon microelectrodes for scalable spatially oversampled neural recording**. *IEEE Transactions on biomedical engineering*, **63**(1):120–130, 2016. 20, 30

[87] Tom Torfs, Arno Aarts, Mehmet A Erismis, Junaid Aslam, Refet Firat Yazicioglu, Karsten Seidl, Stanislav Herwik, Istvan Ulbert, Balázs Dombovari, Richárd Fiáth, et al. **Two-dimensional multi-channel neural probes with electronic depth control**. *IEEE transactions on biomedical circuits and systems*, **5**(5):403–412, 2011. 20

[88] Abdalrahman Sayed Herbawi, Olaf Christ, Lukas Kiessner, Soheil Mottaghi, Ulrich G Hofmann, Oliver Paul, and Patrick Ruther. **CMOS Neural Probe With 1600 Close-Packed Recording Sites and 32 Analog Output Channels**. *Journal of microelectromechanical Systems*, **27**(6):1023–1034, 2018. 20

[89] Mohamad HajjHassan, Vamsy Chodavarapu, and Sam Musallam. **NeuroMEMS: neural probe microtechnologies**. *Sensors*, **8**(10):6704–6726, 2008. 21

DOI:10.15774/PPKE.ITK.2020.005

[90] Kensall D Wise, David J Anderson, Jamille F Hetke, Daryl R Kipke, and Khalil Najafi. **Wireless implantable microsystems: high-density electronic interfaces to the nervous system**. *Proceedings of the IEEE*, **92**(1):76–97, 2004. 21

[91] Patrick K Campbell, Kelly E Jones, Robert J Huber, Kenneth W Horch, and Richard A Normann. **A silicon-based, three-dimensional neural interface: manufacturing processes for an intracortical electrode array**. *IEEE Transactions on biomedical engineering*, **38**(8):758–768, 1991. 21

[92] Emília Tóth, Dániel Fabó, László Entz, István Ulbert, and Loránd Eröss. **Intracranial neuronal ensemble recordings and analysis in epilepsy**. *Journal of neuroscience methods*, **260**:261–269, 2016. 21, 31, 32

[93] Urs Frey, U Egert, F Heer, S Hafizovic, and Andreas Hierlemann. **Microelectronic system for high-resolution mapping of extracellular electric fields applied to brain slices**. *Biosensors and bioelectronics*, **24**(7):2191–2198, 2009. 22

[94] Luca Berdondini, PD Van Der Wal, Olivier Guenat, Nicolaas F de Rooij, Milena Koudelka-Hep, P Seitz, R Kaufmann, P Metzler, N Blanc, and S Rohr. **High-density electrode array for imaging in vitro electrophysiological activity**. *Biosensors and bioelectronics*, **21**(1):167–174, 2005. 22

[95] A Maccione, A Simi, T Nieus, M Gandolfo, K Imfeld, E Ferrea, E Sernagor, and L Berdondini. **Sensing and actuating electrophysiological activity on brain tissue and neuronal cultures with a high-density CMOS-MEA**. In *2013 Transducers and Eurosensors XXVII: The 17th International Conference on Solid-State Sensors, Actuators and Microsystems (TRANSDUCERS and EUROSENSORS XXVII)*, pages 752–755. IEEE, 2013. 22

[96] David Tsai, Daniel Sawyer, Adrian Bradd, Rafael Yuste, and Kenneth L Shepard. **A very large-scale microelectrode array for cellular-resolution electrophysiology**. *Nature communications*, **8**(1):1802, 2017. 22

[97] Marc Olivier Heuschkel, Michael Fejtl, Mario Raggenbass, Daniel Bertrand, and Philippe Renaud. **A three-dimensional multi-electrode array for multi-site stimulation and recording in acute brain slices**. *Journal of neuroscience methods*, **114**(2):135–148, 2002. 22

[98] Micha E Spira and Aviad Hai. **Multi-electrode array technologies for neuroscience and cardiology**. *Nature nanotechnology*, **8**(2):83, 2013. 22

[99] Ane Altuna, Elisa Bellistri, Elena Cid, Paloma Aivar, Beatriz Gal, Javier Berganzo, Gemma Gabriel, Anton Guimerá, Rosa Villa, Luis J Fernández, et al. **SU-8 based microprobes for simultaneous neural depth recording and drug delivery in the brain**. *Lab on a chip*, **13**(7):1422–1430, 2013. 22

[100] Zoltán Fekete and Anita Pongrácz. **Multifunctional soft implants to monitor and control neural activity in the central and peripheral nervous system: A review**. *Sensors and actuators B: Chemical*, **243**:1214–1223, 2017. 22

[101] Gergely Márton, Estilla Zsófia Tóth, Lucia Wittner, Richárd Fiáth, Domonkos Pinke, Gábor Orbán, Domokos Meszéna, Ildikó Pál, Edit Lelle Györi, Zsófia Bereczki, Ágnes Kandrács, Katharina T. Hofer, Anita Pongrácz, István Ulbert, and Kinga Tóth. **The neural tissue around SU-8 implants: A quantitative in vivo biocompatibility study**. *Materials science and engineering: C*, page 110870, 2020. 22, 98

DOI:10.15774/PPKE.ITK.2020.005

[102] Maria Vomero, Elisa Castagnola, Francesca Ciarpella, Emma Maggiolini, Noah Goshi, Elena Zucchini, Stefano Carli, Luciano Fadiga, Sam Kassegne, and Davide Ricci. **Highly stable glassy carbon interfaces for long-term neural stimulation and low-noise recording of brain activity**. *Scientific reports*, **7**(1):1–14, 2017. 22

[103] Maria Vomero, Elena Zucchini, Emanuela Delfino, Calogero Gueli, Norma Carolina Mondragon, Stefano Carli, Luciano Fadiga, and Thomas Stieglitz. **Glassy carbon electrocorticography electrodes on ultra-thin and finger-like polyimide substrate: Performance evaluation based on different electrode diameters**. *Materials*, **11**(12):2486, 2018. 22

[104] Anita Zátonyi, Gábor Orbán, Romil Modi, Gergely Márton, Domokos Meszéna, István Ulbert, Anita Pongrácz, Melanie Ecker, Walter E Voit, Alexandra Joshi-Imre, and Zoltán Fekete. **A softening laminar electrode for recording single unit activity from the rat hippocampus**. *Scientific reports*, **9**(1):2321, 2019. 22, 27, 98

[105] Shruti Nambiar and John TW Yeow. **Conductive polymer-based sensors for biomedical applications**. *Biosensors and Bioelectronics*, **26**(5):1825–1832, 2011. 22

[106] Subramaniam Venkatraman, Jeffrey Hendricks, Zachary A King, Andrew J Sereno, Sarah Richardson-Burns, David Martin, and Jose M Carmena. **In vitro and in vivo evaluation of PEDOT microelectrodes for neural stimulation and recording**. *IEEE transactions on neural systems and rehabilitation engineering*, **19**(3):307–316, 2011. 22

[107] Patrick J Rousche, David S Pellinen, David P Pivin, Justin C Williams, Rio J Vetter, and Daryl R Kipke. **Flexible polyimide-based intracortical electrode arrays with bioactive capability**. *IEEE Transactions on biomedical engineering*, **48**(3):361–371, 2001. 22

[108] Jong-Mo Seo, Sung June Kim, Hum Chung, Eui Tae Kim, Hyeong Gon Yu, and Young Suk Yu. **Biocompatibility of polyimide microelectrode array for retinal stimulation**. *Materials Science and Engineering: C*, **24**(1-2):185–189, 2004. 22

[109] Winfried Denk, James H Strickler, and Watt W Webb. **Two-photon laser scanning fluorescence microscopy**. *Science*, **248**(4951):73–76, 1990. 23

[110] Karel Svoboda, Winfried Denk, David Kleinfeld, and David W Tank. **In vivo dendritic calcium dynamics in neocortical pyramidal neurons**. *Nature*, **385**(6612):161, 1997. 23

[111] Gergely Katona, Gergely Szalay, Pál Maák, Attila Kaszás, Máté Veress, Dániel Hillier, Balázs Chiovini, E Sylvester Vizi, Botond Roska, and Balázs Rózsa. **Fast two-photon in vivo imaging with three-dimensional random-access scanning in large tissue volumes**. *Nature methods*, **9**(2):201, 2012. 23

[112] José-Angel Conchello and Jeff W Lichtman. **Optical sectioning microscopy**. *Nature methods*, **2**(12):920–931, 2005. 23

[113] Karel Svoboda and Ryohei Yasuda. **Principles of two-photon excitation microscopy and its applications to neuroscience**. *Neuron*, **50**(6):823–839, 2006. 24

[114] Gergely Szalay, Linda Judák, Gergely Katona, Katalin Ócsai, Gábor Juhász, Máté Veress, Zoltán Szadai, András Fehér, Tamás Tompa, Balázs Chiovini, et al. **Fast 3D imaging of spine, dendritic, and neuronal assemblies in behaving animals**. *Neuron*, **92**(4):723–738, 2016. 24

DOI:10.15774/PPKE.ITK.2020.005

[115] Hod Dana, Tsai-Wen Chen, Amy Hu, Brenda C Shields, Caiying Guo, Loren L Looger, Douglas S Kim, and Karel Svoboda. **Thy1-GCaMP6 transgenic mice for neuronal population imaging in vivo**. *PloS one*, **9**(9):e108697, 2014. 24, 35, 79

[116] Michael Z Lin and Mark J Schnitzer. **Genetically encoded indicators of neuronal activity**. *Nature neuroscience*, **19**(9):1142, 2016. 25

[117] Vincent Villette, Mariya Chavarha, Ivan K Dimov, Jonathan Bradley, Lagnajeet Pradhan, Benjamin Mathieu, Stephen W Evans, Simon Chamberland, Dongqing Shi, Renzhi Yang, et al. **Ultrafast two-photon imaging of a high-gain voltage indicator in awake behaving mice**. *Cell*, **179**(7):1590–1608, 2019. 25

[118] Edward S Boyden, Feng Zhang, Ernst Bamberg, Georg Nagel, and Karl Deisseroth. **Millisecond-timescale, genetically targeted optical control of neural activity**. *Nature neuroscience*, **8**(9):1263–1268, 2005. 25

[119] György Buzsáki, Eran Stark, Antal Berényi, Dion Khodagholy, Daryl R Kipke, Euisik Yoon, and Kensall D Wise. **Tools for probing local circuits: high-density silicon probes combined with optogenetics**. *Neuron*, **86**(1):92–105, 2015. 25

[120] Michael Häusser. **Optogenetics: the age of light**. *Nature methods*, **11**(10):1012, 2014. 25

[121] Oscar Herreras. **Local field potentials: myths and misunderstandings**. *Frontiers in neural circuits*, **10**:101, 2016. 25

[122] Kenneth D Harris, Rodrigo Quian Quiroga, Jeremy Freeman, and Spencer L Smith. **Improving data quality in neuronal population recordings**. *Nature neuroscience*, **19**(9):1165, 2016. 25, 27, 28, 63

[123] Nicholas A Steinmetz, Christof Koch, Kenneth D Harris, and Matteo Carandini. **Challenges and opportunities for large-scale electrophysiology with Neuropixels probes**. *Current opinion in neurobiology*, **50**:92–100, 2018. 25

[124] Takashi DY Kozai, James R Eles, Alberto L Vazquez, and X Tracy Cui. **Two-photon imaging of chronically implanted neural electrodes: Sealing methods and new insights**. *Journal of neuroscience methods*, **258**:46–55, 2016. 26

[125] Mehdi Jorfi, John L Skousen, Christoph Weder, and Jeffrey R Capadona. **Progress towards biocompatible intracortical microelectrodes for neural interfacing applications**. *Journal of neural engineering*, **12**(1):011001, 2014. 26, 100

[126] Steven M Wellman, James R Eles, Kip A Ludwig, John P Seymour, Nicholas J Michelson, William E McFadden, Alberto L Vazquez, and Takashi DY Kozai. **A materials roadmap to functional neural interface design**. *Advanced functional materials*, **28**(12):1701269, 2018. 26

[127] Nicholas A Steinmetz, Christina Buetfering, Jerome Lecoq, Christian R Lee, Andrew J Peters, Elina AK Jacobs, Philip Coen, Douglas R Ollerenshaw, Matthew T Valley, Saskia EJ De Vries, et al. **Aberrant cortical activity in multiple GCaMP6-expressing transgenic mouse lines**. *eNeuro*, 2017. 27

[128] Toshio Miyashita, Yu R Shao, Jason Chung, Olivia Pourzia, and Dan Feldman. **Long-term channelrhodopsin-2 (ChR2) expression can induce abnormal axonal morphology and targeting in cerebral cortex**. *Frontiers in neural circuits*, **7**:8, 2013. 27

DOI:10.15774/PPKE.ITK.2020.005

[129] Michael Wehr, John S Pezaris, and Maneesh Sahani. **Simultaneous paired intracellular and tetrode recordings for evaluating the performance of spike sorting algorithms.** *Neurocomputing*, **26**:1061–1068, 1999. 28, 30

[130] Costas A Anastassiou, Rodrigo Perin, György Buzsáki, Henry Markram, and Christof Koch. **Cell type-and activity-dependent extracellular correlates of intracellular spiking.** *Journal of neurophysiology*, **114**(1):608–623, 2015. 29, 30, 89

[131] Felix Franke, Robert Pröpper, Henrik Alle, Philipp Meier, Jörg RP Geiger, Klaus Obermayer, and Matthias HJ Munk. **Spike sorting of synchronous spikes from local neuron ensembles.** *Journal of neurophysiology*, **114**(4):2535–2549, 2015. 29, 30

[132] Felix Franke, Michal Natora, Clemens Boucsein, Matthias HJ Munk, and Klaus Obermayer. **An online spike detection and spike classification algorithm capable of instantaneous resolution of overlapping spikes.** *Journal of computational neuroscience*, **29**(1-2):127–148, 2010. 29

[133] Roni Vardi, Amir Goldental, Shira Sardi, Anton Sheinin, and Ido Kanter. **Simultaneous multi-patch-clamp and extracellular-array recordings: Single neuron reflects network activity.** *Scientific reports*, **6**:36228, 2016. 29, 30

[134] David Jäckel, Douglas J Bakkum, Thomas L Russell, Jan Müller, Milos Radivojevic, Urs Frey, Felix Franke, and Andreas Hierlemann. **Combination of high-density microelectrode array and patch clamp recordings to enable studies of multisynaptic integration.** *Scientific reports*, **7**(1):978, 2017. 29, 30

[135] Pierre Yger, Giulia LB Spampinato, Elric Esposito, Baptiste Lefebvre, Stéphane Deny, Christophe Gardella, Marcel Stimberg, Florian Jetter, Guenther Zeck, Serge Picaud, et al. **A spike sorting toolbox for up to thousands of electrodes validated with ground truth recordings in vitro and in vivo.** *eLife*, **7**:e34518, 2018. 29, 30

[136] Joana P Neto, Goncalo Lopes, João Frazão, Joana Nogueira, Pedro Lacerda, Pedro Baião, Arno Aarts, Alexandru Andrei, Silke Musa, Elvira Fortunato, et al. **Validating silicon polytrodes with paired juxtacellular recordings: method and dataset.** *Journal of neurophysiology*, **116**(2):892–903, 2016. 29, 30, 87, 89

[137] Daniel Fine English, Sam McKenzie, Talfan Evans, Kanghwan Kim, Euisik Yoon, and György Buzsáki. **Pyramidal cell-interneuron circuit architecture and dynamics in hippocampal networks.** *Neuron*, **96**(2):505–520, 2017. 29, 30

[138] David L Hunt, Chongxi Lai, Richard D Smith, Albert K Lee, Timothy D Harris, and Mladen Barbic. **Multimodal in vivo brain electrophysiology with integrated glass microelectrodes.** *Nature biomedical engineering*, page 1, 2019. 29, 30

[139] Ivan Cohen and Richard Miles. **Contributions of intrinsic and synaptic activities to the generation of neuronal discharges in in vitro hippocampus.** *The journal of physiology*, **524**(2):485–502, 2000. 30

[140] Edith Chorev and Michael Brecht. **In vivo dual intra-and extracellular recordings suggest bidirectional coupling between CA1 pyramidal neurons.** *Journal of neurophysiology*, **108**(6):1584–1593, 2012. 30

DOI:10.15774/PPKE.ITK.2020.005

[141] Dániel Fabó, Zsófia Maglóczky, Lucia Wittner, Ágnes Pék, Loránd Erőss, Sandor Czirjak, Janos Vajda, András Sólyom, György Rásonyi, Anna Szűcs, et al. **Properties of in vivo interictal spike generation in the human subiculum**. *Brain*, **131**(2):485–499, 2008. 31

[142] Richárd Csercsa, Balázs Dombovári, Dániel Fabó, Lucia Wittner, Loránd Eröss, László Entz, András Sólyom, György Rásonyi, Anna Szűcs, Anna Kelemen, et al. **Laminar analysis of slow wave activity in humans**. *Brain*, **133**(9):2814–2829, 2010. 31, 32

[143] Jose M Ibarz, Guglielmo Foffani, Elena Cid, Marion Inostroza, and Liset Menendez de la Prida. **Emergent dynamics of fast ripples in the epileptic hippocampus**. *Journal of neuroscience*, **30**(48):16249–16261, 2010. 32

[144] Ivan Fernandez-Lamo, Daniel Gomez-Dominguez, Alberto Sanchez-Aguilera, Azahara Oliva, Aixa Victoria Morales, Manuel Valero, Elena Cid, Antal Berenyi, and Liset Menendez de la Prida. **Proximodistal organization of the CA2 hippocampal area**. *Cell reports*, **26**(7):1734–1746, 2019. 32

[145] Lucia Wittner, Gilles Huberfeld, Stéphane Clémenceau, Loránd Eröss, Edouard Dezamis, László Entz, István Ulbert, Michel Baulac, Tamás F Freund, Zsófia Maglóczky, et al. **The epileptic human hippocampal cornu ammonis 2 region generates spontaneous interictal-like activity in vitro**. *Brain*, **132**(11):3032–3046, 2009. 35

[146] Bálint Péter Kerekes, Kinga Tóth, Attila Kaszás, Balázs Chiovini, Zoltán Szadai, Gergely Szalay, Dénes Pálfi, Attila Bagó, Klaudia Spitzer, Balázs Rózsa, et al. **Combined two-photon imaging, electrophysiological, and anatomical investigation of the human neocortex in vitro**. *Neurophotonics*, **1**(1):011013, 2014. 35, 36, 43, 44

[147] Jonathan T Ting, Tanya L Daigle, Qian Chen, and Guoping Feng. **Acute brain slice methods for adult and aging animals: application of targeted patch clamp analysis and optogenetics**. In *Patch-clamp methods and protocols*, pages 221–242. Springer, 2014. 36

[148] Katharina T Hofer, Ágnes Kandrács, István Ulbert, Ildikó Pál, Csilla Szabó, László Héja, and Lucia Wittner. **The hippocampal CA3 region can generate two distinct types of sharp wave-ripple complexes, in vitro**. *Hippocampus*, **25**(2):169–186, 2015. 36, 41

[149] Marius Pachitariu, Nicholas A Steinmetz, Shabnam N Kadir, Matteo Carandini, and Kenneth D Harris. **Fast and accurate spike sorting of high-channel count probes with KiloSort**. In *Advances in Neural Information Processing Systems*, pages 4448–4456, 2016. 40

[150] Marius Pachitariu, Nicholas Steinmetz, Shabnam Kadir, Matteo Carandini, and Kenneth D Harris. **Kilosort: realtime spike-sorting for extracellular electrophysiology with hundreds of channels**. *BioRxiv*, page 061481, 2016. 40

[151] Richárd Fiáth, Adrienn Lilla Márton, Ferenc Mátyás, Domonkos Pinke, Gergely Márton, Kinga Tóth, and István Ulbert. **Slow insertion of silicon probes improves the quality of acute neuronal recordings**. *Scientific reports*, **9**(1):111, 2019. 40

[152] Joe H Ward Jr. **Hierarchical grouping to optimize an objective function**. *Journal of the American statistical association*, **58**(301):236–244, 1963. 41

DOI:10.15774/PPKE.ITK.2020.005

[153] Balázs Chiovini, Gergely F Turi, Gergely Katona, Attila Kaszás, Ferenc Erdélyi, Gábor Szabó, Hannah Monyer, Attila Csákányi, E Sylvester Vizi, and Balázs Rózsa. **Enhanced dendritic action potential backpropagation in parvalbumin-positive basket cells during sharp wave activity**. *Neurochemical research*, **35**(12):2086–2095, 2010. 42

[154] Balázs Chiovini, Gergely F Turi, Gergely Katona, Attila Kaszás, Dénes Pálfi, Pál Maák, Gergely Szalay, Mátyás Forián Szabó, Gábor Szabó, Zoltán Szadai, et al. **Dendritic spikes induce ripples in parvalbumin interneurons during hippocampal sharp waves**. *Neuron*, **82**(4):908–924, 2014. 42

[155] Yi Lu, Tanyuan Wang, Zhengxu Cai, Yuliang Cao, Hanxi Yang, and Yanwen Y Duan. **Anodically electrodeposited iridium oxide films microelectrodes for neural microstimulation and recording**. *Sensors and actuators B: Chemical*, **137**(1):334–339, 2009. 45

[156] S Herwik, O Paul, and P Ruther. **Ultrathin silicon chips of arbitrary shape by etching before grinding**. *Journal of microelectromechanical systems*, **20**(4):791–793, 2011. 45

[157] Franz Lärmer and Andrea Urban. **Challenges, developments and applications of silicon deep reactive ion etching**. *Microelectronic engineering*, **67**:349–355, 2003. 45

[158] Luis A Camuñas-Mesa and Rodrigo Quian Quiroga. **A detailed and fast model of extracellular recordings**. *Neural computation*, **25**(5):1191–1212, 2013. 48, 49, 101

[159] R Quian Quiroga, Zoltan Nadasdy, and Yoram Ben-Shaul. **Unsupervised spike detection and sorting with wavelets and superparamagnetic clustering**. *Neural computation*, **16**(8):1661–1687, 2004. 63

[160] Takashi DY Kozai and Alberto L Vazquez. **Photoelectric artefact from optogenetics and imaging on microelectrodes and bioelectronics: new challenges and opportunities**. *Journal of materials chemistry B*, **3**(25):4965–4978, 2015. 77, 90

[161] Tongsheng Zhang and Yoshio Okada. **Recursive artifact windowed–single tone extraction method (RAW–STEM) as periodic noise filter for electrophysiological signals with interfering transients**. *Journal of neuroscience methods*, **155**(2):308–318, 2006. 78

[162] Vincent Wu, Israel M Barbash, Kanishka Ratnayaka, Christina E Saikus, Merdim Sonmez, Ozgur Kocaturk, Robert J Lederman, and Anthony Z Faranesh. **Adaptive noise cancellation to suppress electrocardiography artifacts during real-time interventional MRI**. *Journal of magnetic resonance imaging*, **33**(5):1184–1193, 2011. 78

[163] Anna Chabuda, Piotr Durka, and Jarosław Żygierewicz. **High frequency SSVEP-BCI with hardware stimuli control and phase-synchronized comb filter**. *IEEE Transactions on neural systems and rehabilitation engineering*, **26**(2):344–352, 2017. 78

[164] Duygu Kuzum, Hajime Takano, Euijae Shim, Jason C Reed, Halvor Juul, Andrew G Richardson, Julius De Vries, Hank Bink, Marc A Dichter, Timothy H Lucas, et al. **Transparent and flexible low noise graphene electrodes for simultaneous electrophysiology and neuroimaging**. *Nature communications*, **5**:5259, 2014. 78

[165] Dong-Wook Park, Sarah K Brodnick, Jared P Ness, Farid Atry, Lisa Krugner-Higby, Amelia Sandberg, Solomon Mikael, Thomas J Richner, Joseph Novello, Hyungsoo Kim, et al. **Fabrication and utility of a transparent graphene neural electrode array for electrophysiology, in vivo imaging, and optogenetics**. *Nature protocols*, **11**(11):2201, 2016. 78

DOI:10.15774/PPKE.ITK.2020.005

[166] A Zátonyi, Zs Borhegyi, M Srivastava, D Cserpán, Z Somogyvári, Z Kisvárday, and Z Fekete. **Functional brain mapping using optical imaging of intrinsic signals and simultaneous high-resolution cortical electrophysiology with a flexible, transparent microelectrode array**. *Sensors and actuators B: Chemical*, **273**:519–526, 2018. 78, 86

[167] Yi Qiang, Pietro Artoni, Kyung Jin Seo, Stanislav Culaclii, Victoria Hogan, Xuanyi Zhao, Yiding Zhong, Xun Han, Po-Min Wang, Yi-Kai Lo, et al. **Transparent arrays of bilayer-nanomesh microelectrodes for simultaneous electrophysiology and two-photon imaging in the brain**. *Science advances*, **4**(9):eaat0626, 2018. 78

[168] A Zátonyi, M Madarász, Á Szabó, T Lőrincz, R Hodován, B Rózsa, and Z Fekete. **Transparent, low-autofluorescence microECoG device for simultaneous Ca2+ imaging and cortical electrophysiology in vivo**. *Journal of neural engineering*, **17**(1):016062, 2020. 78

[169] Joana Pereira Neto, Adriana Costa, Joana Vaz Pinto, André Marques-Smith, Júlio Costa, Rodrigo Martins, Elvira Fortunato, Adam Raymond Kampff, and Pedro Barquinha. **Transparent and flexible ECoG electrode arrays based on silver nanowire networks for neural recordings**. *BioRxiv*, 2020. 78

[170] Gábor Orbán, Domokos Meszéna, Kinga Réka Tasnády, Balázs Rózsa, István Ulbert, and Gergely Márton. **Method for spike detection from microelectrode array recordings contaminated by artifacts of simultaneous two-photon imaging**. *PLoS one*, **14**(8), 2019. 79, 94, 97

[171] Zoltán Fekete, Emese Pálfi, Gergely Márton, M Handbauer, Zs Bérces, I Ulbert, A Pongrácz, and L Négyessy. **Combined in vivo recording of neural signals and iontophoretic injection of pathway tracers using a hollow silicon microelectrode**. *Sensors and actuators B: Chemical*, **236**:815–824, 2016. 86

[172] Helena Glabska, Jan Potworowski, Szymon Leski, and Daniel K Wójcik. **Independent components of neural activity carry information on individual populations**. *PLoS one*, **9**(8):e105071, 2014. 88

[173] Helena T Glabska, Eivind Norheim, Anna Devor, Anders M Dale, Gaute T Einevoll, and Daniel K Wójcik. **Generalized laminar population analysis (gLPA) for interpretation of multielectrode data from cortex**. *Frontiers in neuroinformatics*, **10**:1, 2016. 88

[174] Kaylene C Stocking, Alberto L Vazquez, and Takashi DY Kozai. **Intracortical neural stimulation with untethered, ultrasmall carbon fiber electrodes mediated by the photoelectric effect**. *IEEE Transactions on biomedical engineering*, **66**(8):2402–2412, 2019. 90